

**Numerical investigation of the use of externally generated Lorentz forces to
improve the flow pattern in a continuous glass-melting tank**

Dissertation

zur Erlangung des akademischen Grades

Doktoringenieur (Dr.-Ing.)

vorgelegt der

Fakultät für Elektrotechnik und Informationstechnik der
Technischen Universität Ilmenau

von Herrn

M.Sc. Senan Soubeih

geboren am 01.06.1981 in Latakia, Syrien

Gutachter:

Priv.-Doz. Dr.-Ing. habil. Ulrich Lüdtké
apl. Prof. Dr.-Ing. habil. Christian Karcher
Univ.-Prof. Dr.-Ing. Egbert Baake

Tag der wissenschaftlichen Aussprache: 20.10.2016

urn:nbn:de:gbv:ilm1-2016000518

Zusammenfassung

Das elektromagnetische Boosting (*EMB*) ist ein neuer und innovativer Lösungsansatz zur Verbesserung der Strömungsverhältnisse in den kontinuierlich arbeitenden Glasschmelzwannen mit einer elektrischen Zusatzbeheizung. Das *EMB* basiert auf der Benutzung von extern induzierten Lorentzkräften, die entgegen der Hauptströmungsrichtung in der Schmelzwanne gerichtet sind. Die Generierung dieser zusätzlichen Lorentzkräfte erfolgt durch die Überlagerung eines externen Magnetfeldes mit der in der Glasschmelze fließenden elektrischen Ströme. Das externe Magnetfeld wird von zusätzlichen Magnetspulen generiert. Diese werden unterhalb des Wannenbodens zwischen den Elektroden der Zusatzbeheizung installiert. Dadurch wird ein steuerbarer elektromagnetischer Wall in der Glasschmelze zwischen den Elektroden realisiert. Dieser verhindert die unerwünschte Strömung der kälteren, bodennahen Glasschmelze zum Wannenauslass. Als Ergebnis wird die minimale Verweilzeit (*MRT*) der Glasschmelze in der Wanne erhöht und somit die Verweilzeitverteilung (*RTD*) verbessert. Als Ergebnis wird die Glasqualität erhöht.

In dieser Dissertation wird das *EMB* in einer Glasschmelzwanne numerisch untersucht und somit die Grundlage für eine industrielle Anwendung gelegt. Die stark temperaturabhängigen Materialeigenschaften von Glas erfordern gekoppelte Berechnungen von Elektro-, Thermo- und Hydrodynamik, die zu hochkomplexen, dreidimensionalen, numerischen Simulationen der Problemstellung führen. Die Simulationen werden für eine reale industrielle Glasschmelzwanne unter Annahme einiger Vereinfachungen durchgeführt. Die Randbedingungen sind so definiert, dass die realen Betriebsverhältnisse der Wanne simuliert werden können. Für das *EMB* wird ein zusätzliches Spulensystem angepasst.

Die Simulationen zeigen, dass es im Prinzip möglich ist, einen steuerbaren elektromagnetischen Wall im Boostingbereich zu erzeugen. Um die optimale Wirkung des *EMB* zu erzielen, sind Parameterstudien durchgeführt worden. Mit diesen Simulationen wird erstmals das dynamische Betriebsverhalten einer Glasschmelzwanne mit *EMB* untersucht. Die Ergebnisse zeigen, dass die gewünschte wesentliche Erhöhung von *MRT* und die damit verbundene Verbesserung von *RTD* mit Hilfe des *EMB* erzielbar sind, wodurch die Qualität des Endproduktes erhöht wird. Des Weiteren kann mit Hilfe des *EMB* die Glasqualität verbessert und gleichzeitig der Durchsatz der Wanne erhöht werden. Unter normalen Betriebsverhältnissen ohne das *EMB* ist dies nicht möglich. Diese theoretischen Untersuchungen bilden den ersten Schritt, das *EMB* in der Praxis zu testen und einzusetzen, um neuartige Glasschmelzwannen mit höherem Wirkungsgrad und verbesserter Qualität des Glasproduktes in der Industrie einzuführen.

Abstract

Electromagnetic boosting (*EMB*) is a new and innovative approach for improving the flow patterns within electrically boosted continuous glass-melting tanks. *EMB* is basically achieved by electromagnetic (Lorentz) forces that are orientated against the main flow direction of the glass melt in the tank. The additional Lorentz forces are produced within the glass melt by an externally generated magnetic field interacting with the electric currents that exist within the glass melt. For the process, additional magnet coils are placed underneath the tank bottom and positioned between heating electrodes. Thus, a controllable electromagnetic wall is created in the boosting area to impede the flow of the colder, less well-melted bottom glass through the gaps between the electrodes towards the tank-outlet. The desired *EMB* effect is an increase in the minimum residence time (*MRT*) of the glass melt within the tank and consequent improving of the residence time distribution (*RTD*), with enhanced glass quality as the ultimate result.

Using numerical tools, the author of this thesis has realized and evaluated the *EMB* in a continuous glass-melting tank, laying the foundation necessary for the idea to be converted into an effective industrial process. As the physical properties of glass are strongly temperature-dependent, the numerical simulation involves calculation of the coupled electrodynamic, thermodynamic, and hydrodynamic effects. The investigation thus largely consists in a highly complex coupled three-dimensional mathematical problem. The simulations are performed for a particular industrial-scale continuous glass-melting tank which is represented in academic form. The boundary conditions are so defined as to simulate the realistic conditions of the particular tank. An external magnet coils system which would produce *EMB* in the particular tank is incorporated into the calculations.

The simulations show that it is basically possible to create an electromagnetic wall within the glass melt between the heating electrodes. Parameter analyses for optimization of the *EMB* effect are also presented. The simulation results make it possible, for the first time, to analyze the dynamic behavior of an electromagnetically boosted continuous glass-melting tank in operation. They also reveal that *EMB* affects the glass melt flow within the tank favorably, increasing the *MRT* substantially and thus enhancing the glass quality. Moreover, the tank simulations with *EMB* show that it is possible to increase the tank productivity and enhance the glass quality simultaneously, which is not possible in the ordinary tank operation case without *EMB*. Through the author's work, the first step, always the most important, has been taken en route to a sophisticated glass-melting tank characterized by high efficiency and high production quality.

Contents

1	Introduction.....	1
1.1	Glass processing	1
1.2	Numerical simulation in glass technology.....	2
1.3	About this work	3
2	Continuous glass-manufacturing process	4
2.1	Continuous glass-melting systems.....	4
2.2	Flow patterns within continuous glass-melting tanks.....	6
2.3	Residence time distribution (<i>RTD</i>)	7
3	Electric boosting (<i>EB</i>).....	9
3.1	Flow control in continuous glass-melting tanks	9
3.2	Continuous glass-melting tanks with barrier booster	10
4	Scope of thesis.....	13
4.1	Concept of electromagnetic boosting (<i>EMB</i>)	13
4.2	Aim and objectives of the thesis.....	15
4.3	Overview of the thesis	17
5	Literature, state of the art	19
5.1	Numerical simulation of glass-melting tanks	19
5.2	Lorentz forces in glass manufacture	21
5.2.1	Natural Lorentz forces.....	21
5.2.2	Artificial Lorentz forces	23
6	Problem formulation	27
6.1	Tank representation	27
6.2	Mathematical model	30
6.2.1	Glass material properties	30
6.2.2	Electromagnetic field	31
6.2.3	Flow and temperature fields.....	33
7	Numerical methodology.....	35
7.1	Coupling the calculations	35

7.2	Calculating electromagnetic field with FLUENT	36
7.3	Validation by numerical simulation with MAXWELL	38
7.3.1	Boundary conditions of the cube-model	39
7.3.2	Results of comparison	40
7.4	A simplified tank model with two electrodes	49
7.4.1	The model employed	50
7.4.2	Boundary conditions of the middle-section model	51
7.4.3	Computational grid and numerical solution	52
7.4.4	Results from the middle-section model.....	52
7.5	Calculating a steady-state AC system with FLUENT	58
8	Numerical grid, solution, and accuracy	61
8.1	Computational grid	61
8.2	Numerical solution	63
8.3	Verification and accuracy	64
8.3.1	Mesh-convergence study	65
8.3.2	Residual evaluation study.....	67
9	Implementation and results	69
9.1	The baseline-case.....	69
9.1.1	Boundary conditions	69
9.1.2	Selected results of the baseline-case simulation	72
9.2	Adapting the <i>EMB</i> system	76
9.3	Optimizing the <i>EMB</i> system.....	78
9.3.1	The optimum <i>MRT</i>	78
9.3.2	Coil diameter study	79
9.4	Comparison between the baseline-case and <i>EMB</i> -case	81
9.5	Increasing the tank productivity	87
9.6	Increasing the tank thermal efficiency.....	90
9.7	Considering the structural steel girders	93
9.7.1	Boundary conditions	94

9.7.2	Results and discussion.....	95
10	Conclusion and outlook	99
10.1	Conclusion	99
10.2	Outlook	100
	Bibliography	101
	List of abbreviations.....	110
	List of symbols	111

1 Introduction

Glass is a unique material that has been manufactured and used without interruption for more than 5000 years. Glass-making is a very ancient form of industry that is still evolving and constantly improving as the uses for glass expand. A full insight into the evolution of glass making technology including its cultural implications over the millennia is presented in [1–4].

1.1 Glass processing

Today, life is unthinkable without glass, the manifold uses of which extend into almost every field of modern science, industry, and our personal lives. Examples are containers, architecture, touch screens, electronics, communication equipment, medical equipment, laboratory equipment, optics, automotive, aircraft, or spaceship. Glass has been vital to technological advancement, being continually proposed for new applications. Detailed descriptions of glass types and their applications are given in [4–7].

The most important commercial glasses today are container glass (mainly for holding foods and drinks) and flat glass (mainly for architecture and automotive applications). These glasses belong to a glass type called “soda-lime glass”, and are basically composed of soda (Na_2O) and lime (CaO) beside the main component, namely silica sand (SiO_2).

The raw materials that are used for commercial glass manufacture are some of the most abundant in the Earth’s crust, see [8,9] for comprehensive information. After suitable treatment, these raw materials are weighed and mixed together to the desired composition forming what is called “batch”. The process in which the raw materials are stored, weighed, mixed, and delivered to the melting furnaces is called “batching”. In modern manufacture, it has been fully automated and improved by computer systems, e.g. [10,11]. Crushed glass called “cullet”, which helps to accelerate the melting of the sand and to reduce the energy required for melting, is also added to the batch. Nowadays, recycling of waste glass is becoming increasingly important to reduce the consumption of energy as well as raw materials.

After the batching stage, a glass-melting furnace receives the batch and heats it strongly to start the melting, which is the major stage in the glass manufacturing process. Since commercial glasses are needed in huge amounts, the batch is fed non-stop into the furnace and glass is melted in a continuous manner. At the end of the melting stage, the glass melt, which has been obtained, is delivered to forming devices, or molds, for the forming stage, in which glass melt will cool to the desired shape.

Glass-melting furnaces are mostly tank-furnaces heated by fossil fuels (natural gas or fuel oils) and electric power, sometimes independently and sometimes in combination. These tank-furnaces are operated continuously for high-tonnage production with a steady flow of glass melt into the automatic forming devices. The successive processes of glass manufacturing including the various types of construction and device are thoroughly covered in [12–14].

The flow of molten glass within the glass-melting tank is mainly driven by natural convection of mass. The flow pattern itself plays an important role in the achievement of a qualitatively acceptable glass product. Hence, controlling the flow patterns within the glass-melting tanks so as to improve tank performance is one of the glass industry's primary challenges. However, controlling the glass melt flow in these tanks is fraught with difficulties.

1.2 Numerical simulation in glass technology

When industrial processes are being analysed, numerical simulation is an effective tool. It can predict the dynamic regime behavior after changes in process conditions. Moreover, if systems are to be developed that involve risky working conditions and high constructional costs, as the case with continuous glass-melting tanks, numerical simulation offers wide possibilities at low cost and with rapid response time and no risk involved. Thus, numerical models have come to be of vital importance in the development of industrial systems.

In the glass industry, numerical simulation is now a reliable and effective tool for developing new products, reducing production costs, and improving glass quality. It also offers the possibility in glass manufacture of obtaining data that are difficult to measure in the real process and of finding new parameter configurations without disturbing the operation.

Sine qua non to the simulation of industrial operations which involve highly complicated chemical and physical processes, such as glass melting process, is a deep understanding of the underlying physics and chemistry. As yet, there is no simulation tool that covers all processes in glass technology. Computational fluid dynamics (CFD) is often the basis of the mathematical models. The CFD models are linked with additional sub-models that have been developed to simulate different problems in the glass melting process. Several special purpose software packages are thus used and linked together.

The glass industry is always in search of ways of optimizing the glass manufacturing process especially improving glass quality and reducing energy consumption. Numerical models of glass technology are essential not only for optimizing current furnace design and operating parameters, but also for studying new furnace designs and evaluating new techniques. Thus, numerical models provide a solid foundation for important development decisions.

1.3 About this work

This thesis extends the possibilities for the development of industrial glass-melting tanks. The author shows his numerical investigation of the potential of an unconventional method for controlling the flow pattern within a continuous glass-melting tank. The method relies on electromagnetic flow control, where additionally generated electromagnetic (Lorentz) forces are brought to bear on the glass melt. To do so, an additional magnet system must be adapted and installed. This new and innovative approach is called “electromagnetic boosting”. The approach of employing additionally generated Lorentz forces to improve the flow patterns in continuous glass-melting tanks is, as yet, by no means an established technique. This thesis with its numerical investigation represents the sole groundwork to date for an industrial continuous glass-melting tank with new sophistication.

Using numerical simulation to develop engineering technologies and evaluate new approaches requires technical understanding and scientific analysis of the physical system studied. Additionally, it presupposes a degree of engineering inspiration to enable the physical and functional behaviors to be integrated. In the present research, the numerical simulations of the system considered were carried out with the commercially available software package ANSYS, which is general purpose simulation software.

2 Continuous glass-manufacturing process

This chapter describes industrial continuous glass furnaces, their process conditions, and some of their most important operating parameters.

2.1 Continuous glass-melting systems

Most types of the world's commercial glass are produced using tank-furnaces which operate in a continuous manufacturing process, and are able to produce large amounts of glass melt for automated production of the final item. In such furnaces, batch is constantly fed into the surface of the glass melt bath at one end of the furnace, and fully molten glass is continuously withdrawn from the other end. The glass mass flow rate is typically in the range of several kilograms per second, with an output of several hundred tons per day.

Figure 2.1 shows a simplified example of a continuous manufacturing system for container glass production. Continuous glass-melting systems are large structures with considerable weight, and they exist in different sizes and designs, of which there are examples in [14,15].

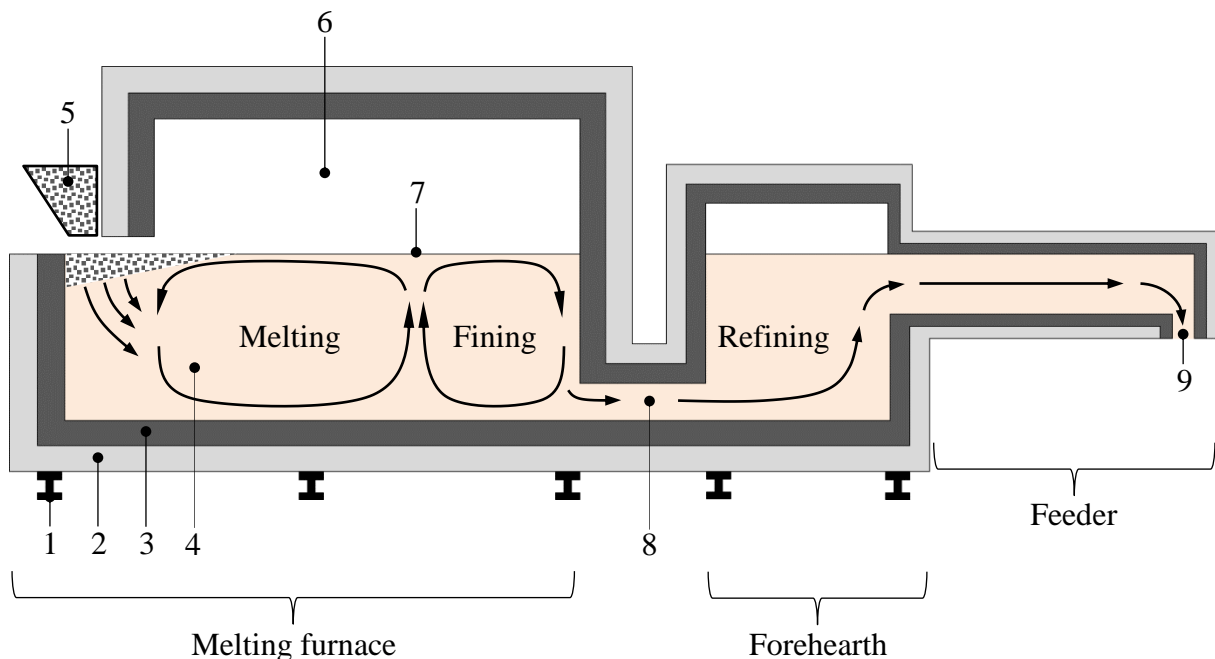


Figure 2.1: Simplified drawing of a continuous manufacturing system for producing container glass. 1 steel girder, 2 thermal insulation, 3 refractory wall, 4 glass bath, 5 batch charging, 6 combustion chamber, 7 hot spot, 8 throat, 9 discharging outlet.

The system illustrated consists of a melting furnace, a forehearth, and feeders. For the construction, refractory bricks, mostly of the fused cast alumina-zirconia-silica (AZS) type, are used [16,17]. There is a layer of thermal insulation bricks on the exterior of the furnace to reduce the wall heat losses. The whole construction stands on supporting steel girders.

The melting furnace, which is where the melting stage takes place, is a large tank with an integrated combustion chamber above. The tank has a capacity of dozens of cubic meters and the melting surface is dozens of square meters in area. The batch is fed into one or more openings in the sides of the tank, forming a blanket on the glass melt. The heat fusing the disparate batch materials is steadily transferred from the combustion chamber to the surface of the glass bath by radiation and convection. It comes from fossil fuel burners which shoot horizontal flames above the glass bath surface.

In the melting tank, the first of the three basic processes that take place is thus the melting. The other two are fining and homogenizing. The melting process is accomplished in the “melting zone” which extends over about two-thirds of the tank length. In this zone the batch materials are completely fused and dissolved, so that the melting process which begins when the batch enters the melting tank is completed when the glass melt becomes batch-free. The freshly molten glass contains numerous gaseous bubbles. These are removed by the fining process in which the bubbles rise to the glass bath surface and escape into the combustion space. This process is accomplished in the “fining zone” which is the last third of the melting tank. The homogenizing process, accomplished in the whole tank, is the thorough mixing of the molten glass to achieve uniformly distributed temperature throughout the glass melt, which will thus be thermally and chemically homogenous. In the melting zone, the homogenizing also involves uniformly distributing the batch components within the melt.

The glass melt obtained leaves the melting tank at a temperature of about 1350 °C, passing to a “forehearth” through a connecting throat. In the forehearth, the glass melt is slowly cooled from the necessary melting temperature to a defined temperature. This process allows the remaining small gaseous bubbles to dissolve in the glass melt, and is called “refining”. The forehearth is connected to automatic molds by several feeders which are usually ducts. In the feeders, the glass melt cools slowly from the refining temperature to the suitable forming temperature. The final glass melt product is discharged from the feeder-outlet to the automatic molds at a certain mass flow rate. Temperature homogenizing is also necessary in the forehearth and feeders to avoid defects, which can be caused if there are strong temperature gradients within the glass melt.

2.2 Flow patterns within continuous glass-melting tanks

Glass melt is characterized by *temperature-dependent* physical properties which significantly modify the glass melt flow. Since heat is released above the glass bath surface, the temperature is highest at the top, and lowest at the bottom of the tank. The induced temperature gradients within the glass melt lead to natural convection of the mass, owing to the variation of density with temperature. Thus, there is a thermal convection flow driven by buoyancy within the glass melt. Furthermore, this convection helps to transfer heat within the glass melt by raising the colder bottom glass melt layers into the hotter surface layers. As illustrated in Figure 2.1, the thermal convection flow results in two recirculating zones within the glass melt, namely melting and fining zones. The recirculating flows are integrated into the throughput flow which the batch charging causes in the glass melt. It should be noted that the recirculating flows through the continuous glass-melting tank are non-uniform and can be only poorly controlled, so that less well-melted, colder bottom glass melt may flow directly to the throat. The melting and fining zones are roughly separated by an upward stream caused by a limited region of maximum temperature called the “hot spot” on the glass bath surface (see Figure 2.1). The hot spot in the continuous glass-melting tank is due firstly to the fact that the boundaries of any heated container tend to be cooler than the center, and secondly to the fact that cold raw materials are introduced at one boundary, so that the hottest region is not at the center, but displaced accordingly.

The recirculating flows in the melting zone are necessary to transfer heat from the surface to the bottom, thus distributing the melting energy. They also determine the melting performance because they affect the time taken for the batch to melt. The recirculating flows in the fining zone serve to raise the gaseous bubbles to the surface. Furthermore, the recirculating flows in both zones determine the degree of mixing within the tank, which affects the homogeneity of the glass melt. Inhomogeneity in the glass product arises because not all glass melt particles in the melting tank will have the same processing history.

Glass melts are highly viscous fluids with a slow flow, so that in continuous glass-melting tanks, the glass melt moves with a velocity in the range of millimeters per second. The nature of glass melt flows is laminar flow. They have a low Reynolds number ($Re \approx 1$). The Reynolds number represents the ratio of inertial forces to viscous forces:

$$Re = \frac{\bar{u}L\rho}{\eta}, \quad (2.1)$$

where \bar{u} is the mean flow velocity, L is the characteristic travelled length, ρ is the mass density, and η is the dynamic viscosity.

2.3 Residence time distribution (*RTD*)

Continuous glass-melting tanks are large thermo-chemical reactors with very complex flow patterns. For adequate processing, the glass melt requires a *minimum residence time (MRT)* within the melting tank. This processing includes completely dissolving the raw materials, thoroughly mixing the glass melt, and properly degassing it to yield a product that satisfies the quality standards. *MRT* is determined by the recirculating flows within the glass-melting tanks. A very low *MRT* implies that a part of the glass melt has not had enough time to be completely melted, thoroughly mixed, and properly degassed. Thus, *MRT* is an indicative parameter and a decisive criterion for evaluating glass quality.

Differences in residence time are imposed by the hardly controllable flow patterns within continuous glass-melting tanks. The glass melt particles travel along an unlimited number of different possible paths between the various positions at the charging opening and the destinations at the throat. The glass melt particles will also, clearly, have non-uniform recirculating history through the tank. As travelling along a certain path takes a certain length of time, the different glass melt particles will spend different lengths of time within the tank. So, each glass melt particle by following its path will have a particular residence time within the tank. These residence time differences and variations in the processing time of the glass melt particles cause inhomogeneity in the glass melt.

An ideal melting cycle (Figure 2.2 (a)) assumes, in a simplified manner, that all glass melt particles flow uniformly through the tank. Accordingly, if the melting cycle were ideal, all glass melt particles would have the same residence time within the tank. This uniform residence time would be equal to the mean residence time τ , which is given by the ratio of the tank space volume V (glass bath volume) to the volumetric flow rate through the tank \dot{V} :

$$\tau = \frac{V}{\dot{V}} . \quad (2.2)$$

The slightly recirculated glass melt particles will, clearly, have shorter residence times than the ideal. Thus, some parts of the glass product will be less-well processed and will be of lower quality than the average, while excessively recirculated glass parts will have longer residence times than the ideal and will be responsible for wasted consumption of energy.

The distribution of the lengths of time spent by every glass melt particle within the melting tank is called “residence time distribution” (*RTD*). Continuous glass-melting tanks show wide *RTD* (see Figure 2.2 (b)). In typical tanks, *MRT* is between 7% and 15% of the mean residence time τ . The result is inhomogeneity in the glass melt product. The element of the glass melt with the *MRT* has the worst quality.

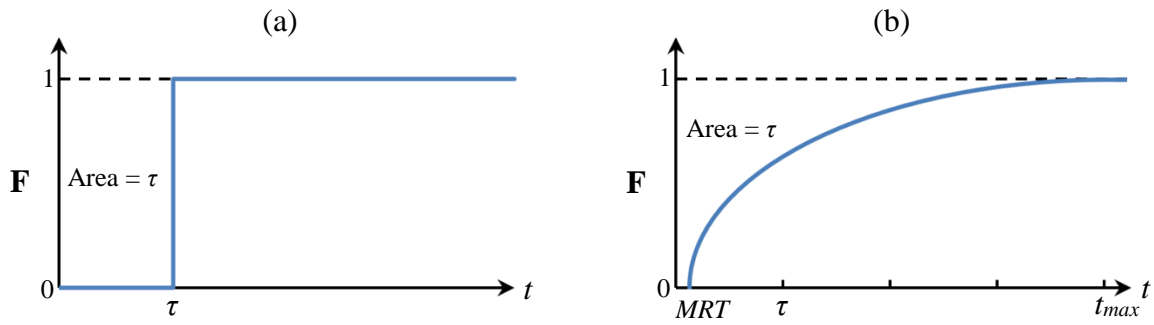


Figure 2.2: Transition function or **F** curve describing the cumulative residence time distribution in a reactor: (a) ideal **F** curve and (b) typical **F** curve for continuous glass-melting tanks.

In chemical reaction engineering, *RTD* is an important parameter for assessing the reactor operation. *RTD* is usually found by tracer studies, in which an amount of tracer is introduced at the tank-inlet, and the change in its concentration over time is measured at the tank-outlet. The *RTD* transition function (also called the “**F** curve”) describes the cumulative *RTD*. The **F** curve can be established by plotting the mass fraction rise from zero to unity at the tank-outlet as a function of time, see Figure 2.2 [18]. In other words, the **F** curve describes the glass melt particles leaving the tank as a function of time. Consider a quantity of glass that is introduced at the tank-inlet at $t = 0$. The observer is measuring at the tank-outlet. A fraction of the introduced glass will be observed arriving at the tank-outlet first after an *MRT*. Then, the fraction arriving the tank-outlet will continue to increase until the complete glass amount, which represents unity, has left the tank after a maximum residence time t_{max} .

The mean residence time τ , which is constant at a constant volumetric flow rate through the tank (see Equation (2.2)), is represented by the area above the **F** curve:

$$\tau = t_{max} - \int_{MRT}^{t_{max}} \mathbf{F} dt, \quad (2.3)$$

with $MRT \leq \tau$ and $t_{max} \geq \tau$.

As these mathematical observations reveal, it would be possible significantly to enhance both glass melt quality and homogeneity by *increasing* the *MRT* in continuous glass-melting tanks. Furthermore, an increase in *MRT* will be accompanied by a decrease in t_{max} (see Equation (2.3)), resulting in a *narrower RTD*, which means more homogeneous processing of all parts of the glass melt. An ideal *RTD* would be attained if $MRT = t_{max} = \tau$, cf. Figure 2.2 (a) and (b).

Controlling the flow patterns within the glass-melting tanks is a key technique for *increasing MRT* and consequently *improving RTD*, which is one of the glass industry’s primary challenges and also the main motivation for this thesis.

3 Electric boosting (EB)

This chapter turns to the electrically boosted continuous glass-melting tanks which are specific to the investigation reported in this thesis.

3.1 Flow control in continuous glass-melting tanks

Chapter 2 has already described the complex flow pattern within continuous glass-melting tanks, and how significantly it affects the melting process. It has also explained how controlling the glass melt flow within the tank can improve both melting performance and glass quality. However, glass melt flow in continuous glass-melting tanks is extremely difficult to influence and can be only poorly controlled. In the glass industry, it is common to apply one or more of two well-established methods to control the glass melt flow within the continuous glass-melting tanks. These are bubbling and electric boosting. A description follows.

To achieve a certain amount of flow control, the natural convection in continuous glass-melting tanks is locally enhanced by an additional flow induced near the hot spot location. The additional flow improves the mixing by raising the colder, less-well melted glass from the bottom towards the surface. It also intensifies the upward stream which separates the melting and fining processes. The effect is produced either by “bubbling”, which is blowing air or other gases through special nozzles installed in the tank bottom near the hot spot location, or by “electric boosting” which applies direct electric heating to introduce additional heat into the glass bath, especially near the hot spot location. The electrically generated heat induces an additional thermal convection current within the glass melt, which will bear the bottom glass melt upwards, see Figure 3.1. The direct electric heating generates Joule heat within the glass melt by using electrodes. As glass melt is itself a good electrolyte, the electrodes conduct electric currents directly through it. There is detailed information on the electrochemistry of glass melts in [19–21]. Although glass in its solid state is a good electrical insulator, it is electrically conducting when molten, for there is a temperature-dependent increase in electrical conductivity. In general, glass melts have an electrical conductivity about five times higher than that of sea water. Bubbling in comparison with electric boosting has the disadvantage of cooling the glass melt, while the latter introduces additional heat and intensifies the hot spot. However, both methods have the disadvantage of exercising only localized influence on the glass melt flow.

As the thesis addresses the use of additional Lorentz forces, the existence of electric current density within the glass melt is crucial.

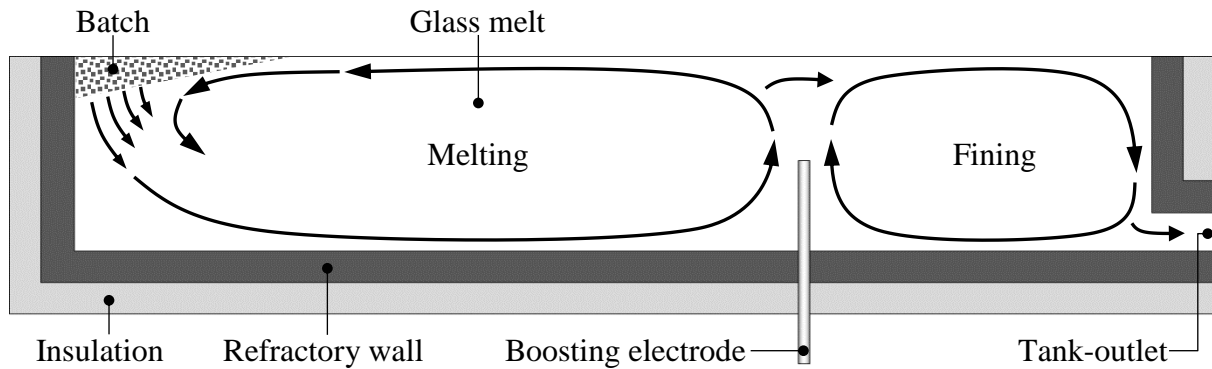


Figure 3.1: Simplified sketch of a conventional continuous glass-melting tank with bottom boosting electrodes, with illustration of the characteristic flow pattern in a longitudinal cross section.

3.2 Continuous glass-melting tanks with barrier booster

For the purposes of the investigation, an industrial continuous glass-melting tank equipped with an electric boosting system called the “barrier booster” is considered. The barrier booster consists of a rod electrode configuration installed near the hot spot location. The glass bath is thus heated in the location of the electrodes, so that a thermal barrier is created [22,23], which supports the hot spot effect and fixes its location. The barrier booster is typically composed of six rod electrodes introduced into the glass bath vertically through the tank bottom. The boosting electrodes are spaced evenly in a row across the width of the tank. They are made of molybdenum which is the material most compatible with almost all glass types [24,25]. Figures 3.1 and 3.2 provide a schematic representation of the continuous glass-melting tanks that are equipped with a barrier booster system. It is common to install a barrier wall of refractory material behind the barrier booster. This type of continuous glass melting-tank is used for the production of container glass. It has a capacity of about 50 m³ and a glass mass flow rate of about 100 T/D (tons per day).

Thus, in continuous glass-melting tanks with barrier booster, electric currents pass through the glass melt between the electrodes generating Joule heat, which induces additional buoyancy-driven flows within the glass melt. This forces the colder, less well-melted glass upwards from the bottom so that it benefits from the heat above. By forcing the bottom glass melt to be recirculated within the melting zone in this way, the barrier booster also *increases* the *MRT*. The positive effect on the glass quality has already been explained in Section 2.3.

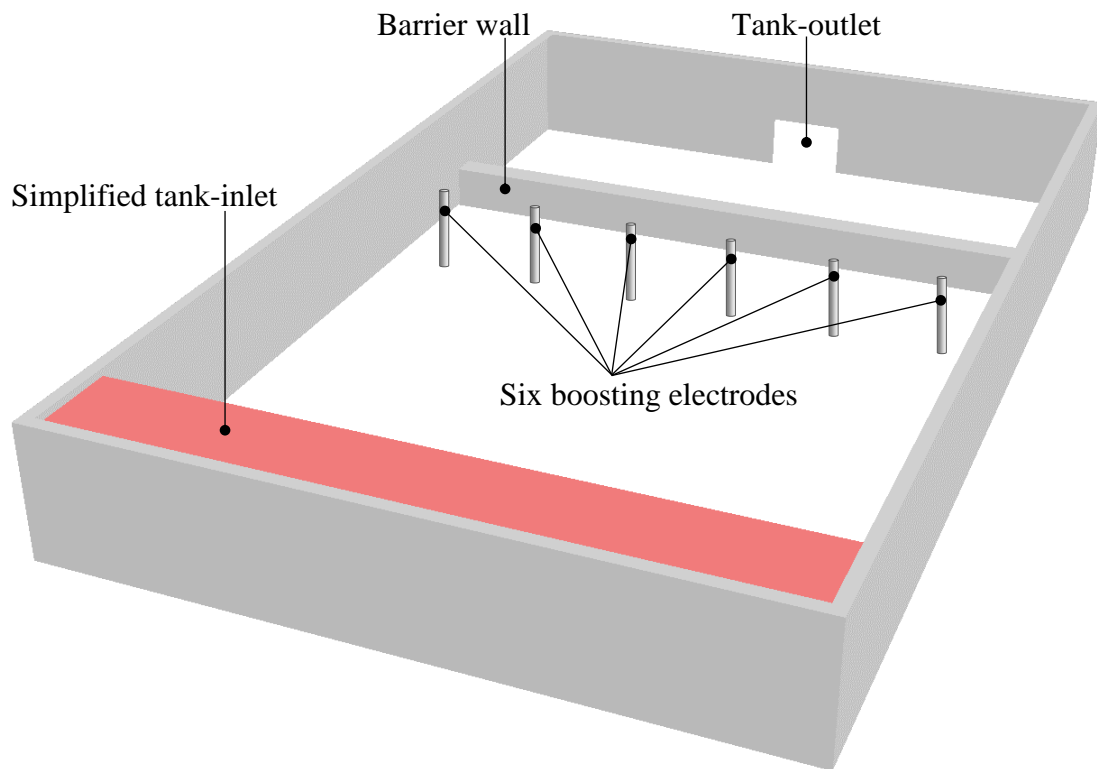


Figure 3.2: Simplified view of a conventional continuous glass-melting tank with a barrier booster system composed of six bottom electrodes and supported by a barrier wall built behind the electrodes.

However, there are gaps between the electrodes, where the electric boosting is less effective and the bottom glass melt flows directly into the throat, impairing the glass quality. For this reason, the barrier booster effect is supported by a barrier wall of refractory material installed behind the electrodes. This barrier wall is anchored in the tank bottom and projects upwards with roughly the same height as the electrodes. It has the disadvantage of being eroded over time, causing additional impurities in the glass melt, as well as reducing the lifetime of the tank. The decision to use a barrier wall to support the electric boosting effect is usually based on different factors, especially the intended glass quality and the electric power value designated for boosting. Therefore, the barrier wall is not always necessary, and in many cases is not installed.

To operate the barrier booster, a distributed three-phase alternating current (AC) system is applied to energize the electrodes, typically at 50 Hz, using a different electrical phase for each electrode in a sequential distribution with phase shifting of 60° as shown in Figure 3.3. Electric currents flow between each electrode and the other five electrodes. Thus, a homogeneous dissipation of electric heating within the glass melt is achieved, where the electric power used is

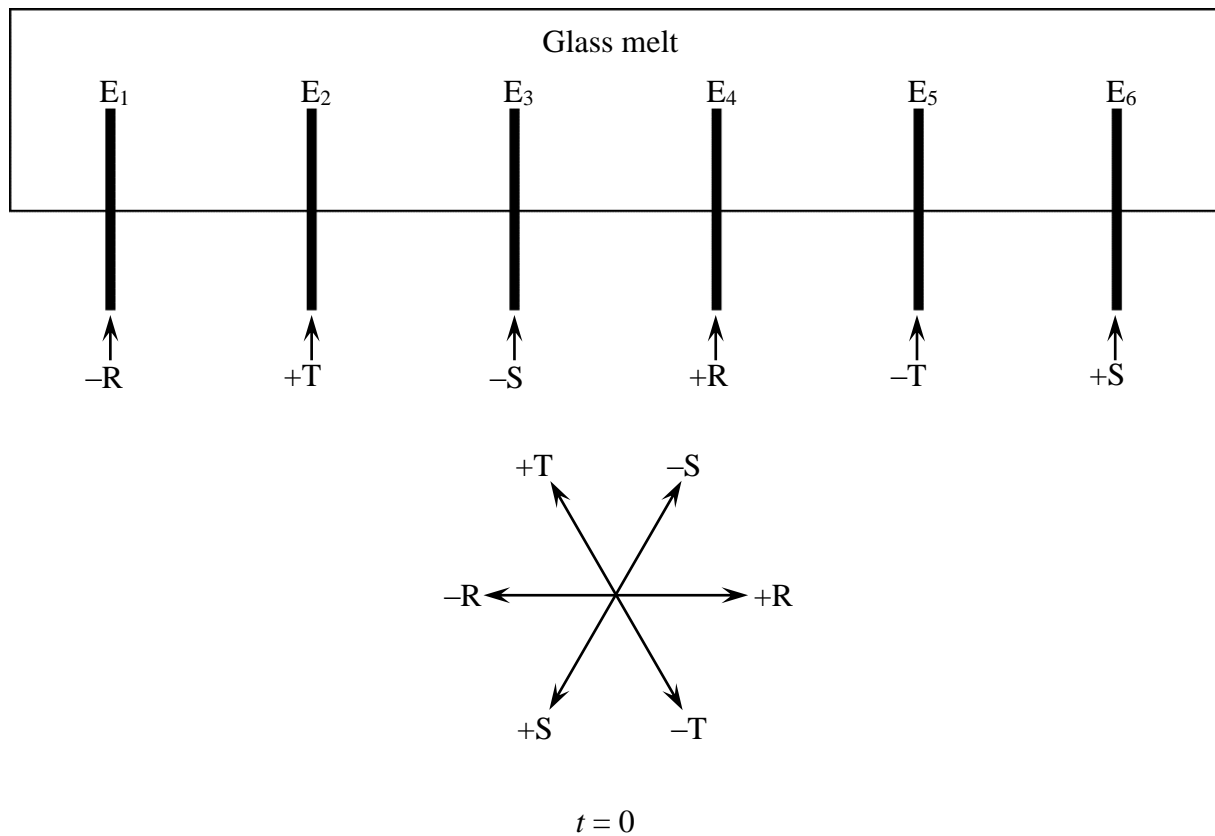


Figure 3.3: Circuit arrangement for operating the barrier booster system considered, showing the electrical phase distribution with a phase shifting of 60° applied to the boosting electrodes ($E_{1,\dots,6}$) to achieve a homogeneous dissipation of electric heating power within the glass melt.

typically about 700 kW. Power transformers are used to connect the electrodes to the supply line [26].

The energizing scheme of the barrier booster system results in complex electric current patterns within the glass melt. These complexities complicate the adaption of an additional magnet coils system for electromagnetic boosting.

4 Scope of thesis

This chapter states the main substance of this thesis, the concept of electromagnetic boosting in electrically boosted continuous glass-melting tanks. It also includes a presentation of the aim and objectives, then concludes with an overview.

4.1 Concept of electromagnetic boosting (*EMB*)

Electromagnetic boosting (*EMB*) is a new and innovative approach to improving the flow patterns within the electrically boosted continuous glass-melting tanks. The idea of *EMB* is to create a controllable electromagnetic barrier between the boosting electrodes which will hinder the flow of the bottom glass melt. Furthermore, the electromagnetic barrier, being material-free, causes no additional impurities in the glass melt, and can replace the traditional barrier wall. *EMB* can be realized by installing supplementary magnet coils below the bottom of the tank in positions between the boosting electrodes. The external coils introduce a magnetic flux density \mathbf{B}_c into the glass bath, superimposing this on the existing electric current density \mathbf{J} which is flowing through the glass melt from one electrode to the other. Thus an artificial Lorentz force density \mathbf{f}_{La} is generated within the glass melt according to

$$\mathbf{f}_{La} = \mathbf{J} \times \mathbf{B}_c . \quad (4.1)$$

Figure 4.1 schematically illustrates the basic principle of *EMB*. The additionally generated Lorentz forces, in *EMB*, are orientated opposite to the main flow direction within the tank as illustrated in Figure 4.1. They will thus oppose the glass melt flow between the electrodes, hindering the flow of the bottom glass melt towards the throat. The colder, less well-melted bottom glass

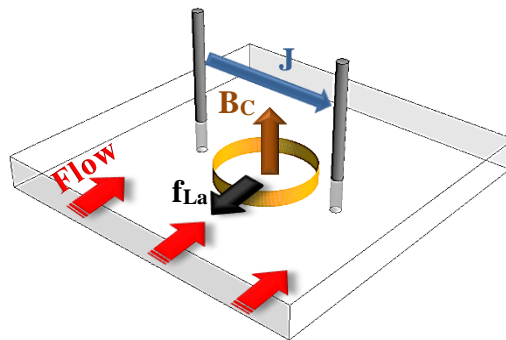


Figure 4.1: Basic principle of electromagnetic boosting (*EMB*) in electrically boosted glass-melting tanks; \mathbf{J} : electric current density within the glass melt, \mathbf{B}_c : magnetic flux density generated by the coil, and \mathbf{f}_{La} : artificial Lorentz force density.

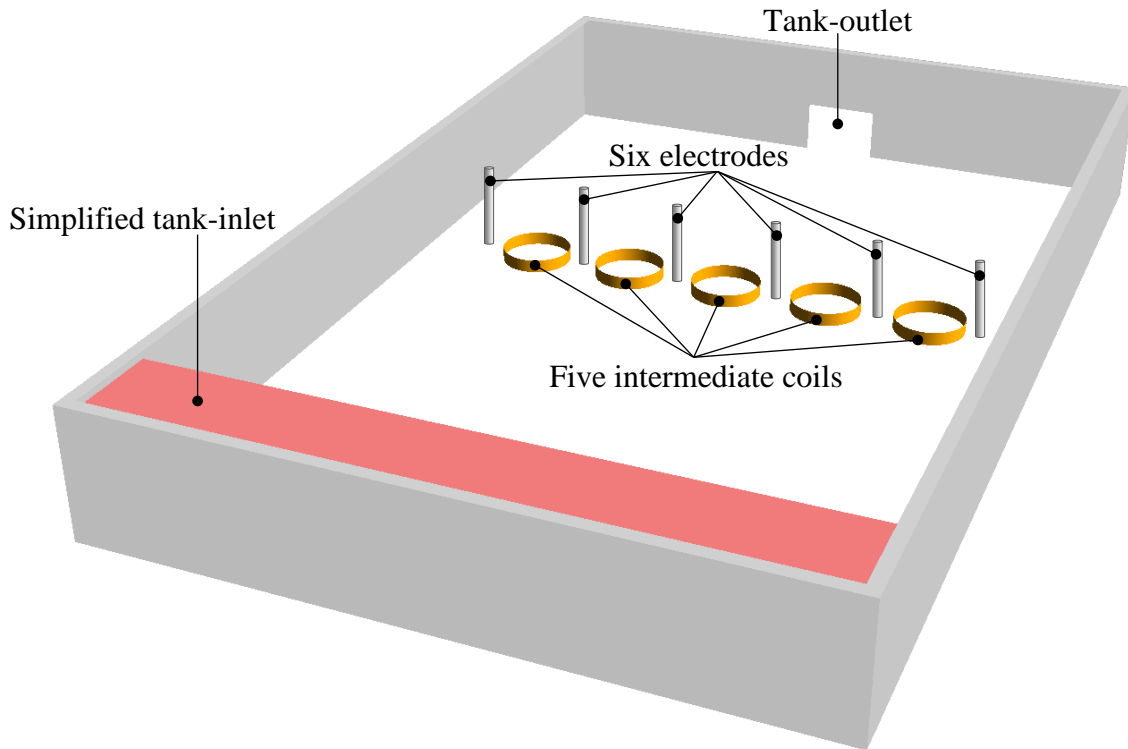


Figure 4.2: Simplified view of a continuous glass-melting tank with an electromagnetic boosting system composed of the existing six boosting electrodes and five additional intermediate coils placed below the bottom of the tank.

will thus be recirculated in the melting zone so that it is better heated and melted. The effect is an *increase* in the *MRT* in the melting tank. Moreover, the method supports the fluidic separation of the melting and fining zones. Figure 4.2 illustrates a continuous glass-melting tank equipped with an *EMB* system of five intermediate coils and six boosting electrodes. The coils are placed underneath the bottom of the tank, i.e. embedded in the thermal insulation of the tank bottom.

Since \mathbf{J} flows horizontally from one electrode to the other within the glass melt and \mathbf{B}_C is introduced vertically into the glass melt. The direction of \mathbf{f}_{La} can be orientated either with or opposite to the main direction of flow within the tank, depending on the electric current polarity applied to the coils. It is very important to apply the same frequency to the coil current \mathbf{I}_c as the frequency of the electrode current \mathbf{I}_E in order to synchronize the phase alteration, so that the additionally generated Lorentz forces always run in the predetermined direction. The intensity of the electromagnetic barrier is readily controllable as the \mathbf{f}_{La} magnitude is adjustable by the

\mathbf{B}_c magnitude (see Equation (4.1)). Hence, the external control parameter for *EMB* is the electric current passed through the coils \mathbf{I}_c . The desired *EMB* effect would be an *increase* in the *MRT* and consequently *improving* of the *RTD*, and finally an enhancement of the glass quality.

4.2 Aim and objectives of the thesis

It is the author's aim in this thesis to present his numerical realisation of electromagnetic boosting (EMB) in a continuous glass-melting tank, together with an assessment of the EMB effects, so as to lay the foundation for converting the idea into an effective industrial process.

This is a challenging aim because a *highly complex* three-dimensional problem is involved. In its solution, it is necessary to pursue five objectives.

The first objective is to derive a simplified representation of the actual glass-melting furnace as the basis for an academic numerical model. This necessitates deriving the mathematical model that describes the three-dimensional problem considered. The industrially available numerical models of actual continuous glass-melting tanks comprise the melting tank model with additional sub-models for the batch melting and combustion chamber. A combination of several special purpose software packages is used. However, for this academic investigation it is more useful to consider a tank model with simplified boundary conditions to reduce the simulation complexities. This approach serves the goal of the model, which is to investigate the pure *EMB* effects and study certain parameters by which the system can be analyzed and optimized.

The second objective is to develop a reliable numerical methodology for coupling the electromagnetic, flow, and temperature fields. The mathematical model of the problem considered involves the conservation laws of momentum, mass, and energy. It also involves the governing equations of the electromagnetic aspect. The necessity for strong coupling of the calculations arises from the temperature-dependent glass properties. The dynamic viscosity $\eta(T)$ and mass density $\rho(T)$ of molten glass decrease with temperature, while the electrical conductivity $\kappa(T)$ increases with temperature. Furthermore, the temperature dependence of $\eta(T)$ and $\kappa(T)$ is nonlinear. Thus, the temperature distribution within the glass melt $T(x,y,z)$ determines the localized value of the electrical conductivity of the glass melt $\kappa(T)$, which, in turn, determines the Lorentz force density distribution $\mathbf{f}_L(x,y,z)$ as well as the electric current density distribution $\mathbf{J}(x,y,z)$ within the glass melt. The Lorentz force density distribution affects the glass melt flow, i.e. the velocity distribution $\mathbf{u}(x,y,z)$, which, in turn, has an important influence on the temperature distribution within the glass melt. Figure 4.3 illustrates how the three fields interplay in a closed loop. As the underlying nonlinear system of governing equations is strongly coupled, it becomes necessary to employ a reliable numerical methodology that can effectively solve the coupled nonlinear three-dimensional problem.

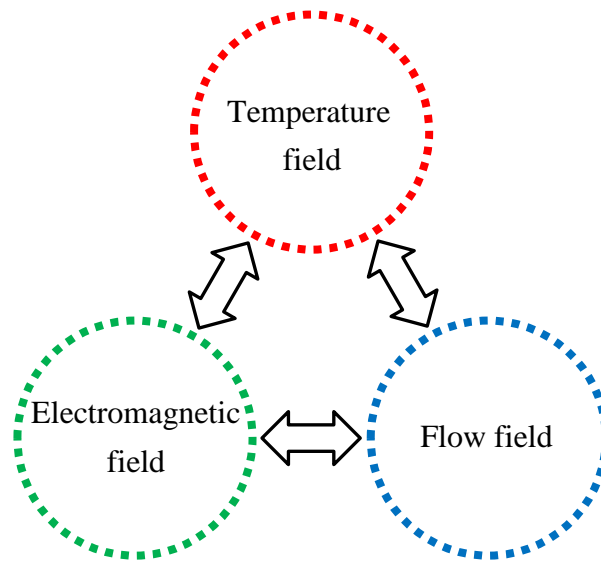


Figure 4.3: Interplay between the temperature, flow, and electromagnetic fields in a glass-melting tank with additional electromagnetic flow control.

The third objective is to adapt a circuit arrangement for operating the magnet coils in such a way that they realize the *EMB* concept. The complexity arises from the electric current patterns that are already existing within the glass melt, as the electrodes are energized by a distributed three-phase AC system using a different electrical phase for each electrode. The goal of the magnet coils system is to produce well-adapted magnetic flux densities, so that the Lorentz forces always run against the main flow direction within the glass-melting tank. This requires an appropriate electrical system for operating the magnet coils using a different electrical phase for each coil.

The fourth objective is to optimize the adapted magnet coils system to obtain the best possible *EMB* effects and, thus, to achieve the optimum process conditions. In this respect, systematic parameter studies are required to compare *EMB* effects under variable operating conditions. As the main desired *EMB* effect is an increase in the *MRT*, this will be the basic criterion for the optimization process.

All these objectives serve the purpose of establishing a numerical representation of *EMB* in the continuous glass-melting tank.

A fifth and final objective is the formulation of an academic evaluation of *EMB* effects on tank operation. Prerequisite to the objective are criteria on which reliable assessment of tank performance can be based. It will be necessary to analyze *RTD* in the simulated glass-melting tank and compare the cases with and without *EMB*, i.e. to investigate the dynamic regime behavior. This final objective serves the purpose of evaluating *EMB* in continuous glass-melting tanks.

4.3 Overview of the thesis

This thesis with its numerical simulation provides the *groundwork* for the use of the novel and innovative *EMB* approach to improve the *RTD* in electrically boosted continuous glass-melting tanks. In the simulation, an additional magnet coils system is adapted and assumed to be installed into the tank to generate additional Lorentz forces within the glass melt. These forces act against the main flow direction of the glass melt in the tank. The influence of the additionally generated Lorentz forces on the *RTD* in a continuous glass-melting tank is systematically studied using three-dimensional numerical simulations based on the geometry of a real industrial glass-melting tank. Furthermore, the physical properties of soda-lime glass are taken into account: the temperature dependence of the electrical conductivity, the dynamic viscosity, and the mass density. The tank performance with and without *EMB* is compared, to investigate the feasibility of *EMB* in continuous glass-melting tanks. The optimum operating conditions are also sought with a view to optimizing the *EMB*.

The literature on the subject is referred to in Chapter 5. The literature draws its relevance from two aspects, namely numerical simulation of glass-melting tanks and Lorentz forces in glass manufacture. Both aspects lead to useful conclusions and possible approaches.

Following the literature review, Chapter 6 presents the model for the tank under consideration, deriving therefrom the appropriate mathematical model. This describes the physical phenomena which characterize the operation of the tank. It also defines the real three-dimensional problem by means of a system of equations.

Chapter 7 presents the numerical methodology employed to couple the calculations. Calculations of simplified examples to validate and test the method are also provided in this chapter. The methodology adapted is to include the electromagnetic field calculation in software which was developed for calculating coupled hydrodynamic and thermodynamic effects, the commercial program FLUENT. This numerical methodology was first applied in [27] with highly simplified considerations, which were later systematically developed to the complete system in [28–31]. In these developments, the author was a member of the investigative team.

In Chapter 8, the author presents details of the computational grid, followed by a discussion of the numerical solution for the governing equations. The chapter concludes with different systematic studies by which the numerical accuracy is verified.

The numerical simulation of the actual continuous glass-melting tank is the subject of Chapter 9. The boundary conditions are so defined as to simulate the realistic conditions in the tank. The chapter also contains a determination of the circuit arrangement for operating the magnet coils so as to realize the *EMB* concept. There are parameter studies to establish the optimum process conditions. The simulation results are thoroughly discussed and comparisons are made, indicating a fruitful investigation. In the last section of Chapter 9, an additional fact is taken

into account: the structural steel of the tank construction. This is relevant to the installation of additional magnet coils. The fact that the magnetic field is generated near steel construction elements requires exploration.

The last chapter, Chapter 10, presents the conclusions and outlook.

The work and its main results have been published at events in [32–34] and in a peer-reviewed international scientific journal [35]. The tank simulations and their results have also been presented, discussed and published at specialized conferences of the international glass industry [36–38] and at the specialized conference on ANSYS numerical simulation [39].

5 Literature, state of the art

Here follows a comprehensive survey of the literature on subjects that are relevant to the present work. The literature falls into two groups, namely that relating to numerical simulation of glass-melting tanks and that on Lorentz forces in glass manufacture. The author draws the content into a presentation of the state of the art in each field.

5.1 Numerical simulation of glass-melting tanks

There is constant demand for better glass quality and lower glass processing costs. The demand can only be met by full insight into the glass melting process. Numerical simulation is already a tried and trusted tool in the glass industry. With the advent of the computer in the second half of the 20th century, mathematical models could come into practical use for glass-melting tanks.

The evolution of simulation tools which have been used to model glass-melting furnaces is outlined in [40]. An overview of mathematical modeling in glass manufacture is presented in [41–43]. The report on mathematical modeling in glass processing in [44] is particularly useful. The most influential papers on numerical simulation of glass-melting tanks are reviewed in the following.

Curran [45] did pioneering work in 1971. He formulated a two-dimensional computer model to study various electrode configurations in a hypothetical all-electric tank-furnace. Curran used contour maps in his work to visualize the isotherms and streamlines, and this is still the main means of presenting results today. This two-dimensional simulation was followed by another work of Curran [46], in which he studied the effects of various glass colors. He used Rosseland approximation to derive an effective thermal conductivity for the glass melt, which has been successfully employed ever since. Additional progress in the two-dimensional models came when Austin & Bourne [47], followed by Leyens [48], Mase & Oda [49], and Mardorf & Woelk [50] included the calculation of the batch feeding and melting.

Leyens & Smrček [51] studied the effects of the feeding rate and tank depth on *RTD*, while the papers published by Leyens et al. [52] and Nolet [53] included tracer studies performed on operating furnaces to compare the *RTD* with the predictions of two-dimensional mathematical models. Indeed, they found good agreement.

An early attempt at a three-dimensional numerical model of glass-melting furnaces was made by Chen & Goodson [54] in 1972. Their purpose was only to develop an efficient computational approach, using a highly simplified furnace model, as the limits of computational capacities at that time restricted the computation of realistic three-dimensional models for glass-melting fur-

naces. With the advent of commercial powerful computers in the early 1980's, it became possible to use three-dimensional models for analyzing glass process. The newly established method was employed to study a variety of glass furnace problems. An early three-dimensional study by Moulton [55] concentrated on the throat region of the glass-melting furnace. Simonis et al. [56] considered the influences of the glass flow rate, of bubbling, and of electric boosting. Ungan & Viskanta [57,58] developed a coupling of the combustion, batch melting, and tank models. They also used their coupled models to study the effects of electric boosting and air bubblers in the glass-melting furnace. Choudhary [59,60] developed a three-dimensional model and with it studied an all-electric furnace. While Ghandakly & Curran [61] developed a technique to model the electrical resistances between the electrodes in electric glass-melting furnaces. Murnane et al. [62] analyzed a variety of glass processing problems. Further papers [63–68] also appeared in the field of mathematical modeling of industrial glass-melting furnaces. The various authors of these papers addressed the control of the glass melt flow by evaluating the effects of bubbling, electric boosting, barrier wall, natural convection, and electrode arrangements. In other papers, for instance [69], the energy balance in glass-melting furnaces was described. Gopalakrishnan et al. [70] investigated time-dependent electrode energizing to improve the mixing in an all-electric glass-melting furnace.

In order to establish a benchmark test for the modeling of glass-melting tanks, the Technical Committee 21 (TC 21) of the International Commission on Glass (ICG) ran the first Round Robin Test (RRT1), in which a very simplified glass-melting tank was considered. The purpose was to test tank simulation codes by comparing the calculated velocity distributions, temperature distributions, and *MRT*'s. The results submitted by the participants were compared and published by Muschick & Muysenberg [71]. Moukarzel et al. [72] recalculated the RRT1 using the commercial software FLUENT, and demonstrated the importance of numerical precision for *MRT* calculation.

Many of the publications discussed the calculation and analysis of *RTD* in glass-melting tanks. The authors of [56,60], obtained the *RTD* by simulating a tracer experiment. This method was found to have the disadvantage of slow calculation and low accuracy. An alternative powerful method that involves performing particle tracing was applied in [64,65,72,73]. This method was found quick and accurate and, furthermore, able to provide information on *MRT* and particle path. In the last decades, the validation of mathematical models using data of operating glass-melting tanks has often been the subject of papers and has shown that the results reasonably agree with practical observations. The authors are agreed that qualitatively good predictions are attainable from numerical simulation, see [52,53,65,68,74–76].

Conclusions drawn from numerical simulation of glass-melting tanks

Today's mathematical models, as is shown in the progression recounted above, are becoming more accurate than physical models to simulate glass-melting tanks and they are replacing them

increasingly. This arises from their ability to use the real glass material properties which are usually provided by measurements, and to address the real processing conditions in the furnace. Numerical simulation using CFD models is shown in the literature to be a reliable tool for optimizing the operating parameters of the glass-melting tank, predicting glass quality, and evaluating new configurations and designs. The calculation technique most often applied is the Finite Volume Method (FVM), which is widely available in such commercial software programs as FLUENT. So far, there is no simulation tool that completely covers all processes in glass technology. Hence, in the literature, the CFD models are linked with additional sub-models to include the calculations of combustion and batch melting processes, using thus several special purpose software packages. For purposes of better control of the flow of the glass melt, numerical simulation has been used to study the effects of natural convection, bubbling, electric boosting, and electrode arrangements. The importance of *MRT* as a critical parameter for evaluating glass quality has also been emphasized in the literature by authors who studied and analyzed *RTD* to understand the flow behavior within the tank and to evaluate the tank performance. The particle tracing technique, as also reported in the literature, offers a reliable and powerful numerical method to calculate *RTD* and to provide the particle path and *MRT*.

5.2 Lorentz forces in glass manufacture

Two types of Lorentz forces are known in glass manufacture, and are distinguished by their origin. The one type occurs naturally in directly electrically heated glass melts, and is referred to as “natural Lorentz force”. The other type is artificially imposed on the electrically heated glass melts to obtain control of the flow, and is referred to as “artificial Lorentz force”.

5.2.1 Natural Lorentz forces

When glass melt is electrically heated using rod electrodes, Lorentz force densities arise naturally in the vicinity of the heating electrode. The natural Lorentz force density \mathbf{f}_{Ln} is induced when the radial electric current density \mathbf{J} , which is flowing from the electrode into the glass melt, interacts with the magnetic flux density \mathbf{B}_E called “eigenfield” which is induced by the electric current passing through the electrode itself:

$$\mathbf{f}_{Ln} = \mathbf{J} \times \mathbf{B}_E. \quad (5.1)$$

As illustrated in Figure 5.1, the natural Lorentz forces always run towards the tip of the electrode, causing an extra flow component in the tiny area surrounding the electrode.

The contribution of natural Lorentz forces as a flow component was initially neglected in the computations of flow and heat transfer in electrically heated glass melts. However, in 1991, Hofmann & Kaliski [77] indicated the importance of considering natural Lorentz forces as a second driving force beside buoyancy in the immediate vicinity of the electrodes. Moreover,

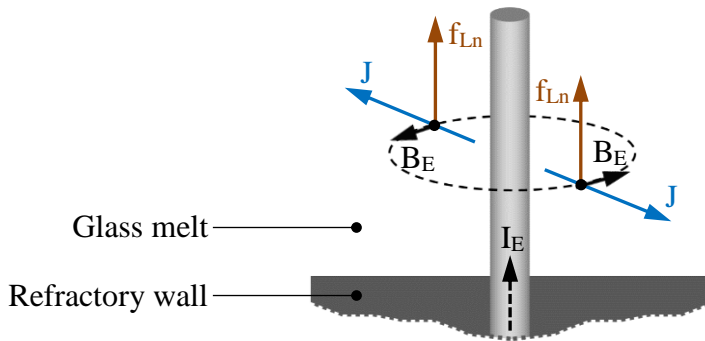


Figure 5.1: Schematic to illustrate the generation of natural Lorentz force density f_{Ln} in the electrode vicinity in directly electrically heated glass melts; \mathbf{J} : electric current density within the glass melt, \mathbf{B}_E : magnetic flux density induced by the electric current \mathbf{I}_E which is flowing through the electrode.

they showed that in physical models the similarity criteria of the natural Lorentz forces cannot be fulfilled. Hofmann & Philipp [78] demonstrated the importance of including the natural Lorentz forces in mathematical models of glass melt flow. They described the effect of the natural Lorentz force in all-electric glass-melting furnaces with different electrode arrangements. Furthermore, to simplify the discussion they assumed electric current and magnetic flux densities in the glass melt. Philipp & Hofmann [79] stated that in the case of an electrically boosted continuous glass-melting tank, an increase in the maximum upward velocity near the electrodes is calculated when the natural Lorentz force is taken into account. This leads to a considerable decrease in the *MRT*. Choudhary [80] developed a mathematical formulation for an axisymmetric model, consisting of a cylindrical volume of glass melt around a single electrode. The formulation calculates the natural Lorentz forces by solving transport equations for the magnetic field intensity. In a later paper [81], Choudhary used the model to evaluate the relative importance of buoyancy and natural Lorentz force as the driving forces in the vicinity of an electrode. More results presenting the effect of natural Lorentz forces in directly electrically heated glass melts were also published in [82] by Hofmann & Thess and in [83] by Hofmann.

Conclusions drawn from natural Lorentz forces in glass manufacture

Although the natural Lorentz forces has been neglected in the most publications on the modeling of glass-melting tanks with direct electric heating, it is proved in some few papers that it is in most cases important to take their effect into account. The natural Lorentz force effect has been emphasized in the case of continuous glass-melting tanks that are electrically boosted using bottom electrodes. Such tanks are the focus of the present work.

5.2.2 Artificial Lorentz forces

While flow control using Lorentz forces is a widely applied technology in many metallurgical processes, no use of Lorentz forces in glass manufacture has yet become established. The difficulty arises from the relatively small electrical conductivity of molten glass (about five orders of magnitude less than molten metals). Therefore, in glass processing, the essential effect of electric current is to generate Joule heat within the glass melt. However, a number of proposals has been made for applying artificial Lorentz force in glass manufacture. A review follows.

There is a patent registered as early as 1932 by Bates & Haskell [84]. The inventors suggest a method for controlling the successive delivery of molten glass to forming device using artificial Lorentz forces. Furthermore, the orientation of artificial Lorentz forces is alternated to either accelerate or retard the glass melt flow through a feeder discharge passage. The inventors suggest two arrangements of annular coils with iron frames for the magnetic circuit. For the coil arrangements they suggest a two-phase winding and a distributed three-phase winding, for which they give a detailed switching diagram. According to the suggested method, the generated magnetic flux density will induce electric current density within the glass melt. However, at the suggested low frequency of 60 Hz, the induced electric currents cannot be expected to have the desired effect, because molten glass has such low electrical conductivity. Therefore, in this author's eyes, the method remains doubtful. Moreover, the patent lacks the operation requirements, i.e. the setup dimensions and the magnitudes of magnetic flux density and induced electric current density.

Forty years later, in 1972, Walkden [85] patented a method for homogenizing glass melts using artificial Lorentz forces. The given method relates to the glass melts that are electrically heated using electrodes, mainly in forehearth and all-electric furnaces. The inventor suggests different arrangements of electromagnets connected in series with the heating electrodes. The electromagnets are thus energized by the same electric current as the electrodes, using either a single-phase or a three-phase alternating current system at 50 Hz. The patent schematically describes different glass melt flow patterns obtained in a forehearth that is equipped with three heating electrodes and two additional intermediate electromagnets.

In 1981, Mikelson et al. [86] patented an arrangement for refining and homogenizing optical glasses in crucibles using artificial Lorentz forces. In this case, the arrangement consists in three pairs of electrodes and two electromagnets. The electrodes pass alternating electric current through the glass melt, and the electromagnets introduce alternating magnetic flux density into it. The electric current is sequentially changed in three directions that are perpendicular to each other. Simultaneously, the magnetic field is changed in two directions that are perpendicular to each other and to the electric current. The inventors propose a specific glass melt flow regime, which rotates the glass melt in three planes that are perpendicular to each other. The active plane alternates every few seconds according to the switching sequence that is applied to the

electric current and magnetic field. Osmanis et al. [87] obtained a further patent in which an additional suggestion is given. Here an additional high-frequency magnetic field is applied to generate vibrations in the glass melt.

Fekolin & Stupak [88] report on physical model based on the similarity theory to investigate the electromagnetic stirring in electrically heated feeders. The model comprises a channel, an electrode arrangement, an electromagnet, and a glycerin-based model liquid. The authors study the dependence of the liquid's maximum velocity in the stirring zone on the magnetic flux density magnitude at different electric currents applied to the electrodes. However, as the similarity criteria of the temperature-dependent material properties are not considered, results from such a model remains doubtful.

A theoretical view of the application of Lorentz force in glass melts has been published by Hofmann & Thess [82]. They provide an overview of the magnetohydrodynamic effects and highlight the potential for controlling glass melt flow. A later computed example is given by Hofmann in [83].

A method using artificial Lorentz forces to control the glass melt mass flow rate in feeders was patented in 2005 by Kunert et al. [89]. According to this method, the artificial Lorentz forces are orientated either in or opposite to the glass melt flow direction. This will either accelerate or decelerate the glass melt flow in the feeder channel. The inventors suggest introducing an electric current and a magnetic field simultaneously into the glass melt. These fields are perpendicular to each other and both are perpendicular to the flow direction. The concept of electromagnetically controlled mass flow rate in feeder channels has been further investigated by Giessler et al. [90–92] using a simplified representation of the system. They consider a pipe with circular cross-section to study the effects of artificial Lorentz forces on temperature distribution and velocity. To simplify the study, they use a one-dimensional analytical model [90], and validate the results by two-dimensional axisymmetric numerical simulations [91].

A first demonstration of how artificial Lorentz forces can be effectively used to stir and homogenize the glass melts in a crucible is given by Hülsenberg et al. [93] and Krieger et al. [94,95]. They use a laboratory-scale cylindrical crucible, in which two electrodes are immersed in the glass melt to introduce electric current. Furthermore, a magnetic flux density that is perpendicular to the electric current density is introduced to the glass melt using an external magnet system. Thus, artificial Lorentz forces are generated, of which the direction can be changed according to the magnetic field and electric current directions. The authors show, by experimental studies, how artificial Lorentz forces enhance both thermal and chemical homogeneity of the glass melt. The experimental measurements of temperature distribution within the glass melt are then compared with numerical results by Cepite et al. [96]. The crucible setup is also used

by Giessler et al. [92,97–99], who study the relations between velocity, temperature, and artificial Lorentz force. They formulate a simple one-dimensional analytical model in [97,98], and perform three-dimensional numerical simulations in [99].

In 2007, Halbedel et al. [100] patented a method for electromagnetically stirring and homogenizing technical glasses within the discharging channel. The inventors suggest an arrangement composed of inner and outer cylindrical electrodes enclosed by a magnet coil system. The glass discharging channel, which is an electrically conducting pipe with circular cross-section, constitutes the outer electrode. The inner electrode is a rod inserted axially into the channel. The radial electric current density within the glass melt interacts with the axial magnetic flux density generated by the coils. Thus artificial Lorentz forces are generated perpendicular to the flow direction.

Two years later, Hofmann [101] gives in his patent a method for electromagnetically mixing, degassing, and homogenizing the electrically heated glass melts. The inventor suggests applying unequal frequencies for each electric current and magnetic field, thus obtaining artificial Lorentz forces that change their direction. According to the difference value between the applied frequencies, the artificial Lorentz forces change their direction at longer or shorter intervals so that the mixing behavior will be appropriate either to degassing or to homogenizing.

Gopalakrishnan & Thess [102] report on their numerical investigation of an electromagnetic pipe mixer which is proposed for homogenizing optical glasses. The mixer is composed of an electrically conducting pipe, two inner rod electrodes energized alternately, and surrounding coils which generate an axial magnetic flux density. Another evaluation including validation by a physical model is given by Torres & Halbedel [103].

In his thesis for the German Diplom, Kelm [104] describes three-dimensional numerical simulations that are related to the *EMB* concept. The simulations are carried out for a simple arrangement composed of a magnet coil placed between two rod electrodes that are immersed in a glass melt cube. A single-phase alternating current system at 50 Hz is assumed for the electrodes and coil. Furthermore, constant glass material properties are assumed. The temperature effect and gravity term are not considered in the simulations. Kelm investigates the basic influence of artificial Lorentz forces on the glass melt flow between two boosting electrodes. The natural Lorentz forces are considered in the simulations. First, the electromagnetic field is calculated by the commercial software MAXWELL. The calculated Lorentz force densities are then exported into the commercial software FLUENT to perform the flow field calculations.

There is a recent addition to the literature by Torres et al. [105], who investigate the artificial Lorentz force application to improve the glass coloring process in forehearths. They propose an arrangement composing three rod electrodes and two magnet coils. Both are energized with a single-phase alternating current system at 50 Hz. The coils are placed underneath the forehearth refractory bottom in positions between the electrodes which are introduced into the glass melt

through the forehearth bottom. The artificial Lorentz forces are orientated in the opposite direction to the glass melt flow to induce an upward push. This improves the mixing conditions in the forehearth, ultimately resulting in a better color homogenizing process.

Conclusions drawn from artificial Lorentz forces in glass manufacture

From this comprehensive survey of the fairly limited number of publications in the field, it is concluded that Lorentz force application to control glass melt flow is still in its infancy. Some attention has been given to homogenizing the glass melt and controlling the glass melt mass flow rate using artificial Lorentz forces. Furthermore, a variety of setups has been proposed for different glass compositions. The control parameters have been the magnetic flux density, electric current density, and frequency. The investigations have been accomplished by experimental studies, physical models and numerical simulations. The published results have demonstrated the effective application of artificial Lorentz force to control glass melt flow, which provides a contactless method. However, there has been no investigation to date of other potential applications that are related to artificial Lorentz forces in glass melts, such as the improvement of *RTD* in continuous glass-melting tanks. The current work attempts to remedy this.

6 Problem formulation

This chapter presents the system under consideration and derives the governing equations to describe the three-dimensional problem in mathematical terms.

6.1 Tank representation

The author's work takes for its academic purposes a simplified model of an industrial-scale glass-melting tank used to produce container glass. The model is illustrated in Figure 4.2 and the dimensions are shown in Figures 6.1 and 6.2. The tank walls are assumed to have a uniform thickness that is equal to the sum of the thickness of the refractory and of the thermal insulation (each is assumed to be 200 mm). An equivalent thermal conductivity is assumed for the tank walls. A *simplified* tank-inlet is used for the numerical simulation. The model here applied takes a tank-inlet that is a bounded surface on the glass melt bath. The complicated chemical reactions and heat transfer within the batch are not included in the model, and the batch is assumed to be molten glass that has a constant mass flow rate with a prescribed temperature at the simplified tank-inlet.

The tank is equipped with an electric boosting system composed of six molybdenum electrodes installed through the tank bottom. The boosting electrodes are operated by a three-phase AC system at 50 Hz, using a different electrical phase for each electrode, as shown in Figure 3.3. The electric boosting system introduces a specified amount of electric power into the glass melt, which provides additional heating near the electrodes. In the model, no barrier wall is considered as the purpose is to study the pure *EMB* effects, and to compare the dynamic regime behavior with and without *EMB*. Furthermore, a case that considers the barrier wall cannot serve as a baseline for comparison with *EMB* case in which the barrier wall is essentially discarded, the comparison would not be of like with like.

The *EMB* system considered comprises five intermediate coils in addition to the six boosting electrodes, as shown in Figure 6.2. The coils are considered to be placed 200 mm under the glass melt, i.e. in the thermal insulation directly under the refractory bottom. With an outer diameter of 600 mm, the coils can be assumed to cover the area in which *EB* is less effective. In practice, the coils can be made of a copper conductor cooled by passing water through a gap inside the conductor itself. In this thesis, a square cross section with 10 mm side length is assumed for the copper conductor. 20 turns are assumed for each coil, making the coil height 200 mm in total.

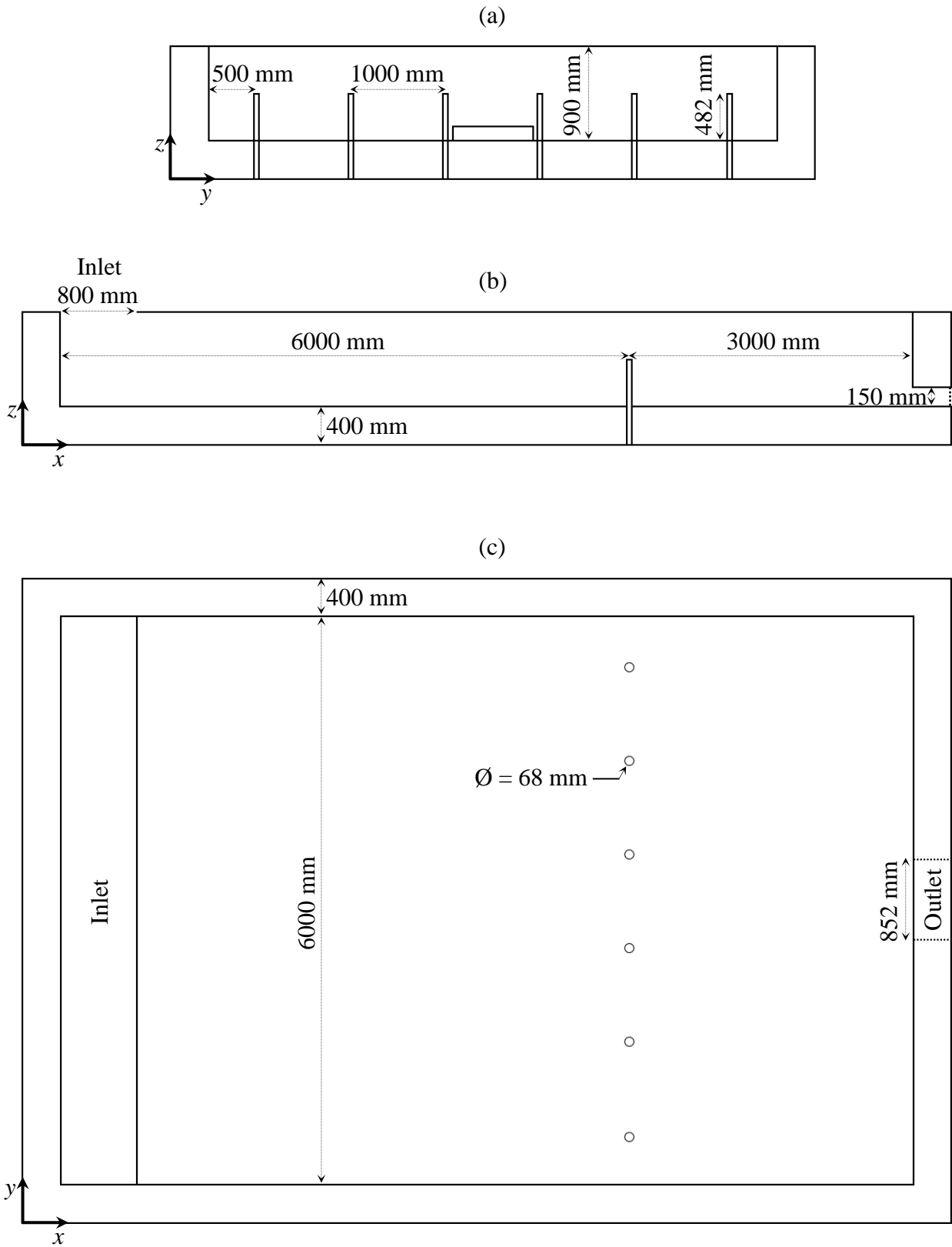


Figure 6.1: The geometric dimensions considered in this thesis for an industrial scale glass-melting tank with electric boosting: (a) front view, (b) side view, and (c) top view.

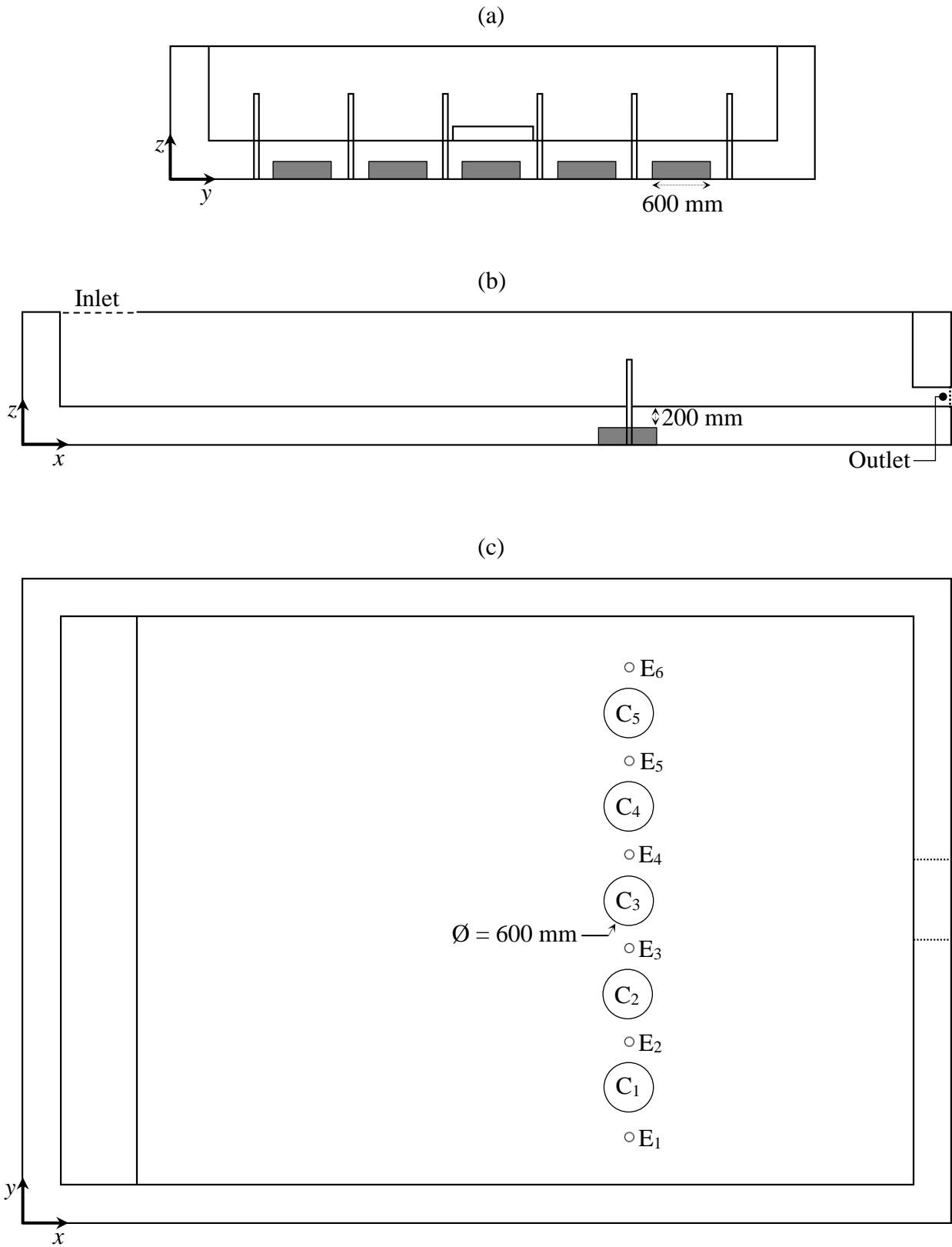


Figure 6.2: The coil dimensions and locations considered for the *EMB* system: (a) front view, (b) side view, and (c) top view. $E_{1,\dots,6}$ and $C_{1,\dots,5}$ are the electrodes and coils respectively.

6.2 Mathematical model

The mathematical model involves the equations governing the electromagnetic aspect, the glass melt flow, and the transfer of heat.

6.2.1 Glass material properties

To start with the nature of glass itself, the soda-lime glass composition known as “DGG-Standardglas Ia” [106], whose physical properties have been measured experimentally, is assumed. The glass melt has a very high dynamic viscosity $\eta(T)$ which decreases *nonlinearly* with temperature T . Furthermore, $\eta(T)$ is approximated on the base of Vogel-Fulcher-Tammann equation [13] using the logarithmic function

$$\log \eta(T) = -A + \frac{B}{T}, \quad (6.1)$$

where A and B are constants pertaining to the glass composition.

The mass density $\rho(T)$ of the glass melt decreases with temperature T , and is considered to obey the linear approximation:

$$\rho(T) = -aT + b, \quad (6.2)$$

where the constants a and b also pertain to the glass composition.

In contrast to $\eta(T)$ and $\rho(T)$, the electrical conductivity $\kappa(T)$ of the glass melt increases with temperature T . Furthermore, $\kappa(T)$ changes *nonlinearly* with T , and is approximated by the logarithmic function

$$\log \kappa(T) = C - \frac{D}{T}. \quad (6.3)$$

Again, C and D are constants pertaining to the glass composition.

Glass melt is typically considered to have an effective thermal conductivity λ_{eff} which represents a thermal conductivity for heat transfer by both radiation and conduction within the glass melt. Furthermore, effective thermal conductivity is derived by Rosseland approximation [107]. In this thesis, both λ_{eff} and specific heat capacity c_p of the glass melt are considered to be constant and independent of temperature [108].

6.2.2 Electromagnetic field

Since the AC system is applied, the complex number expression is used in describing the system [109]. The generalized Ohm's law describes how electric current density $\underline{\mathbf{J}}$ is generated in an electrically conducting media with an electrical conductivity κ [110,111]:

$$\underline{\mathbf{J}} = \kappa(-\nabla\varphi + \mathbf{u} \times \underline{\mathbf{B}} - j\omega\underline{\mathbf{A}}). \quad (6.4)$$

The gradient caused by the spatial distribution of electric potential φ within the glass melt generates the electric current density component $\kappa(-\nabla\varphi)$. It is possible that another electric current density component $\kappa(\mathbf{u} \times \underline{\mathbf{B}})$ is induced from the velocity \mathbf{u} of the conducting body in interaction with a magnetic flux density $\underline{\mathbf{B}}$. However, this component is negligible in view of the small flow velocity and the low electrical conductivity of the glass melt. A further possibility is that the time varying magnetic field may induce an electric current density component $\kappa(-j\omega\underline{\mathbf{A}})$, where $\underline{\mathbf{A}}$ is the magnetic vector potential and ω is the angular frequency of the AC system. This component is also negligible because of the low electrical conductivity of the glass melt and the low frequency, i.e. 50 Hz, used for the direct electric heating in the glass-melting tank. This means that eddy currents within the glass melt are neglected [107].

Thus, the electric current density distributed within the glass melt $\underline{\mathbf{J}}(x, y, z)$ is calculated by

$$\underline{\mathbf{J}} = -\kappa(T)\nabla\varphi. \quad (6.5)$$

The electric field $\underline{\mathbf{E}}$ is defined as

$$\underline{\mathbf{E}} = -\nabla\varphi. \quad (6.6)$$

The solenoidal nature of electric current density is described by

$$\nabla \cdot \underline{\mathbf{J}} = 0. \quad (6.7)$$

Substituting Equation (6.5) in Equation (6.7) gives the transport equation of electric potential φ :

$$\nabla \cdot (\kappa(T)\nabla\varphi) = 0. \quad (6.8)$$

The electric currents are passed through the glass melt to cause Joule heating. The average value of electric power density diffused through the glass melt is calculated by

$$p_v = \frac{1}{\kappa} |\underline{\mathbf{J}}|^2, \quad (6.9)$$

where $|\underline{\mathbf{J}}|$ is the effective value of electric current density.

According to the Maxwell-Ampere law, electric current density is surrounded by a magnetic flux density $\underline{\mathbf{B}}$:

$$\nabla \times \underline{\mathbf{B}} = \mu(\underline{\mathbf{J}} + j\omega\underline{\mathbf{D}}), \quad (6.10)$$

where μ is constant magnetic permeability and $\underline{\mathbf{D}}$ is the electric flux density.

Glass is considered to have the magnetic permeability of a vacuum μ_0 [112]. Then as the component $\mu(j\omega\underline{\mathbf{D}})$ is negligible at the low frequency of 50 Hz, the induced magnetic flux density within the glass melt $\underline{\mathbf{B}}(x, y, z)$ is calculated by

$$\nabla \times \underline{\mathbf{B}} = \mu_0 \underline{\mathbf{J}}. \quad (6.11)$$

The magnetic vector potential $\underline{\mathbf{A}}$ is defined by the magnetic flux density according to

$$\underline{\mathbf{B}} = \nabla \times \underline{\mathbf{A}}. \quad (6.12)$$

Substitution of Equation (6.12) in Equation (6.11) gives

$$\nabla \times (\nabla \times \underline{\mathbf{A}}) = \mu_0 \underline{\mathbf{J}}. \quad (6.13)$$

The magnetic flux density is mainly induced by the high electric current densities that exist within the electrodes, which forms the surrounding eigenfield (see Figure 5.1).

There is additional magnetic flux density $\underline{\mathbf{B}}_C(x, y, z)$ generated by the external coils when the electric current $\underline{\mathbf{I}}_C$ is passed through them. This is calculated according to the Biot-Savart law:

$$\underline{\mathbf{B}}_C(\mathbf{r}) = \frac{\mu_0}{4\pi} \int_l \frac{\underline{\mathbf{I}}_C(\mathbf{r}') \times (\mathbf{r} - \mathbf{r}')}{|\mathbf{r} - \mathbf{r}'|^3} dl'. \quad (6.14)$$

The Biot-Savart law calculates the magnetic flux density $\underline{\mathbf{B}}_C$ at a position vector \mathbf{r} due to a current element $\underline{\mathbf{I}}_C dl'$ at a position vector \mathbf{r}' . This is an analytical solution for a domain with constant magnetic permeability $\mu = \mu_0$.

The total magnetic flux density within the glass melt is thus $\underline{\mathbf{B}}_{\text{Total}} = \underline{\mathbf{B}} + \underline{\mathbf{B}}_C$.

The alternating electric current density $\underline{\mathbf{J}}(t)$ and total magnetic flux density $\underline{\mathbf{B}}_{\text{Total}}(t)$ interact with each other, generating Lorentz force density within the glass melt:

$$\underline{\mathbf{f}}_L(t) = \underbrace{\text{Re}\{\underline{\mathbf{J}} \times \underline{\mathbf{B}}_{\text{Total}}^*\}}_{\text{Direct component}} + \underbrace{\text{Im}\{\underline{\mathbf{J}} \times \underline{\mathbf{B}}_{\text{Total}}\}}_{\text{Alternating component}} \cos(2\omega t). \quad (6.15)$$

$\underline{\mathbf{f}}_L(t)$ consists of a direct (time averaged) component and a component that alternates with doubled frequency, i.e. 100 Hz. However, the high inertia of glass melt means that the alternating component is negligible. The Lorentz force density distributed within the glass melt $\underline{\mathbf{f}}_L(x, y, z)$ is thus calculated from the direct component only:

$$\mathbf{f}_L = \operatorname{Re} \left\{ \mathbf{J} \times \mathbf{B}_{\text{Total}}^* \right\}. \quad (6.16)$$

It should be noted that the effective value is considered for the electric current density and magnetic flux density in Equations (6.15) and (6.16).

6.2.3 Flow and temperature fields

Problems related to the distribution of velocity and of heat in fluids are solved using a set of equations based on mass, momentum, and energy conservation laws. The general form of a conservation law is $U(t) + F = D + S$, made up of an unsteady term $U(t)$, a convective term F , a diffusive term D , and a source/sink term S . In the S , sources have a positive sign, while sinks have a negative sign. The conservation laws are usually expressed by partial differential equations which are obeyed in every infinitesimal volume dV .

Continuous glass-melting tanks are assumed to have *steady-state* behavior. This implies that the distribution of velocity and of temperature does not change with time and depends only on position (x,y,z) . Therefore, the unsteady term in the conservation law is zero $U(t) = 0$.

Glass melt flow is generally assumed to be incompressible as the temperature dependence of glass mass density ρ is weak. Buoyancy force, however, is taken into account in the calculation of the glass melt flow. Thus, the velocity distribution within the glass melt $\mathbf{u}(x,y,z)$ is determined by solving the momentum equation [107]

$$\underbrace{\rho(\mathbf{u} \cdot \nabla)\mathbf{u}}_{\text{Convection}} = \underbrace{\nabla \cdot (\eta(T)\nabla\mathbf{u})}_{\text{Diffusion}} - \underbrace{\nabla p + \rho(T)\mathbf{g} + \mathbf{f}_L}_{\text{Source/Sink}}, \quad (6.17)$$

where \mathbf{u} is the velocity vector, ∇p is the pressure force density, $\rho(T)\cdot\mathbf{g}$ is the gravitational force density, and the Lorentz force density \mathbf{f}_L is manifested as an additional source.

Mass conservation in the glass melt is described by the continuity equation for incompressible flow

$$\nabla \cdot \mathbf{u} = 0. \quad (6.18)$$

Thus, the temperature distribution within the glass melt $T(x,y,z)$ is determined by solving the energy equation [107]

$$\underbrace{\rho c_p (\nabla \cdot (\mathbf{u}T))}_{\text{Convection}} = \underbrace{\nabla \cdot (\lambda_{\text{eff}} \nabla T)}_{\text{Diffusion}} - \underbrace{q_{\text{cool}}'' + p_v}_{\text{Source/Sink}}, \quad (6.19)$$

where Joule heat density p_v (Equation (6.9)) and the local volumetric cooling due to the wall heat losses q_{cool}'' appear as the source/sink term of the energy equation, in that the tank walls have a cooling influence on glass melt in contact with them and heat passes through the tank walls by means of conduction and leaves their outer surfaces by means of convection and radiation.

Heat flux within the tank walls is calculated by Fourier's law

$$\mathbf{q}_w'' = -\lambda_w \nabla T, \quad (6.20)$$

where \mathbf{q}_w'' is the heat flux vector, λ_w is the equivalent thermal conductivity of the walls, and ∇T is the temperature gradient [113].

The surface of the walls at a temperature T_S exchanges thermal energy with the surroundings at an ambient temperature T_∞ . Convective heat transfer rate q_{conv} is calculated by Newton's law of cooling

$$q_{conv} = h A_S (T_S - T_\infty), \quad (6.21)$$

where h is the heat transfer coefficient which is considered for air in this case, and A_S is the surface area of the walls. Radiative heat transfer rate q_{rad} from a surface is calculated according to

$$q_{rad} = \sigma_B \varepsilon A_S (T_S^4 - T_\infty^4), \quad (6.22)$$

where σ_B is the Stefan-Boltzmann constant and ε is the surface emissivity [114]. It should be noted that Equation (6.22) represents a special case for a surface surrounded by an outer surface with infinite area or with emissivity $\varepsilon = 1$.

Thus, the heat transfer rate from the tank walls to the surroundings is

$$q_{cool} = q_{conv} + q_{rad}. \quad (6.23)$$

7 Numerical methodology

Here the subject is the numerical approach employed to couple the calculations, followed by test-simulations which form part of the model developing process. The test-simulations are performed using simplified examples intended to validate and test the numerical approach.

7.1 Coupling the calculations

Numerically solving the coupled nonlinear system of equations presented in Chapter 6 would require a simulation tool that is able to calculate coupled electrodynamic, thermodynamic, and hydrodynamic effects. In modeling the tank, one should also take into account the huge volume of glass melt (approximately 50 m^3) and the complex flow pattern. Numerical simulation of such a system thus requires a massive computational grid consisting of several million cells.

The computational effort involved in coupling two different simulation tools with an exchange between electromagnetic field calculation on one side and flow field including temperature field calculation on the other side would be enormous. Such two-way coupling is necessary as the value of the temperature-dependent electrical conductivity must be updated in the solution domain so that the electric current and Lorentz force densities can be recalculated. Such a highly complex problem will overload even the available commercial software tools that are suitable for Multiphysics calculations.

A reliable computational approach must be found that is able to efficiently solve the problem. The approach taken is to reduce the need for numerical programming and make use of the state of the art in pre- and post-processing by implementing the electrodynamics calculation in the commercial software FLUENT. This program was developed to calculate coupled thermodynamic and hydrodynamic effects on the basis of FVM. Therewith, the governing equations for the magnetic field are referred to the general form of diffusion equation, making it thus possible to solve these equations using the same computational algorithm used for flow and temperature fields, a technique which allows all fields to be calculated iteratively in one computational procedure. There is a further advantage in using FLUENT: the possibility of calculating the coil magnetic field by analytical solution using the so-called user-defined function (UDF). It is also useful that FLUENT has a parallel solver which features solution partitioning using multiple processes that can be executed on one computer, or on different computers in a network cluster, which can significantly reduce the computational time [115].

7.2 Calculating electromagnetic field with FLUENT

FLUENT bases its solution of the partial differential equations of mass, momentum, and energy conservation on the use of FVM. FLUENT allows the solving of up to 50 user-defined scalar (UDS) transport equations [116]. For an arbitrary scalar ϕ_k , FLUENT solves the general scalar transport equation

$$\underbrace{\frac{\partial \rho \phi_k}{\partial t}}_{\text{Unsteady}} + \frac{\partial}{\partial x_i} \left(\underbrace{\rho u_i \phi_k}_{\text{Convection}} - \underbrace{\Gamma_k \frac{\partial \phi_k}{\partial x_i}}_{\text{Diffusion}} \right) = \underbrace{S_{\phi_k}}_{\text{Sources}}, \quad k = 1, \dots, N. \quad (7.1)$$

The diffusion coefficient Γ_k and source term S_{ϕ_k} are provided by the user for each of the N scalar transport equations. The idea is to calculate the electromagnetic field with FLUENT, which is an innovative use of the program. Then it is possible to calculate the electromagnetic, the thermodynamic, and the hydrodynamic effects in one computational procedure. Furthermore, the governing equations of the electromagnetic, flow, and temperature fields will thus be solved using the same kind of computational algorithm [115].

To simplify the discussion initially, what follows is the case of a direct current (DC) system. As shown in Subsection 6.2.2, electric current density is given by

$$\mathbf{J} = -\kappa \nabla \varphi, \quad (7.2)$$

and the solenoidal nature of \mathbf{J} is described by

$$\nabla \cdot \mathbf{J} = 0. \quad (7.3)$$

Substituting Equation (7.2) in Equation (7.3) gives the transport equation of electric potential φ :

$$\nabla \cdot (\kappa \nabla \varphi) = 0. \quad (7.4)$$

Electric current density induces a magnetic flux density which is given by [110]

$$\nabla \times \mathbf{B} = \mu_0 \mathbf{J}. \quad (7.5)$$

The magnetic vector potential \mathbf{A} is defined by the magnetic flux density according to

$$\mathbf{B} = \nabla \times \mathbf{A}. \quad (7.6)$$

Equation (7.6) substituted in Equation (7.5) gives

$$\nabla \times (\nabla \times \mathbf{A}) = \mu_0 \mathbf{J}. \quad (7.7)$$

Applying the vector equality $\nabla \times (\nabla \times \mathbf{A}) = \nabla(\nabla \cdot \mathbf{A}) - \nabla^2 \mathbf{A}$ to the left-hand side of Equation (7.7), one obtains [117]

$$\nabla(\nabla \cdot \mathbf{A}) - \nabla^2 \mathbf{A} = \mu_0 \mathbf{J}. \quad (7.8)$$

Furthermore, the Coulomb gauge

$$\nabla \cdot \mathbf{A} = 0 \quad (7.9)$$

reduces Equation (7.8) to the Poisson equation:

$$\nabla^2 \mathbf{A} = -\mu_0 \mathbf{J}. \quad (7.10)$$

Equations (7.10) and (7.2) lead to the transport equations for the magnetic vector potential components A_x , A_y , and A_z :

$$\nabla^2 A_x = \mu_0 \kappa \frac{\partial \varphi}{\partial x}. \quad (7.11)$$

$$\nabla^2 A_y = \mu_0 \kappa \frac{\partial \varphi}{\partial y}. \quad (7.12)$$

$$\nabla^2 A_z = \mu_0 \kappa \frac{\partial \varphi}{\partial z}. \quad (7.13)$$

To calculate electric potential φ and magnetic vector potential \mathbf{A} with FLUENT, Equations (7.4), (7.11), (7.12), and (7.13) are solved using four UDS equations. Neither the unsteady term nor the convective term in Equation (7.1) are to be considered for the four UDS equations, and they are thus set to zero: $\frac{\partial \rho \phi_k}{\partial t} = 0$ and $\frac{\partial \rho u_i \phi_k}{\partial x_i} = 0$. So, the four UDS transport equations used

Index: k	Scalar: ϕ_k	Diffusivity: Γ_k	Source: S_{ϕ_k}
1	φ	κ	0
2	A_x	1	$-\mu_0 \kappa \frac{\partial \varphi}{\partial x}$
3	A_y	1	$-\mu_0 \kappa \frac{\partial \varphi}{\partial y}$
4	A_z	1	$-\mu_0 \kappa \frac{\partial \varphi}{\partial z}$

Table 7.1: Parameter settings for the user-defined scalar (UDS) equations required to calculate electric potential φ and magnetic vector potential components A_x , A_y , and A_z in the DC system.

to calculate φ , A_x , A_y , and A_z are defined by setting the parameters for the diffusive and source terms in Equation (7.1), as shown in Table 7.1.

After that, the calculated values of φ , A_x , A_y , and A_z are used to calculate electric current density \mathbf{J} and its induced magnetic flux density \mathbf{B} using Equations (7.2) and (7.6) respectively. This is performed using UDF which can be dynamically loaded with the FLUENT solver.

Also by means of UDF, the additional magnetic flux density generated by the coils \mathbf{B}_c is calculated using the Biot-Savart law for each turn of each coil:

$$\mathbf{B}_c(\mathbf{r}) = \frac{\mu_0}{4\pi} \int_l \frac{\mathbf{I}_c(\mathbf{r}') \times (\mathbf{r} - \mathbf{r}')}{|\mathbf{r} - \mathbf{r}'|^3} dl'. \quad (7.14)$$

Equation (7.14) provides an analytical solution for a domain with constant magnetic permeability.

The total magnetic flux density is then defined as

$$\mathbf{B}_{\text{Total}} = \mathbf{B} + \mathbf{B}_c. \quad (7.15)$$

The Lorentz force density is calculated using UDF for

$$\mathbf{f}_L = \mathbf{J} \times \mathbf{B}_{\text{Total}}. \quad (7.16)$$

\mathbf{f}_L is set as an additional parameter for source term S_{ϕ_k} in the momentum equation which is solved by FLUENT to calculate the flow field.

Joule heat density caused by \mathbf{J} is calculated using UDF for

$$p_v = \frac{1}{\kappa} |\mathbf{J}|^2. \quad (7.17)$$

Likewise, p_v is set as an additional parameter for source term S_{ϕ_k} in the energy equation which is solved by FLUENT to calculate the temperature field.

7.3 Validation by numerical simulation with MAXWELL

In the modeling of a system, validation is evaluating the accuracy of the model by comparing the results with those from a different modeling approach [118,119]. Numerical models are usually validated by comparing their results with those of experiments [120]. Another possibility, when experiments or measurements are not possible, is to compare the results with those obtained by a different numerical method. This section of the present thesis is largely concerned with validating the electrodynamics calculation modeled within FLUENT. The FLUENT results are compared with that of a reference code which employs a different numerical method for the calculation of the electromagnetic field. The choice of reference software is MAXWELL, which was developed to calculate electromagnetic effects on the basis of the Finite

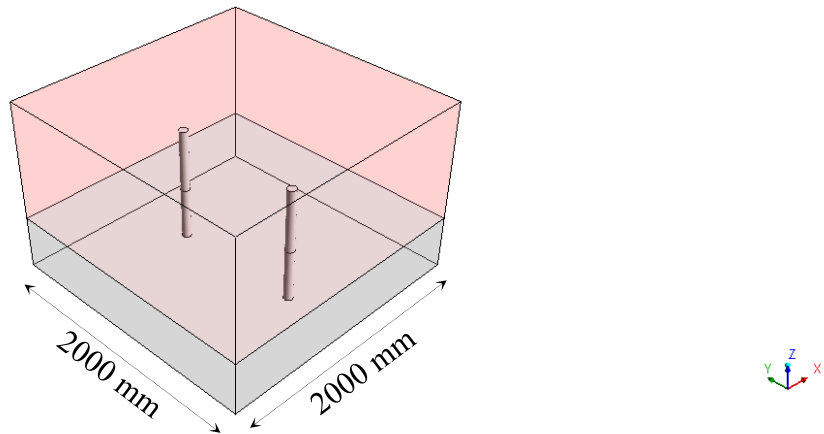


Figure 7.1: Cube-model consisting of a glass melt cube, two immersed electrodes, and a bottom wall, used for testing and validating the numerical method presented in Section 7.2.

Element Method (FEM) and is commercially available. For the validation process, a simple cube-model as a section of the tank geometry in Figure 6.1 is considered. The section comprises two rod electrodes immersed in a glass melt cube through a bottom wall, as depicted in Figure 7.1. As the aim is only to test and validate the electromagnetic field calculation performed by FLUENT, flow and temperature fields are not included in the calculations. The glass melt and the electrodes are assumed to have constant electrical conductivity, while the bottom is assumed to have no electrical conductivity. All domains are assumed to have the magnetic permeability of a vacuum μ_0 . The simulation of this test model is carried out using both MAXWELL and FLUENT to compare like with like as a means of validation.

7.3.1 Boundary conditions of the cube-model

Prescribed direct electric current of 1700 A is assumed to be flowing through the bottom-surface of each of the two electrodes, where the electric current is entering the bottom-surface of one electrode and leaving the bottom-surface of the other electrode. This is applied in MAXWELL using the “Magnetostatic” solver. In FLUENT, the electric current is defined as an electric current density on the bottom-surface of the electrodes using the “Flux” boundary condition for electric potential, and the direction of the current is defined by applying a positive sign (for entering the bottom-surface of the electrode) or a negative sign (for leaving the bottom-surface of the electrode). No additional flux is assumed in FLUENT for electric potential across the other outer boundaries. FLUENT also permits definition of the electric potential value on boundaries in the form of “Dirichlet” boundary condition by using the “Value” boundary condition. For magnetic field, “Neumann” boundary condition is assumed on all outer boundaries, which means that the magnetic field is tangential to the boundary and cannot cross it. This

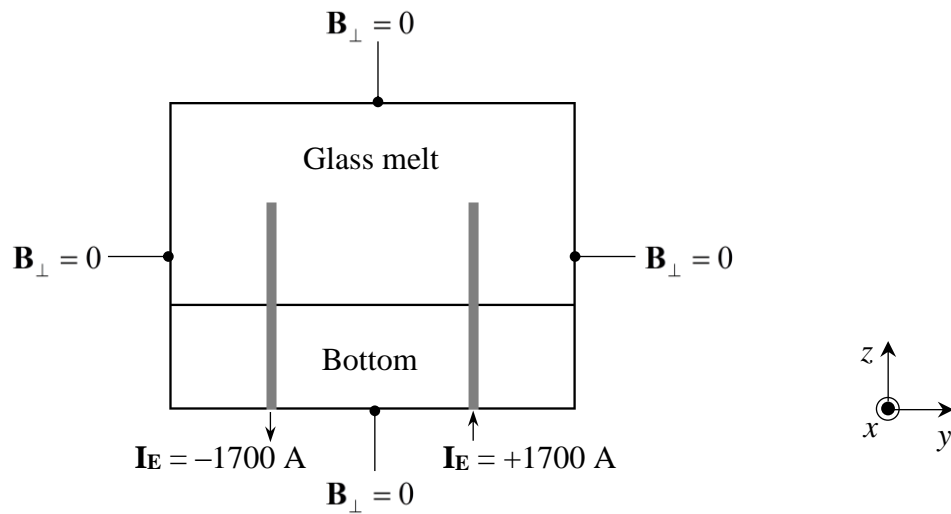


Figure 7.2: Boundary conditions of the cube-model, where \mathbf{B}_\perp is the normal component of magnetic flux density.

boundary condition is also called magnetic insulation. It corresponds to symmetry conditions where the magnetic flux density has no normal component and is applicable for keeping the solution domain relatively small. This boundary condition is set by default in MAXWELL [121]. In FLUENT, the tangential component of magnetic vector potential is fixed at zero on all outer boundaries, so that the magnetic field normal component results in zero. To help clarifying this, Figure 7.2 illustrates the boundary conditions of the cube-model. On the interfaces between objects, natural boundary condition is assumed for the magnetic field, which means that the normal component of the magnetic field is continuous across the interface boundaries.

7.3.2 Results of comparison

The main point of the validation is comparing FLUENT results with MAXWELL results in terms of electric current density \mathbf{J} , magnetic flux density \mathbf{B} , and Lorentz force density \mathbf{f}_L . The primary result of the calculations is that for electric current density. Figure 7.3 presents a magnitude comparison of the electric current density distribution within the glass melt in a vertical plane across the electrodes from each program. Within the glass melt, the most intense electric current density is in the vicinity of the electrodes. A comparison of electric current density vectors within the glass melt calculated by the two programs is also shown in Figure 7.4, in which the vectors are presented in a horizontal plane that is 50 mm above the bottom. The figure illustrates how electric current density flows through the glass melt from one electrode to the other. The vector diagram is given with the main intention of demonstrating the field direction. The vectors of electric current density in the figure are presented in normalized mode and,

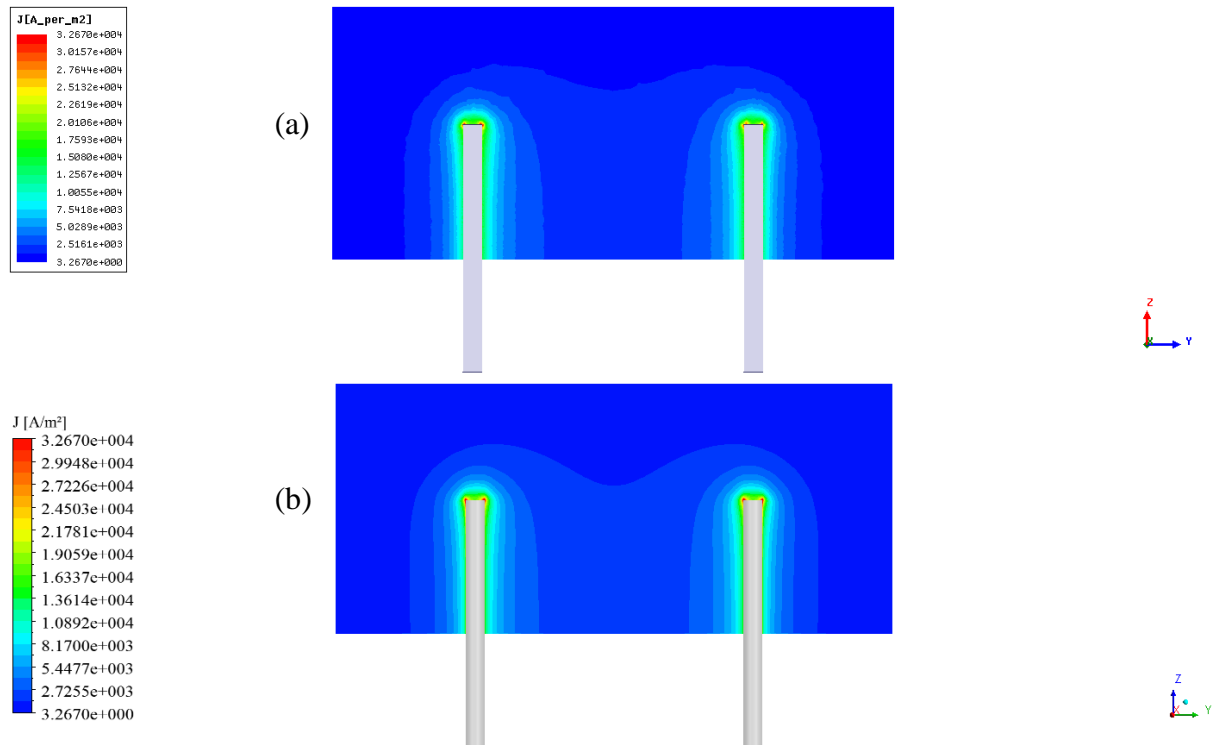


Figure 7.3: The distribution of electric current density magnitudes within the glass melt in a vertical plane across the electrodes, calculated (a) with MAXWELL and (b) with FLUENT.

therefore, they have a uniform length and their intensity is described by color scale. The small differences in vector distribution and vector size between MAXWELL and FLUENT are only due to the different software post-processing tools and have nothing to do with the accuracy of the results. An additional comparison is shown in Figure 7.5 for the magnitude of electric current density in a horizontal line between the electrodes, again at a height of 50 mm above the bottom. The comparisons presented in the figures reveal very good agreement between electric current density results. For a more quantitative comparison, the percentage total divergence d_J [%] between both electric current densities within the glass melt, calculated with MAXWELL and with FLUENT, is estimated according to

$$d_J = \frac{\left| \int_{V_{Glass}} J_{FLUENT} dV - \int_{V_{Glass}} J_{MAXWELL} dV \right|}{\int_{V_{Glass}} J_{MAXWELL} dV} \cdot 100, \quad (7.18)$$

where $J_{MAXWELL}$ and J_{FLUENT} are the electric current density magnitudes in MAXWELL and FLUENT respectively and V_{Glass} is the glass melt volume. The estimation reveals that the divergence within electric current density is very low, with $d_J = 0.341\%$.

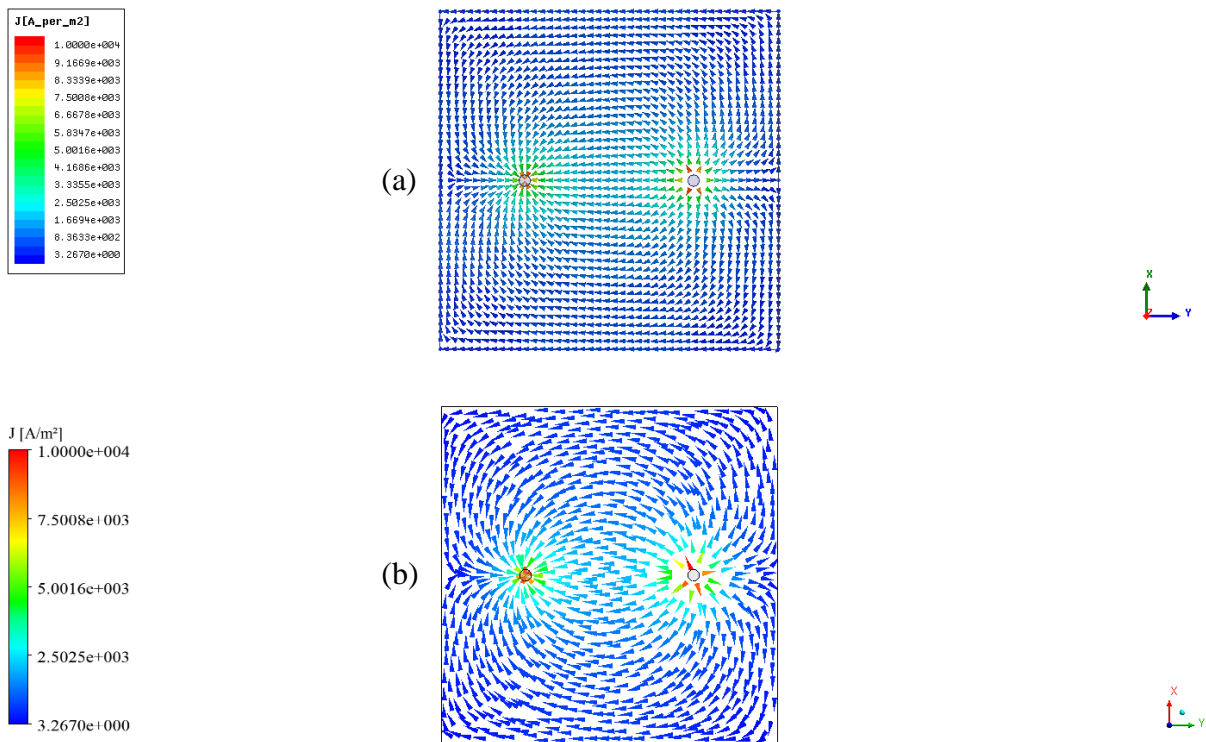


Figure 7.4: The distribution of electric current density vectors within the glass melt in a horizontal plane at 50 mm above the bottom, calculated (a) with MAXWELL and (b) with FLUENT.

Turning to the magnetic flux density, Figure 7.6 presents a magnitude comparison of the magnetic flux density distribution within the glass melt in a vertical plane across the electrodes. Magnetic flux density in the glass melt has the largest intensity in the vicinity of the electrodes with their eigenfield, induced by the high electric current density within them. A comparison of magnetic flux density vectors in the glass melt is shown in Figure 7.7, here again the vectors are presented in a horizontal plane that is 50 mm above the bottom, and the main intention is to demonstrate direction of field. The figure illustrates how the eigenfield rotates around the electrodes. Again, the small differences in the vector distribution and vector size between MAXWELL and FLUENT are only due to the different software post-processing tools, with no implications as to accuracy. An additional comparison is shown in Figure 7.8 for magnetic flux density magnitude again in a horizontal line between the electrodes at a height of 50 mm above the bottom. Here, too, the comparisons presented in the figures reveal very good agreement between magnetic flux density results for the two programs. The percentage total divergence d_B [%] between the magnetic flux densities, calculated with MAXWELL and FLUENT, is estimated according to

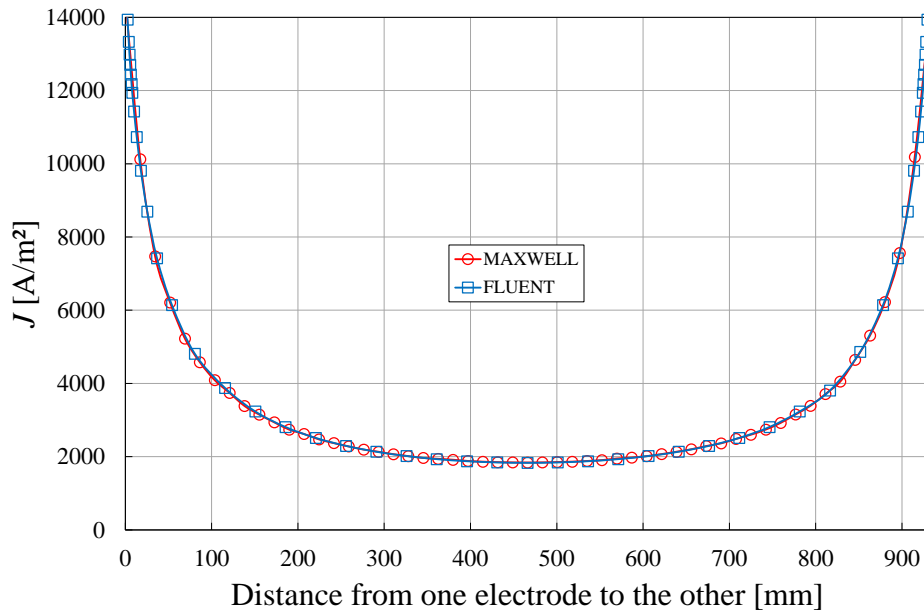


Figure 7.5: Comparison of electric current density magnitudes, calculated with MAXWELL and FLUENT, within the glass melt in a horizontal line between the electrodes at a height of 50 mm above the bottom.

$$d_B = \frac{\left| \int_{V_{Glass}} B_{FLUENT} dV - \int_{V_{Glass}} B_{MAXWELL} dV \right|}{\int_{V_{Glass}} B_{MAXWELL} dV} \cdot 100, \quad (7.19)$$

where $B_{MAXWELL}$ and B_{FLUENT} are the magnetic flux density magnitudes in MAXWELL and FLUENT respectively. The divergence turns out again to be very low, with $d_B = 0.292\%$.

For the Lorentz force density distribution, Figure 7.9 presents a magnitude comparison in a vertical plane across the electrodes. Natural Lorentz forces arise in the vicinity of the electrodes because electric current density in the glass melt is superimposed on the eigenfield induced by the currents in the electrodes. A comparison of Lorentz force density vectors within the glass melt is shown in Figure 7.10. The vectors are presented in a horizontal line that is 50 mm above the bottom, and the main point is to show the direction of field. The figure illustrates how the natural Lorentz forces run towards the electrode tip. The minor differences in the represented vector distribution are again only due to the different software post-processing tools, with no implications for accuracy. An additional comparison is shown in Figure 7.11 for Lorentz force density magnitude, in the horizontal line between the electrodes at a height of 50 mm above the

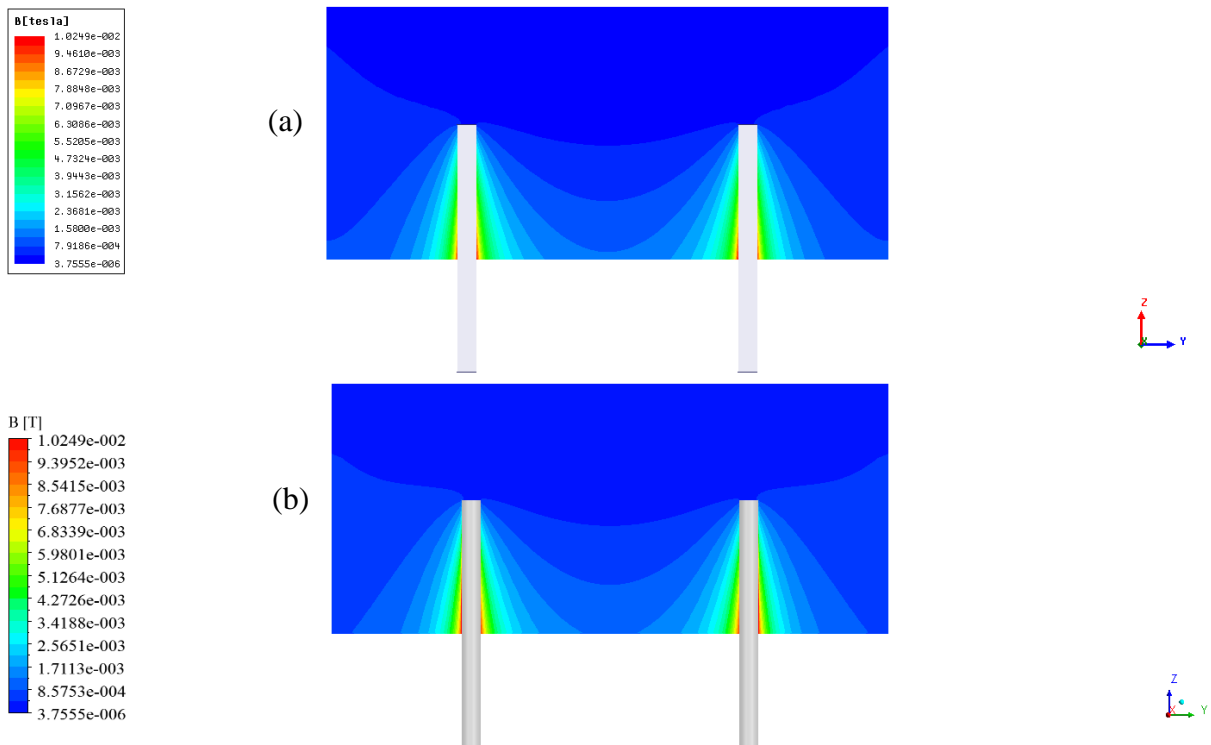


Figure 7.6: The distribution of magnetic flux density magnitudes within the glass melt in a vertical plane across the electrodes, calculated (a) with MAXWELL and (b) with FLUENT.

bottom. The Lorentz force density results compare very well. In quantitative terms, the percentage total divergence d_f [%] between both Lorentz force densities within the glass melt, calculated with MAXWELL and FLUENT, is estimated according to

$$d_f = \frac{\left| \int_{V_{Glass}} f_{FLUENT} dV - \int_{V_{Glass}} f_{MAXWELL} dV \right|}{\int_{V_{Glass}} f_{MAXWELL} dV} \cdot 100, \quad (7.20)$$

where $f_{MAXWELL}$ and f_{FLUENT} are the Lorentz force density magnitudes in MAXWELL and FLUENT respectively. Once more, the divergence is very low, with $d_f = 0.319\%$.

Conclusions drawn from validation exercise

The comparisons of electric current density \mathbf{J} , magnetic flux density \mathbf{B} , and Lorentz force density \mathbf{f}_L , between MAXWELL and FLUENT, reveal very good agreement both qualitatively and quantitatively. This suggests that the numerical method for calculating electrostatics with FLUENT as presented in Section 7.2 is reliable and can thus enable electrostatics calculation to be coupled with thermodynamics and hydrodynamics calculations. The model simulated and its boundary conditions are considered as a test-example in the context of the model developing

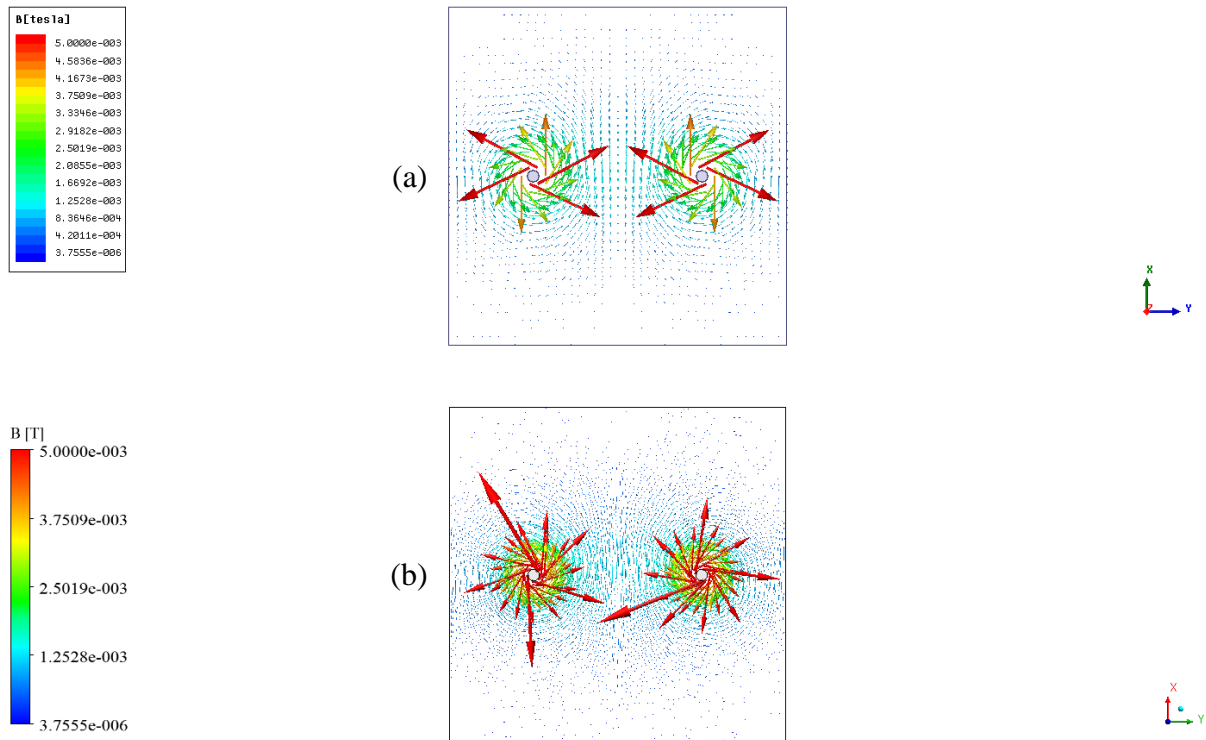


Figure 7.7: The distribution of magnetic flux density vectors within the glass melt in a horizontal plane at 50 mm above the bottom, calculated (a) with MAXWELL and (b) with FLUENT.

process, rather than as real problem simulation. The parallel solver in FLUENT certainly reduces the computational time. The divergence in results between MAXWELL and FLUENT is negligible and even this small difference is probably simply due to two different computational grids used by the different programs. The mesh in MAXWELL consists of 1 012 690 cells with a minimum length of cell edge $\text{Min. } \Delta x = 4.4 \text{ mm}$ and a maximum length of cell edge $\text{Max. } \Delta x = 176.8 \text{ mm}$, and is generated automatically with the adaptive meshing technique used by the program MAXWELL. The mesh used in FLUENT is slightly different, consisting of 615 728 cells with a minimum length of cell edge $\text{Min. } \Delta x = 1 \text{ mm}$ and a maximum length of cell edge $\text{Max. } \Delta x = 34 \text{ mm}$. This mesh is a well-structured mesh with an adapted resolution at the boundary layers and was created using the in-house program PROMETHEUS. Figure 7.12 shows the two meshes compared in a vertical plane across the electrodes.

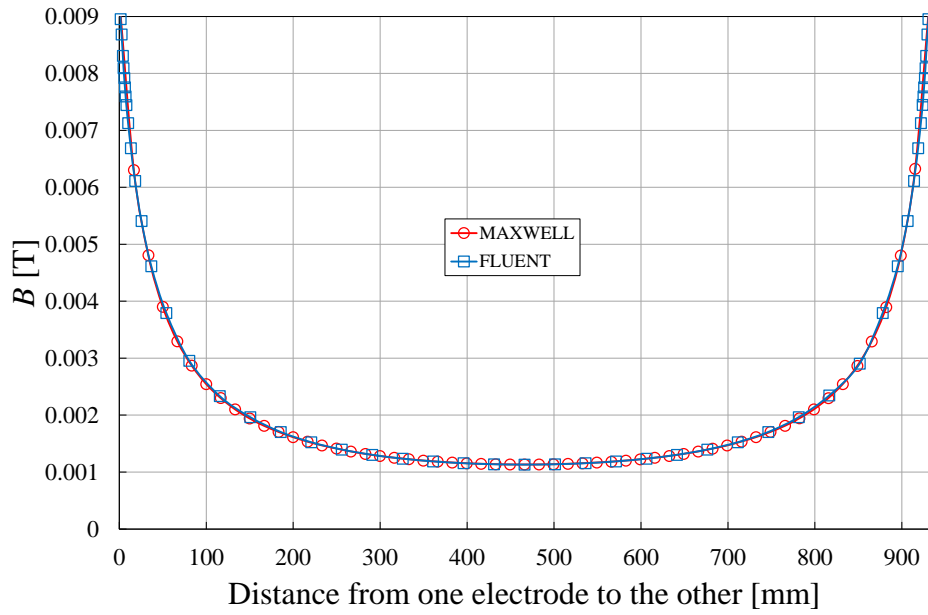


Figure 7.8: Comparison of magnetic flux density magnitudes, calculated with MAXWELL and FLUENT, within the glass melt in a horizontal line between the electrodes at a height of 50 mm above the bottom.

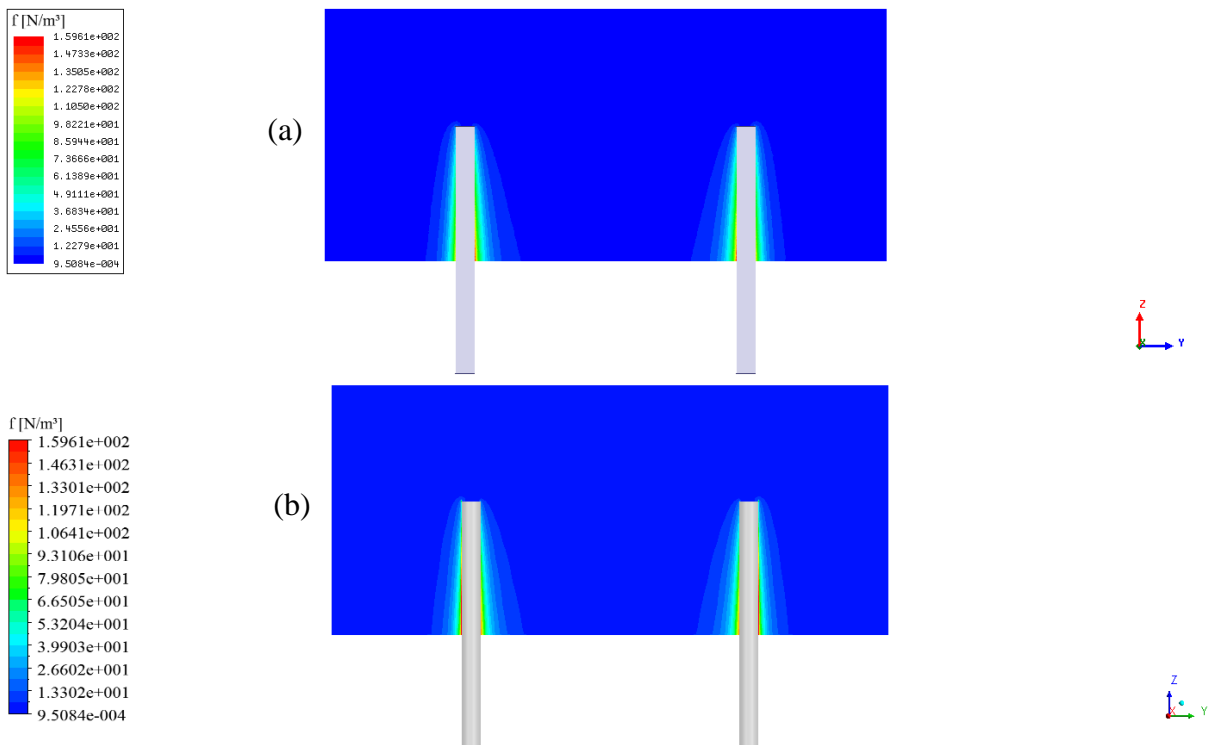


Figure 7.9: The distribution of Lorentz force density magnitudes within the glass melt in a vertical plane across the electrodes, calculated (a) with MAXWELL and (b) with FLUENT.

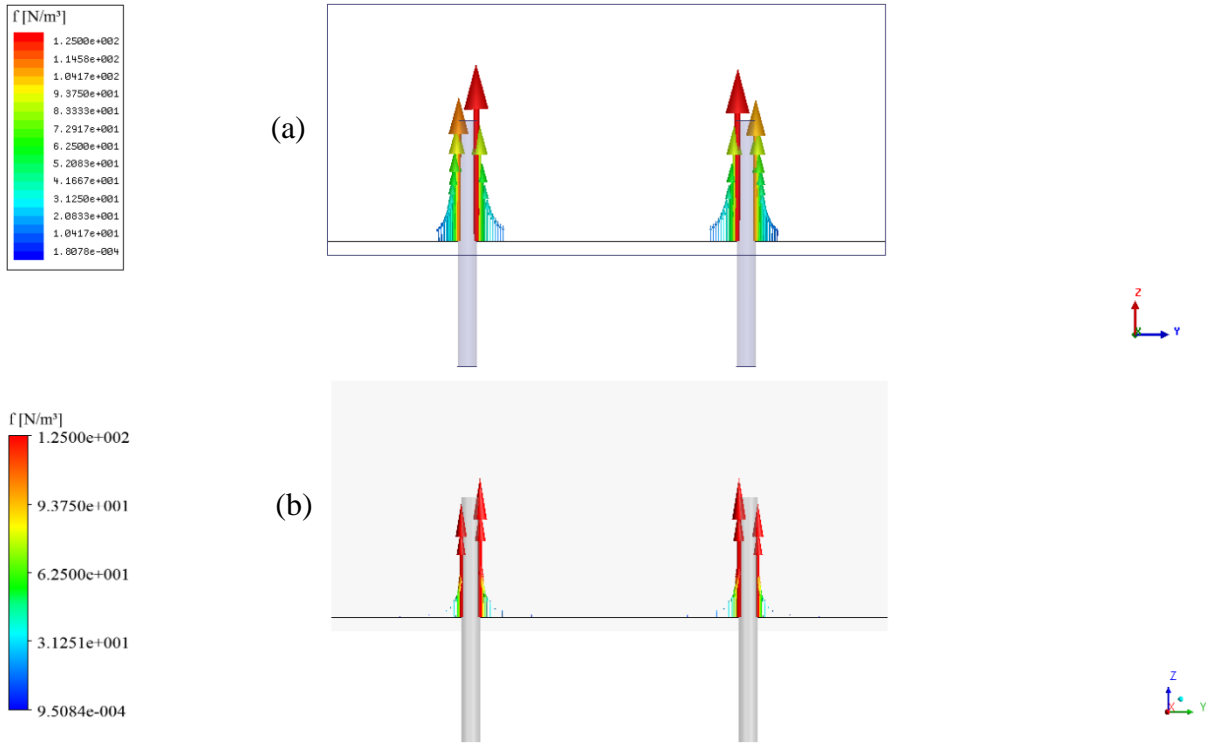


Figure 7.10: The distribution of Lorentz force density vectors within the glass melt in a horizontal line across the electrodes at 50 mm above the bottom, calculated (a) with MAXWELL and (b) with FLUENT.

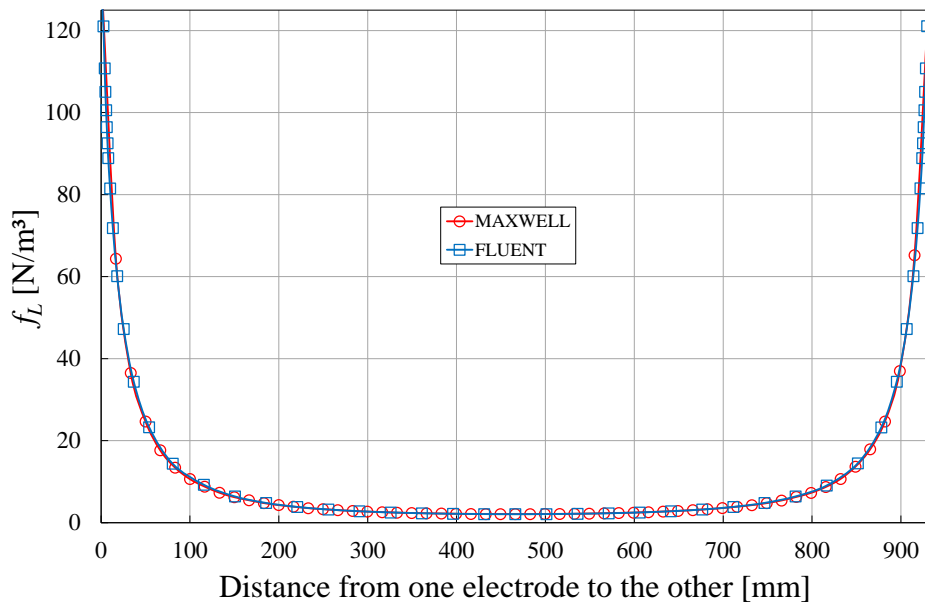


Figure 7.11: Comparison of Lorentz force density magnitudes, calculated with MAXWELL and FLUENT, within the glass melt in a horizontal line between the electrodes at a height of 50 mm above the bottom.

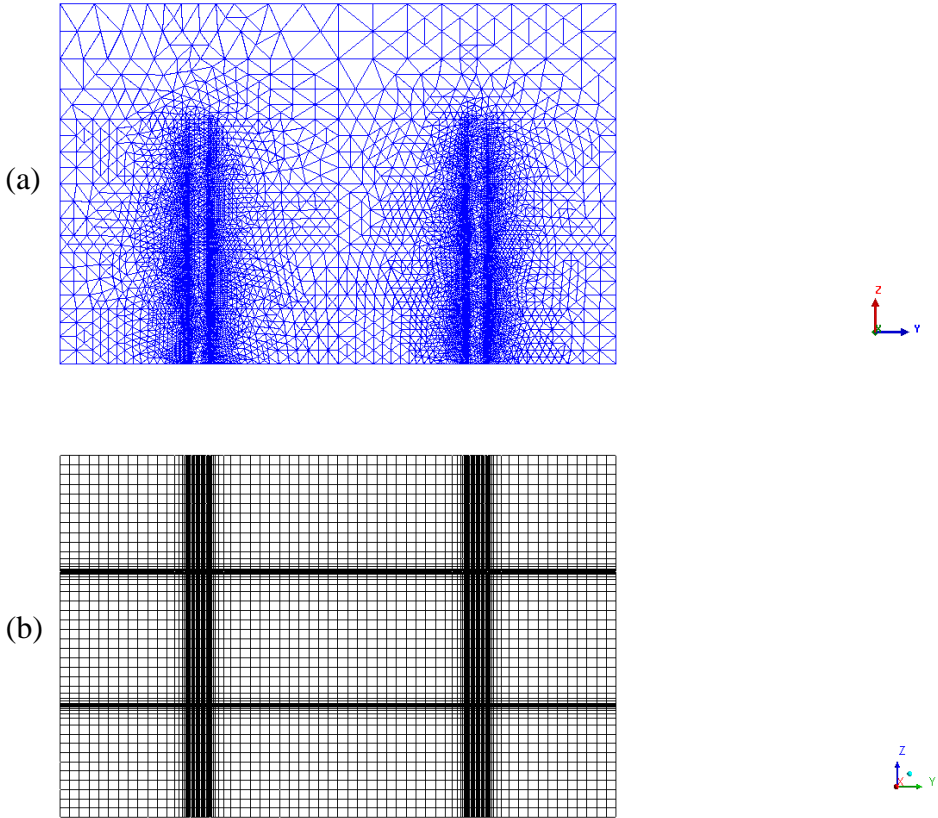


Figure 7.12: Comparison between the meshes used (a) in MAXWELL and (b) in FLUENT in a vertical plane across the electrodes.

7.4 A simplified tank model with two electrodes

Not with the intention of simulating the realistic conditions in the industrial glass-melting tank, but of implementing and testing the method described in Section 7.2 for coupling the calculations, a further model is presented in this section. It is a simple-case model to reduce both the computational difficulty and simulation complexity. There are two simple cases, namely with and without additionally generated Lorentz forces, and the simulations are performed with FLUENT. Comparing the flow conditions for both cases will give an initial indication of the

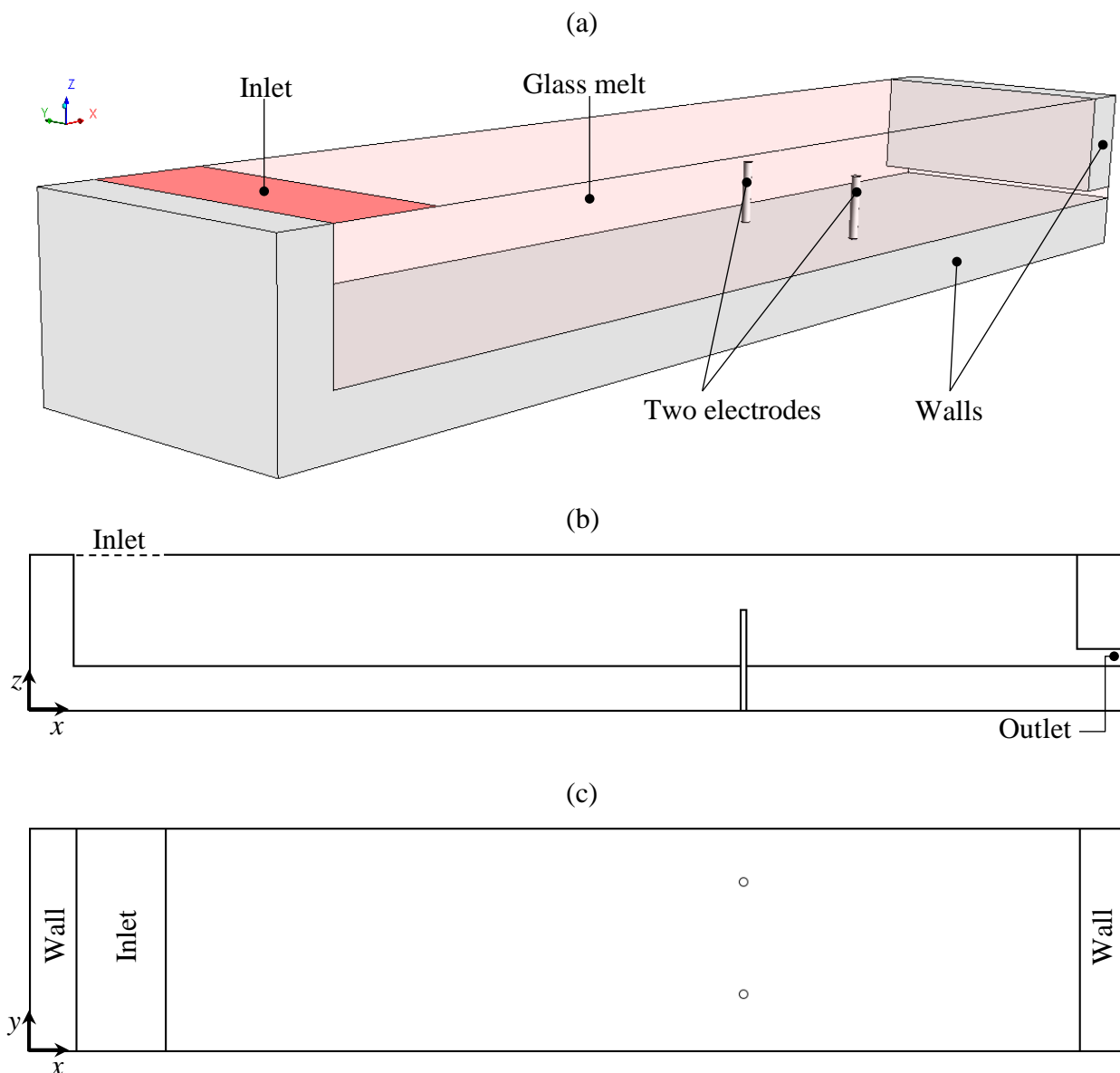


Figure 7.13: Middle-section model of the glass-melting tank used as a simple-case model, comprising glass melt, an inlet, an outlet, two boosting electrodes, and tank walls: (a) perspective view, (b) side view, and (c) top view.

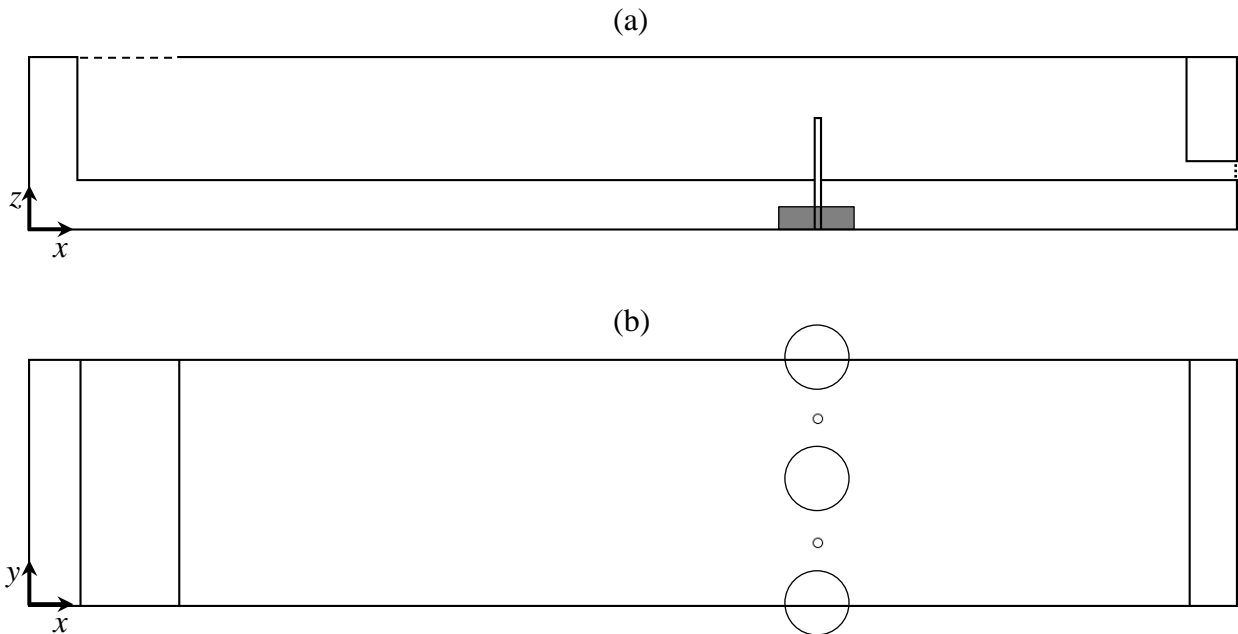


Figure 7.14: Middle-section model of the tank with three additional coils: (a) side view, and (b) top view.

potential impact of such Lorentz forces as an additional flow component within the glass-melting tank.

7.4.1 The model employed

The simplified model is that of a longitudinal section taken out from the middle of the glass-melting tank as illustrated in Figure 7.13, with a representation of the glass melt, an inlet, an outlet, two boosting electrodes and the tank walls. This middle-section model has two symmetry sides. The geometric dimensions are basically those given in Section 6.1. The glass melt is taken to be a soda-lime glass composition with temperature-dependent dynamic viscosity $\eta(T)$, mass density $\rho(T)$, and electrical conductivity $\kappa(T)$ as described in Subsection 6.2.1. All other material properties are considered to be constant. The material properties used in the simulation are given in Table 9.1.

A preheated glass melt is assumed to be continuously fed in the inlet, and continuously drawn out at the outlet at a prescribed constant rate of mass flow. The boosting electrodes are assumed to be supplied with direct electric current (DC). Joule heating, natural Lorentz forces, and gravity are taken into consideration. For the second simulation case, the case with additionally generated Lorentz forces, three additional magnet coils are included as illustrated in Figure 7.14.

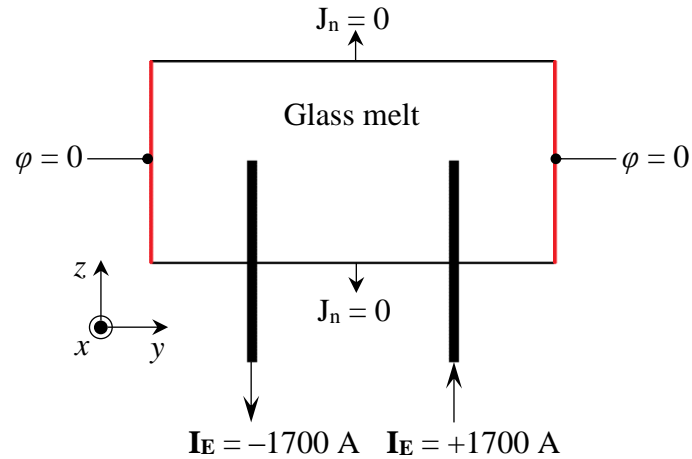


Figure 7.15: Boundary conditions of the electric potential φ and electric current in the middle-section model. J_n is the normal component of electric current density.

The magnetic field of coils generates additional Lorentz forces contrary to the main flow direction of the glass melt, creating an *EMB* effect.

7.4.2 Boundary conditions of the middle-section model

As the tank walls are assumed to have no electric conductivity, electric potential is not calculated in the walls domain. A prescribed electric current of $+1700 \text{ A}$ is assumed to flow through the bottom-surface of one electrode and an electric current of -1700 A through the bottom-surface of the other. Electric current is defined as an electric current density on the bottom-surface of the electrodes using the “Flux” boundary condition for electric potential. As the electric current is assumed to flow from the electrodes to the symmetry sides of the glass melt, as well as from one electrode to the other, the electric potential is fixed at a constant value, i.e. zero, on the symmetry sides, as shown in Figure 7.15. On the inlet, outlet, glass melt surface, and glass melt bottom the normal component of electric current density J_n is fixed at zero. The tangential component of magnetic vector potential is fixed at zero on all outer boundaries. This corresponds to the symmetry boundary condition which means that there is no normal component of the magnetic field. The electric current passed through each coil turn is assumed to be 1700 A , with polarity chosen so as to obtain Lorentz forces against the glass melt flow direction. The coil turns are defined as lying in the xy -plane. The coil current polarity determines the main direction of the coil’s magnetic field: a positive polarity will result a magnetic field in the z -direction, while a negative polarity will result a magnetic field against the z -direction. Accordingly, the coil current should have a positive polarity for the coil between the electrodes and a negative polarity for both side coils, in order to obtain Lorentz forces that run against the main flow direction of the glass melt, cf. Figure 7.20. Furthermore, each coil is assumed to have

20 turns. The coils are not built into the model geometry: their magnetic field is analytically calculated in the glass melt using the Biot-Savart law (Equation (7.14)) for each coil turn.

A glass mass flow rate of 100 T/D is assumed to be entering the inlet surface and leaving the outlet surface. The “No-slip” boundary condition, which means velocity is zero, is used for the glass melt boundaries immediately adjacent to the electrodes and refractory walls. Shear stress is fixed at zero on the glass melt surface and symmetry sides. Gravitational acceleration is set against the z -direction.

The glass melt temperature at the inlet is fixed at a prescribed temperature of 1553.15 K. Heat flux across the glass melt surface and symmetry sides is fixed at zero. This boundary condition results in a temperature distribution approximating to that of simulations taken from the glass industry. Temperature exchange by convection and radiation is assumed at the outer boundaries of the tank walls, where the ambient temperature assumed is 323.15 K. The temperature-dependent material properties are defined using UDF.

7.4.3 Computational grid and numerical solution

As no solution convergence is obtained when automatically generated tetrahedral mesh (ANSYS WORKBENCH-generated) is used to perform the coupled calculations, a well-structured mesh with an adapted resolution at the boundary layers is necessary to obtain a good solution convergence for this strongly coupled problem. For this purpose, the software tool ICEM CFD is used to generate a hexahedral mesh of about 4.57×10^5 cells. The steady-state system behavior is calculated using the “Pressure-Based” solver for laminar flow model. The pressure and velocity are linked by the SIMPLE algorithm. Gradients are computed using the “Green-Gauss Node Based” method using second order solution correction for all variables. The default settings are retained for the under-relaxation factor. The calculations are set to terminate if the residuals are smaller than 1×10^{-6} .

7.4.4 Results from the middle-section model

It is the distribution of the density of the electric current, the magnetic flux, and the Lorenz force within the glass melt that is the main focus of interest. These additionally calculated variables are stored in the memory using user-defined memory (UDM) macros featured by FLUENT. The initial case (before the three magnet coils are added) is here first discussed. Electric current density within the glass melt has the largest intensity in the vicinity of the electrodes, see Figure 7.16. Consequently the largest Joule heat is also generated near the electrodes, so that local thermal convection flow brings the colder bottom glass towards the surface. The generated Joule heat density within the glass melt is calculated from the electric current density

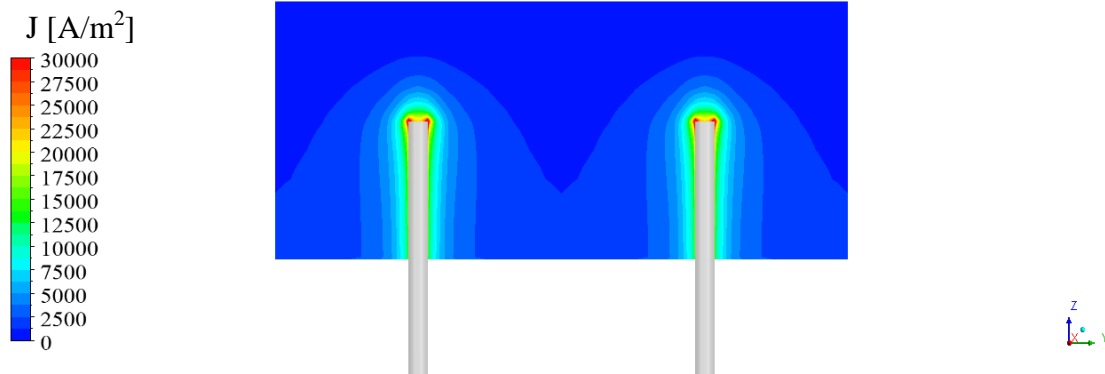


Figure 7.16: The distribution of electric current density magnitudes within the glass melt in a sectional plane across the electrodes, in the initial case (without the additional magnet coils).

using Equation (7.17), and it is set as a source term for temperature field calculation in FLUENT. The gradual decrease in temperature from the surface to the bottom is the main temperature profile within the glass melt, see Figure 7.17 (b). This is the typical temperature distribution in continuous glass-melting tanks. The temperature distribution within the glass melt determines the local values of the glass material properties, i.e. $\eta(T)$, $\rho(T)$, and $\kappa(T)$. Electric current density is the source of magnetic vector potential which is used to calculate the magnetic flux density distribution within the glass melt. The largest magnetic flux density arises in the vicinity of the electrodes, being the eigenfield surrounding the electrodes, see Figure 7.18 (a). The eigenfield is caused by the high electric current densities within the electrodes themselves. Away from the electrodes, it drops steeply.

Now, in the second case with the additional three coils, the magnetic flux density induced by electric current density is added to that generated by the coils, resulting in the total magnetic flux density distribution within the glass melt, see Figure 7.18 (b). Lorentz force density within the glass melt is the cross product of electric current and magnetic flux densities (Equation (7.16)), and it is set as a source term for flow calculation in FLUENT. Figure 7.19 shows a comparison of the Lorentz force density distributions within the glass melt in both considered cases. In the initial case (Figure 7.19 (a)), natural Lorentz forces arise around the electrodes, causing some extra lifting of the glass melt in the tiny area surrounding the electrode. In the second case, after the three magnet coils are added (Figure 7.19 (b)), an additional Lorentz force density is generated between the electrodes and also between the electrodes and the symmetry sides. The additionally generated Lorentz force density has the largest intensity at the bottom and decreases towards the surface, as is to be expected from the causative additional magnetic flux density profile generated by the coils. Figure 7.20 (c) shows how the additionally generated Lorentz forces are orientated against the main flow direction in the tank to retard the glass melt

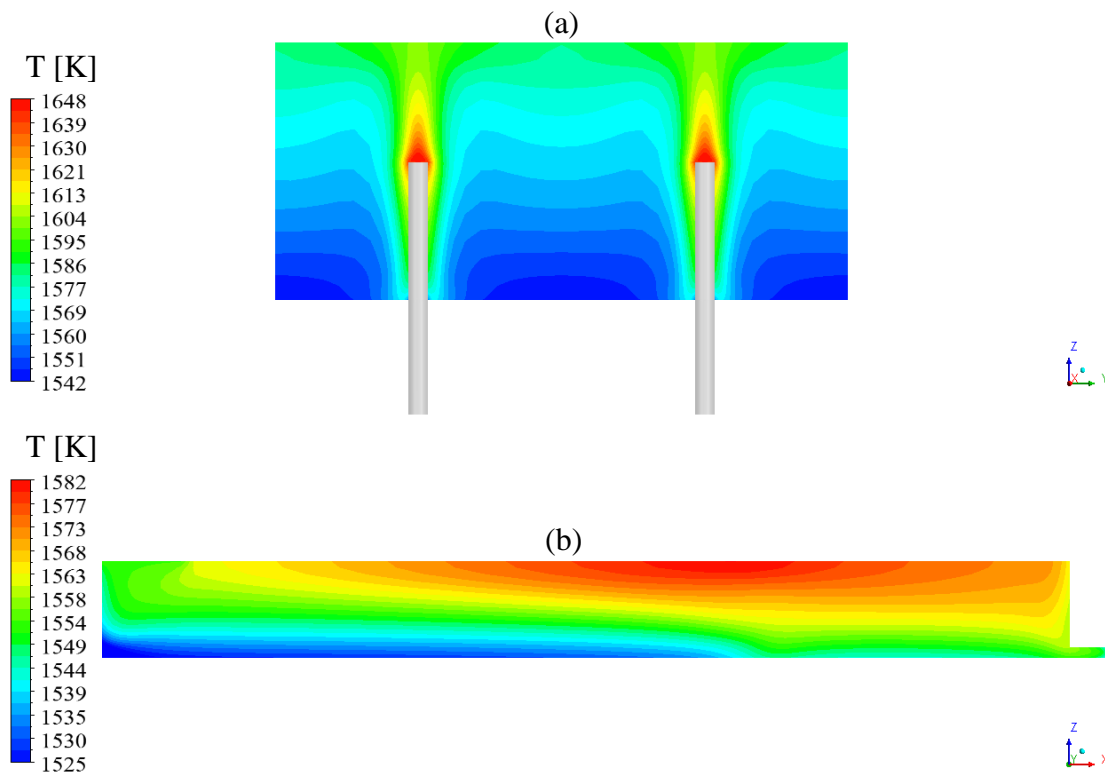


Figure 7.17: The temperature distribution within the glass melt in the initial case (without the additional magnet coils) (a) in a sectional plane across the electrodes and (b) in a longitudinal sectional plane along the centerline between the electrodes.

flow, thus creating an electromagnetic wall between the electrodes and also between the electrodes and the symmetry sides. The influence of the additional Lorentz forces on the glass melt flow is visualized by “streamlines” which are the paths travelled by glass melt particles. In Figure 7.21, the glass melt flow in both considered cases is compared using streamlines of 90 glass melt particles released from the inlet and evenly distributed. In the initial case (Figure 7.21 (a)), the glass melt near the electrodes is driven to the surface by buoyancy. Two recirculating flows are formed in front of and behind the electrodes, which is the typical flow pattern in continuous glass-melting tanks. In the second case with the additional Lorentz forces, the obvious additional vortices that appear in Figure 7.21 (b), in front of and behind the electrodes, indicate that the additional Lorentz forces increase the length of the streamlines. It thus becomes obvious that the additional Lorentz forces intensify the glass melt recirculation within the tank. This desired flow control influence increases the residence time of the glass melt within the tank.

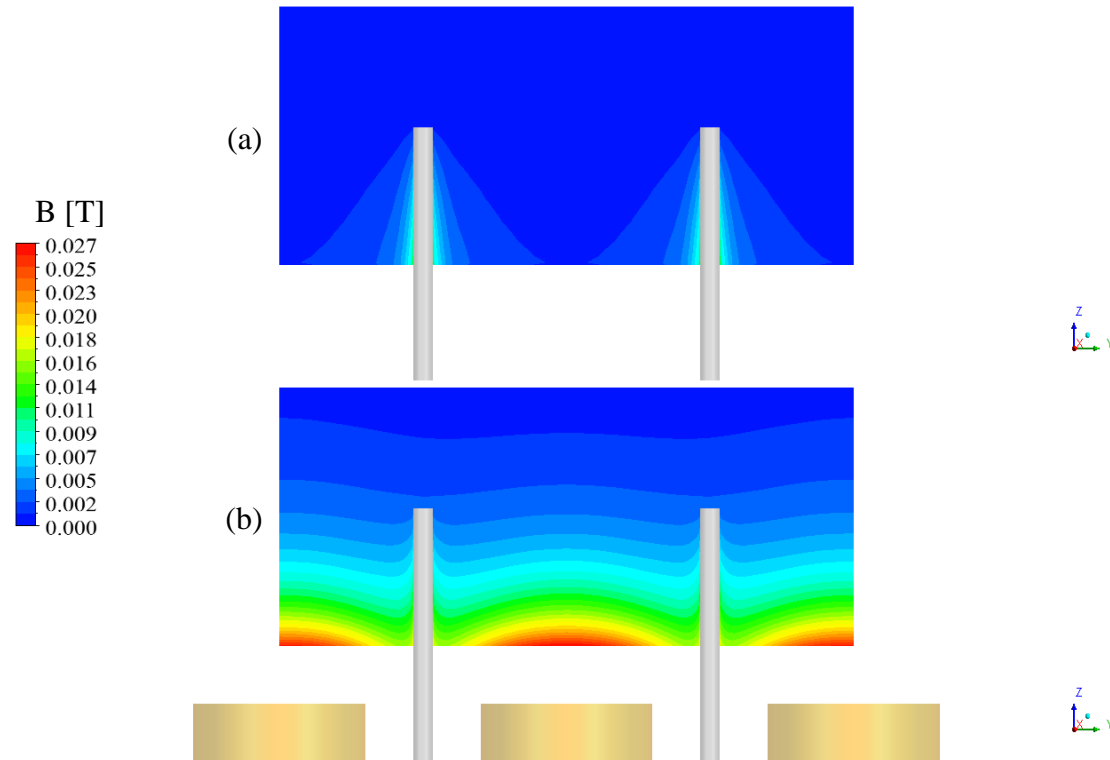


Figure 7.18: The distribution of magnetic flux density magnitudes within the glass melt in a sectional plane across the electrodes (a) in the initial case (without the additional magnet coils) and (b) in the case with three additional magnet coils.

Conclusions drawn from middle-section model

Implementing electromagnetic field calculation in FLUENT offers a reliable simulation tool for the coupled three-dimensional problem of electrodynamics, thermodynamics, and hydrodynamics which is under consideration. Obtaining a solution convergence for a problem with such a strong coupling necessitates a well-structured computational grid with an adapted resolution at the boundary layers. In order to reduce the computational time and efforts a relatively coarse mesh is used for the calculations. Although the middle-section model is not appropriate for comprehensive investigation of the real glass-melting tank in which glass melt flows in the whole tank volume, and for which all six boosting electrodes must be considered, the simulated model and its boundary conditions are a valuable test-example. They are not a simulation of the real-life tank, but serve the model developing process. In this context, it is shown that adding Lorentz forces orientated against the main flow direction between the electrodes does result in the desired flow control effect. Again, it is only a general view of the flow conditions that is obtained by calculating these from streamlines of 90 particles. The next step will be to model the complete glass-melting tank considering the six boosting electrodes and their distributed three-phase energizing scheme. This requires AC system calculation, the subject of the following section.

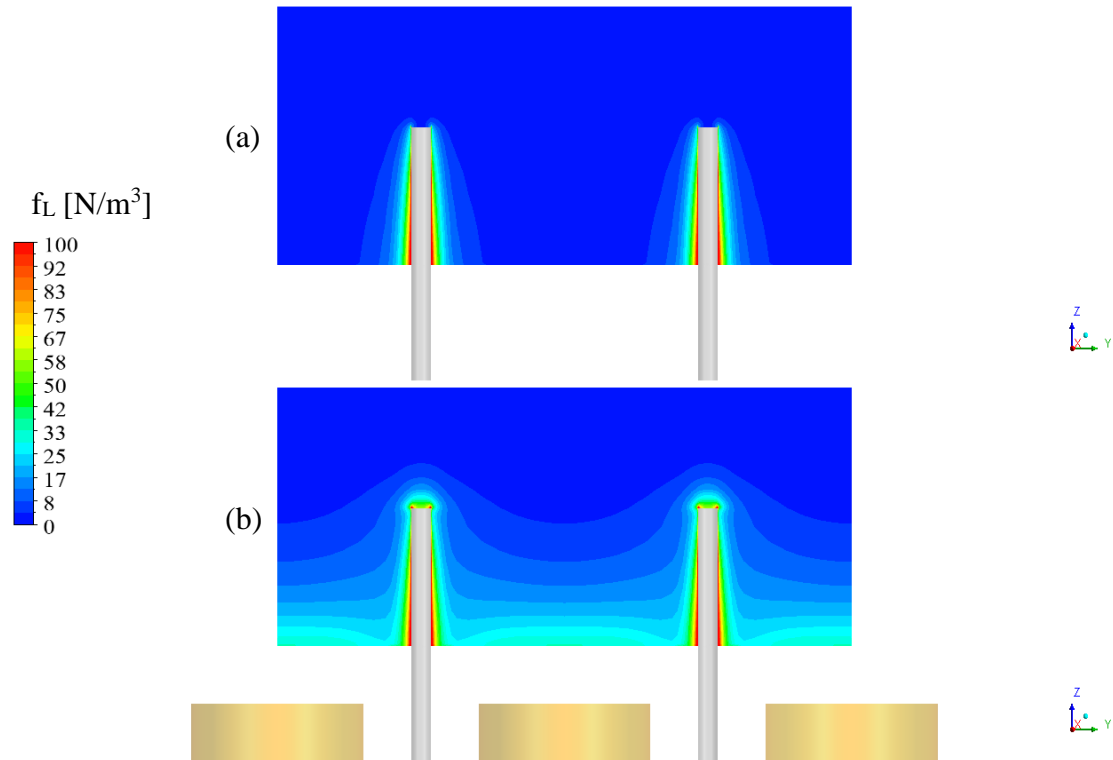


Figure 7.19: The distribution of Lorentz force density magnitudes within the glass melt in a sectional plane across the electrodes (a) in the initial case (without the additional magnet coils) and (b) in the case with three additional magnet coils.

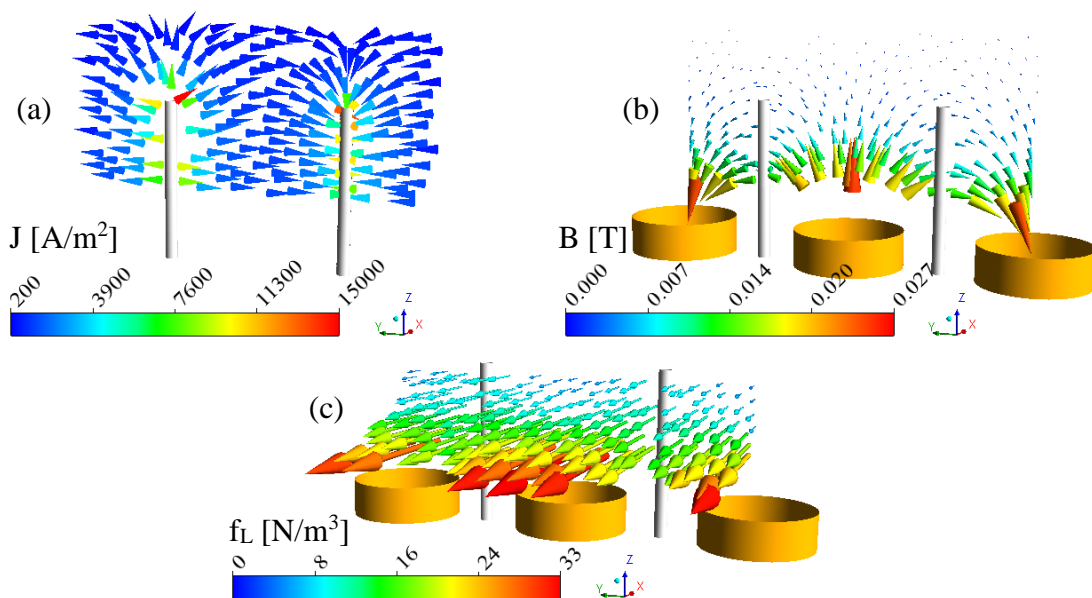


Figure 7.20: The distribution (a) of the electric current density vectors, (b) of the magnetic flux density vectors generated by the additional coils, and (c) of the additional Lorentz force density vectors within the glass melt, all presented in a sectional plane across the electrodes.

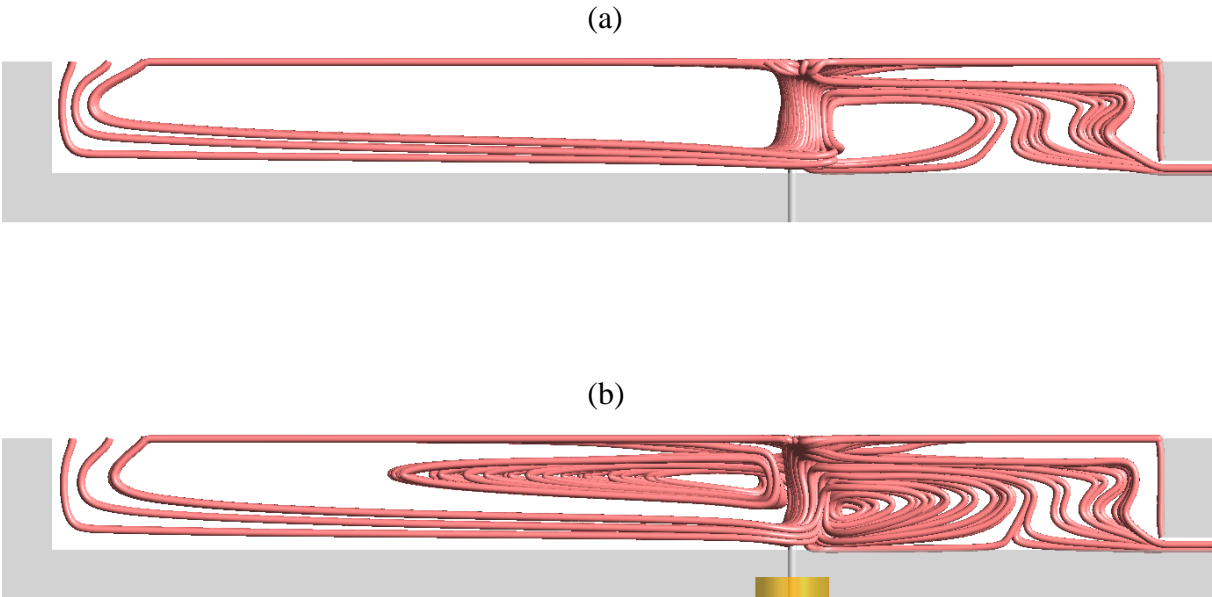


Figure 7.21: Side view of 90 streamlines released from the inlet (a) in the initial case (without the additional Lorentz forces) and (b) in the case with the additional Lorentz forces.

7.5 Calculating a steady-state AC system with FLUENT

Problems that include sinusoidal variation, i.e. AC system, are mathematically described using complex number expression, which means that all electric and magnetic quantities are decomposed into real and imaginary parts [122,123]. Accordingly, the approach presented in Section 7.2 has to be considered for real and imaginary parts. That way, the appropriate distributed three-phase AC system used to energize the electrodes can be defined by defining both real and imaginary components of electric potential at the electrodes.

Electric current density in AC system is calculated by

$$\underline{\mathbf{J}} = -\kappa(\nabla\varphi + j\omega\underline{\mathbf{A}}). \quad (7.21)$$

The low electrical conductivity of glass melt and the low frequency, i.e. 50 Hz, used for the direct electric heating in the glass-melting tank mean that the component $-\kappa(j\omega\underline{\mathbf{A}})$ is negligible, i.e. eddy currents within the glass melt are neglected [107].

Thus, as described in Subsection 6.2.2 (see Equations (6.5) to (6.8)), the transport equation of complex electric potential (Equation (6.8)) is derived, enabling the transport equations of complex electric potential components φ_{Re} and φ_{Im} to be found:

$$\nabla \cdot (\kappa \nabla \varphi_{\text{Re}}) = 0. \quad (7.22)$$

$$\nabla \cdot (\kappa \nabla \varphi_{\text{Im}}) = 0. \quad (7.23)$$

Also, following the definition in Subsection 6.2.2 (see Equations (6.10) to (6.13)), applying the vector equality $\nabla \times (\nabla \times \underline{\mathbf{A}}) = \nabla(\nabla \cdot \underline{\mathbf{A}}) - \nabla^2 \underline{\mathbf{A}}$ to the left-hand side of Equation (6.13) gives [117]

$$\nabla(\nabla \cdot \underline{\mathbf{A}}) - \nabla^2 \underline{\mathbf{A}} = \mu_0 \underline{\mathbf{J}}. \quad (7.24)$$

Furthermore, Coulomb gauge

$$\nabla \cdot \underline{\mathbf{A}} = 0. \quad (7.25)$$

reduces Equation (7.24) to the Poisson equation:

$$\nabla^2 \underline{\mathbf{A}} = -\mu_0 \underline{\mathbf{J}}. \quad (7.26)$$

From Equations (7.26) and (6.5), the transport equations of complex magnetic vector potential components $A_{x\text{Re}}$, $A_{x\text{Im}}$, $A_{y\text{Re}}$, $A_{y\text{Im}}$, $A_{z\text{Re}}$, and $A_{z\text{Im}}$ are, in turn, found:

$$\nabla^2 A_{x\text{Re}} = \mu_0 \kappa \frac{\partial \varphi_{\text{Re}}}{\partial x}. \quad (7.27)$$

$$\nabla^2 A_{x\text{Im}} = \mu_0 \kappa \frac{\partial \varphi_{\text{Im}}}{\partial x}. \quad (7.28)$$

$$\nabla^2 A_{y\text{Re}} = \mu_0 \kappa \frac{\partial \varphi_{\text{Re}}}{\partial y}. \quad (7.29)$$

$$\nabla^2 A_{y\text{Im}} = \mu_0 \kappa \frac{\partial \varphi_{\text{Im}}}{\partial y}. \quad (7.30)$$

$$\nabla^2 A_{z\text{Re}} = \mu_0 \kappa \frac{\partial \varphi_{\text{Re}}}{\partial z}. \quad (7.31)$$

$$\nabla^2 A_{z\text{Im}} = \mu_0 \kappa \frac{\partial \varphi_{\text{Im}}}{\partial z}. \quad (7.32)$$

Index: k	Scalar: ϕ_k	Diffusivity: Γ_k	Source: S_{ϕ_k}
1	φ_{Re}	κ	0
2	φ_{Im}	κ	0
3	$A_{x\text{Re}}$	1	$-\mu_0 \kappa \frac{\partial \varphi_{\text{Re}}}{\partial x}$
4	$A_{x\text{Im}}$	1	$-\mu_0 \kappa \frac{\partial \varphi_{\text{Im}}}{\partial x}$
5	$A_{y\text{Re}}$	1	$-\mu_0 \kappa \frac{\partial \varphi_{\text{Re}}}{\partial y}$
6	$A_{y\text{Im}}$	1	$-\mu_0 \kappa \frac{\partial \varphi_{\text{Im}}}{\partial y}$
7	$A_{z\text{Re}}$	1	$-\mu_0 \kappa \frac{\partial \varphi_{\text{Re}}}{\partial z}$
8	$A_{z\text{Im}}$	1	$-\mu_0 \kappa \frac{\partial \varphi_{\text{Im}}}{\partial z}$

Table 7.2: Parameter settings for the user-defined scalar (UDS) equations required to calculate complex electric potential components φ_{Re} and φ_{Im} and complex magnetic vector potential components $A_{x\text{Re}}$, $A_{x\text{Im}}$, $A_{y\text{Re}}$, $A_{y\text{Im}}$, $A_{z\text{Re}}$, and $A_{z\text{Im}}$.

Equations (7.22), (7.23), (7.27), (7.28), (7.29), (7.30), (7.31), and (7.32) are solved using eight UDS equations, as defined in Table 7.2. Both the unsteady term and the convective term in Equation (7.1) are set to zero.

After that, the calculated values of φ_{Re} , φ_{Im} , A_{xRe} , A_{xIm} , A_{yRe} , A_{yIm} , A_{zRe} , and A_{zIm} are used to calculate electric current density $\underline{\mathbf{J}}$ and its induced magnetic flux density $\underline{\mathbf{B}}$ using Equations (6.5) and (6.12) respectively. This is performed using UDF which can be dynamically loaded with the FLUENT solver.

Also by means of UDF, the additional complex magnetic flux density generated by the coils $\underline{\mathbf{B}}_C$ is calculated using the Biot-Savart law for each turn of each coil, i.e. Equation (6.14), which provides an analytical solution for a domain with constant magnetic permeability.

The total complex magnetic flux density is then defined as

$$\underline{\mathbf{B}}_{\text{Total}} = \underline{\mathbf{B}} + \underline{\mathbf{B}}_C. \quad (7.33)$$

Lorentz force density \mathbf{f}_L (time averaged) is calculated using UDF for Equation (6.16). Furthermore, \mathbf{f}_L is set as an additional parameter for source term S_{ϕ_k} in the momentum equation which is solved by FLUENT to calculate the flow field.

Joule heat density p_v is calculated using UDF for Equation (6.9) and set as an additional parameter for source term S_{ϕ_k} in the energy equation which is solved by FLUENT to calculate the temperature field.

8 Numerical grid, solution, and accuracy

This chapter gives details of the computational grid on which the numerical solution is created. There follows a note on the numerical solution for the governing equations. Finally, various studies are carried out to verify the numerical accuracy.

8.1 Computational grid

To obtain a numerical solution of partial differential equations, the computational domain requires division into geometrical elements (cells). The resultant cell structure forms the computational grid (mesh), which can be also viewed as points (nodes) connected by straight lines. Mesh is one of the most important considerations for numerical simulations as it is the structure on which the numerical solution is built [124]. The structure is basically of triangles or quadrilaterals in two-dimensions, and tetrahedra or hexahedra in three-dimensions. As hexahedral cells provide higher solution accuracy than tetrahedral cells, they tend to be more numerically stable. Also, when a hexahedral mesh is compared with a tetrahedral one with the same number of nodes, the number of elements is several times lower. Consequently, hexahedral meshes offer reduced numerical error and less computational time than tetrahedral ones. On the other hand, for volume mesh generation, tetrahedral mesh is more easily generated even for models with complex geometries. Tetrahedral mesh generators also provide more automatic generation process with the ability to add mesh controls to improve the accuracy in critical regions. In contrast, hexahedral mesh generation is more difficult to perform and automate, and takes several orders of magnitude longer than tetrahedral mesh generation [125].

The mesh quality strongly influences the simulation accuracy. In general, fluid dynamics simulations require very high-quality meshes in both cell shape and smoothness of size variation. For the strongly coupled problem of hydrodynamics, thermodynamics, and electrostatics considered in this work, the test simulations have shown that no solution convergence can be obtained using an automatically generated unstructured mesh, i.e. tetrahedral mesh. The use of a structured mesh, i.e. hexahedral mesh, thus becomes a basic prerequisite for the numerical simulations. Both geometric configuration and physical solution must be considered in designing the mesh structure. The mesh interior should vary smoothly between the boundaries. As distribution within the mesh is critical for numerical solution, it should capture the physical field features. The physical field should be properly resolved in critical regions to minimize the variation in the field variables from cell to cell. In general, no field passage should be represented by fewer than five cells and the change in cell size should be gradual. For high-quality meshes, highly skewed cells and cells with high aspect ratios should be avoided where possible, as such badly shaped cells tend to decrease the numerical stability. Skewness represents the



Figure 8.1: Plane view of the top side of the block-structured hexahedral mesh topology, generated using the commercial software ICEM CFD, for the tank simulation. The related geometry is depicted in Figure 6.1.

deviation from equiangular shape, and cell aspect ratio represents the ratio of the longest cell edge to the shortest cell edge [116].

In the present work, the commercial software ICEM CFD is used to generate a well-structured hexahedral mesh topology which successfully maps the system features. The considered geometry can be designed using the CAD-functions of ICEM CFD or it can be easily imported from another source, e.g. ANSYS WORKBENCH. For the mesh generation, the block-structured technique, in which the domain is decomposed into a number of topologically simpler domains, is here adopted. Thus, each domain can be meshed independently and relatively simply. The intended mesh topology requires determination of the number of blocks and how they should be arranged. It is then necessary to set the parameters of each block edge in terms of number and spacing of nodes. This task is time consuming: one week for even this simple tank geometry that is depicted in Figure 6.1. It can take several weeks for more complex geometries. Figure 8.1 presents a plane view of the high-quality hexahedral mesh topology generated with ICEM CFD for the tank simulation. The figure shows the regular rectangular mesh cells and how the mesh

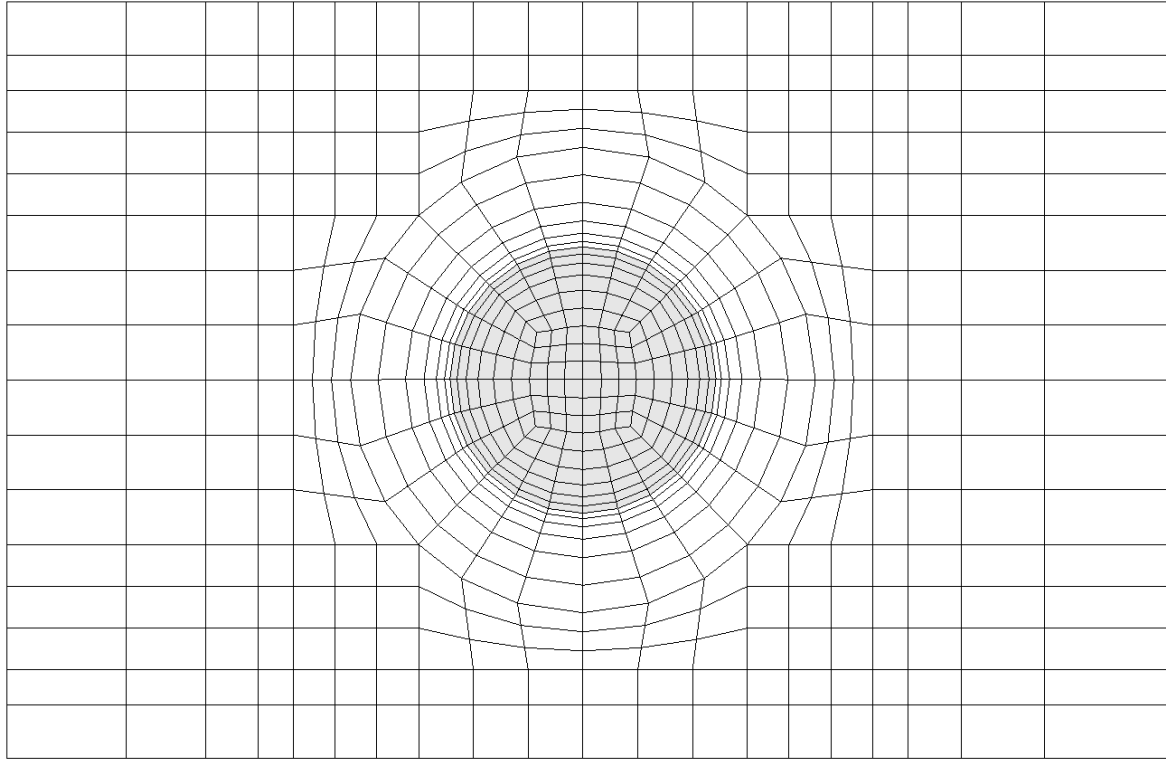


Figure 8.2: Plane view of the body-fitted O-grid mesh topology inside and around the electrode, generated using the commercial software ICEM CFD, to capture the circular shape of the electrode cross-section. The grey part represents the electrode domain.

resolution is adapted between the boundaries and increased in the critical region near the electrodes. The O-grid technique has been employed to generate a body-fitted mesh inside and around the electrodes. Individual O-grid-blocks have been allocated to each cylindrical electrode and to each surrounding area. The body-fitted mesh captures the circular geometry of the electrode cross-section, as shown in Figure 8.2. In CFD, a body-fitted meshing approach supports accurate resolution of the flow at the boundaries, which is especially necessary for shear layers along a solid body. However, this involves more complexity in the meshing tool [126]. The number of cells is defined by a mesh-convergence study, given in Subsection 8.3.1.

8.2 Numerical solution

When the solution domain has been divided in this way into a number of smaller cells, the system of governing equations is solved for each volume cell using FLUENT, which is based on FVM as the means of discretizing the governing equations. First, the solution domain is discretized into control volumes using the mesh. Then, the governing differential equations are integrated on the individual control volumes so that they can be approximated by algebraic equations that are capable of numerical solution. The system of algebraic equations is then

solved to produce discrete values that approximate the solution of the partial differential system. The solution loop is carried out iteratively to converge the numerical solution. A steady-state system behavior is calculated with FLUENT using the Pressure-Based solver which was developed for low-speed incompressible flows. The laminar flow model is specified in the present case. Pressure and velocity are linked by the SIMPLE algorithm, which is suitable for complicated problems. Gradients are computed using the Green-Gauss Node Based method, as this method will give higher accuracy than the cell based one. For all variables, second order solution correction is the option chosen, to provide the highest accuracy of the convergence. Less convergence stability is, however, available with this option. To achieve stable convergence behavior, the under-relaxation factors of density, body force, momentum, energy and all UDS's are reduced from their default values to 0.7, 0.9, 0.5, 0.9, and 0.9 respectively. Under-relaxation of equations is used to control the update of calculated variables at each iteration. Reducing under-relaxation factors is usually a necessity in strongly coupled problems where unstable convergence behavior can be observed. The technique damps strong parameter variations, giving the solution algorithm a certain number of iterations to adjust to the new parameters. Nevertheless, convergence behavior of a completely stable kind is still not achievable. To overcome this problem, the initial conditions are built up gradually over two hundred iterations. These are performed using cell based gradient computation and first order solution correction, providing the greater convergence stability which is desirable regardless of the lower accuracy. It is a feature of this initial calculation that an initial temperature must be set or there will be calculation disturbance. The initial guess gained over the two hundred iterations is then used as a start solution for the simulation. The convergence criterion for terminating the calculation is specified by a study as described in Subsection 8.3.2. After the steady-state simulation has been calculated, the velocity vectors will be saved in each grid cell. There will thus be a mapped velocity in the solution domain. *RTD* can then be calculated using the particle tracing technique in CFD. This technique uses an infinitesimal volume of material called a "particle" to follow the velocity vectors. In this way, particle trajectory and particle residence time are calculated. The particle trajectory (also called a streamline) is the curve that is tangential to the velocity vectors. The particle tracing process is available in FLUENT within the "Discrete Phase Model".

8.3 Verification and accuracy

Solution verification is the process of evaluating the numerical accuracy of the obtained solution. As such, it deals with solution accuracy and should not be confused with the validation term which addresses the modeling accuracy. Both processes are, of course, essential for every numerical simulation as they are the basis for quantifying the accuracy of the results and the reliability of the calculation [118,119]. In this section, the focus is on the verification.

8.3.1 Mesh-convergence study

Section 8.1 has discussed the quality and topology of the generated mesh which will guarantee the highest calculation stability and map the system features very well. However, the cell size which is desirable to resolve the flow features has still to be determined on the basis of numerical accuracy. Refining the mesh will result in a higher solution accuracy but will exact the price of higher computational time. Larger meshes will, indeed, increase the numerical accuracy but the CPU and memory requirements for computation of the solution will increase accordingly. A mesh-convergence study is now given, to determine the most efficient mesh resolution at best compromise between accuracy and computational time. The systematic mesh-convergence study has to quantify the numerical uncertainty [127]. During the study, the mesh resolution is increased until the solution changes only within a reasonable tolerance. The mesh-convergence study has been carried out for the four different mesh resolutions that are given in Table 8.1. It considers the ordinary tank operation case, i.e. without *EMB*, referred to as the baseline-case in Section 9.1. The influence of the mesh resolution on the kinetic energy E_k of the glass melt is investigated as a global value, calculated in FLUENT using

$$E_k = \frac{1}{2} \int_{V_{Glass}} \rho |\mathbf{u}|^2 dV . \quad (8.1)$$

Figure 8.3 demonstrates how the kinetic energy E_k of the glass melt converges rapidly as the number of cells within the glass melt domain increases. Furthermore, with the mesh refinement more than that of Mesh-3, E_k tends to have a very small change (less than 3%).

Mesh	Min. Δx within the glass melt	Max. Δx within the glass melt	Number of cells within the glass melt	Total number of cells
Mesh-1	1.5 mm	79.4 mm	880 710	1 471 080
Mesh-2	1.4 mm	67.7 mm	1 605 342	2 517 760
Mesh-3	1.4 mm	39.7 mm	2 945 640	4 509 960
Mesh-4	0.75 mm	29.9 mm	6 477 390	10 130 400

Table 8.1: Mesh resolutions used in the mesh-convergence study, where Min. Δx and Max. Δx are respectively the minimum and maximum lengths of cell edge. Min. Δx exists at the boundaries of the domain.

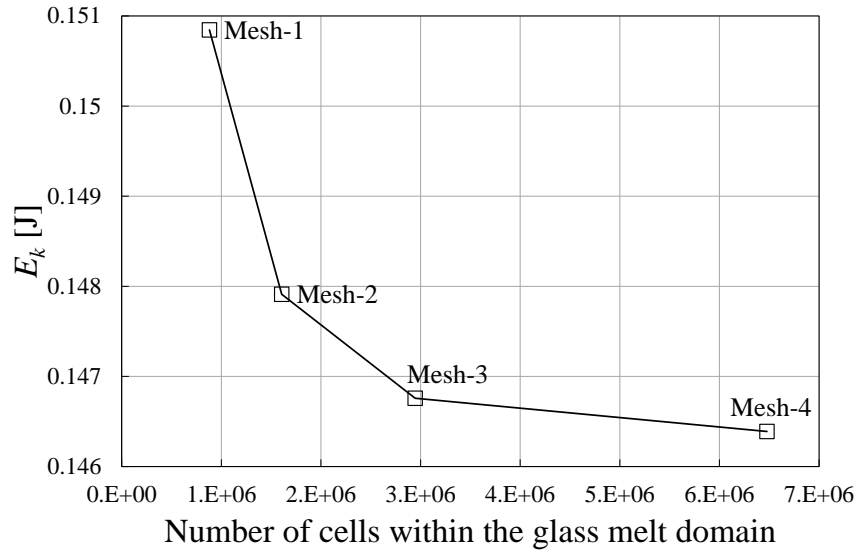


Figure 8.3: Mesh-convergence study on the basis of the kinetic energy E_k of the glass melt for the different mesh resolutions that are given in Table 8.1. The calculations were performed for the baseline-case of tank operation defined in Section 9.1, i.e. without *EMB*.

As the ultimate simulation goal is to evaluate the *MRT* of the glass melt in the tank, it is also beneficial to study the influence of the mesh resolution on *MRT*. The importance of mesh resolution to determine the numerical accuracy of *MRT* calculation is emphasized in [72]. As shown in Figure 8.4, the mesh refinement leads to *MRT* variation towards an asymptotic value (the change is less than 2%) at mesh refinement more than that of Mesh-3. The mesh-convergence study presented reveals that sufficient numerical accuracy can be attained using Mesh-3 for performing the calculations. As is shown in Table 8.1, the reduction of cell size leads to an explosive increase in the total number of cells and consequently in greatly extended computational time. The simulations carried out in the present work used 8 CPU cores (each 2.67 GHz) on the “Massive Parallel Computer Cluster” at the computer center of “Technische Universität Ilmenau” [128]. The number of CPU cores to be used for the calculation is constrained by the number of ANSYS FLUENT licences available. The simulation using Mesh-3 requires about one week of computational time, which extends to one month if Mesh-4 is used. The computer memory capacity needed for Mesh-3 is about 15 GB, while it is about 30 GB for Mesh-4. Consideration of the substantial amount of computational time and resources required for solving the three-dimensional coupled problem led to the choice of Mesh-3 for performing the simulations, as the best compromise between numerical accuracy and computational time.

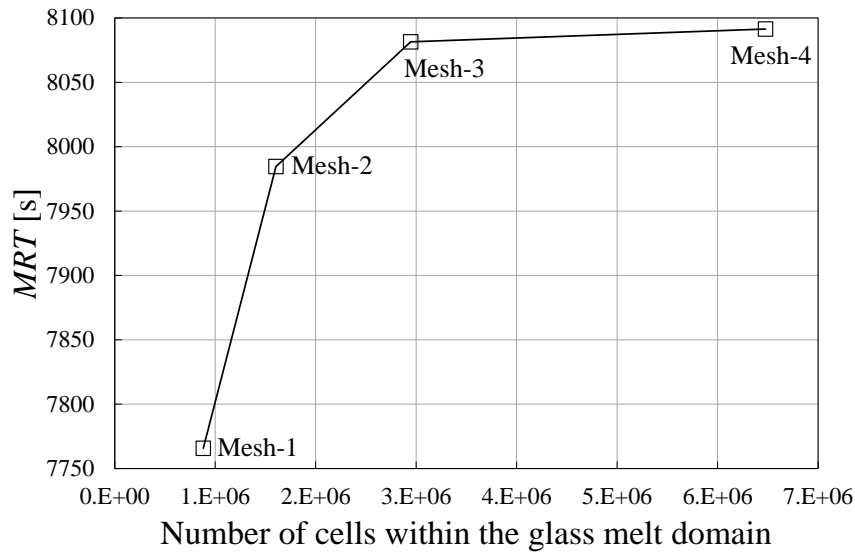


Figure 8.4: Mesh-convergence study on the basis of the *MRT* of the glass melt for the different mesh resolutions that are given in Table 8.1. The calculations were performed for the baseline-case of tank operation defined in Section 9.1, i.e. without *EMB*.

8.3.2 Residual evaluation study

In FVM, the term residual refers to the discretization error that results from incomplete iterative solution. In other words, it represents the amount of numerical error left within the approximated solution as it approaches the exact solution. Iterative residuals of the solution variables decay to some small values as the iterative solution converges. FVM demands residual evaluation to determine the convergence criterion for terminating the calculation. This is done on the basis of solution accuracy. When the solution does not significantly change as residual levels reduce, the obtained residuals are considered to be sufficient and the calculation can be terminated. To determine the convergence criterion, the maximum solution residual is studied on the basis of the kinetic energy E_k of the glass melt, see Figure 8.5. The study shows rapid convergence of the kinetic energy E_k of the glass melt, revealing no significant change (less than 0.0015%) at a maximum solution residual less than 1×10^{-7} . As *MRT* of the glass melt in the tank is the ultimate focus of the simulation, it is also taken as a basis for the determination of the convergence criterion. In Figure 8.6, it is demonstrated that the variation in *MRT* of the glass melt develops until there is hardly any significant change (less than 0.00015%) at a maximum solution residual less than 1×10^{-7} . Accordingly, the convergence criterion for the simulations is set so that the calculations terminate if the maximum residual is less than 1×10^{-7} . The numerical simulation will be iteratively calculated until this criterion is satisfied.

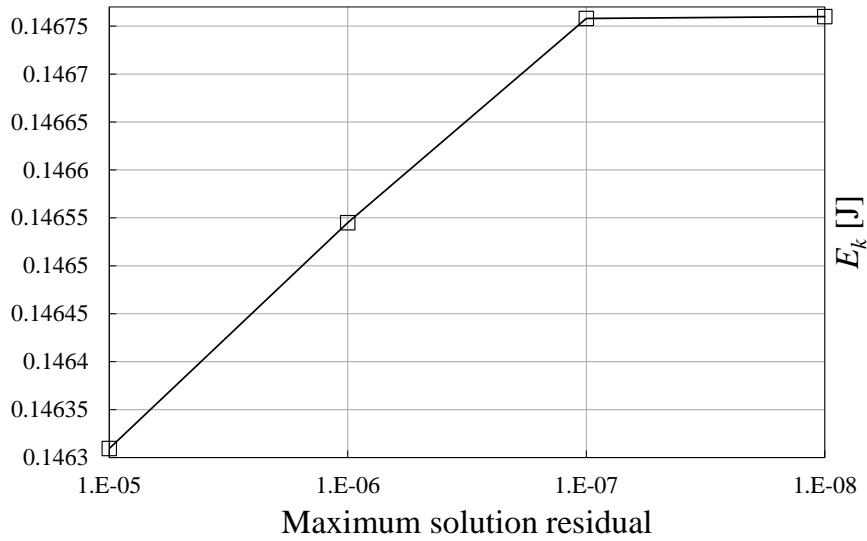


Figure 8.5: Residual evaluation study on the basis of the kinetic energy E_k of the glass melt (at Mesh-3). The calculation was performed for the baseline-case of tank operation defined in Section 9.1, i.e. without *EMB*.

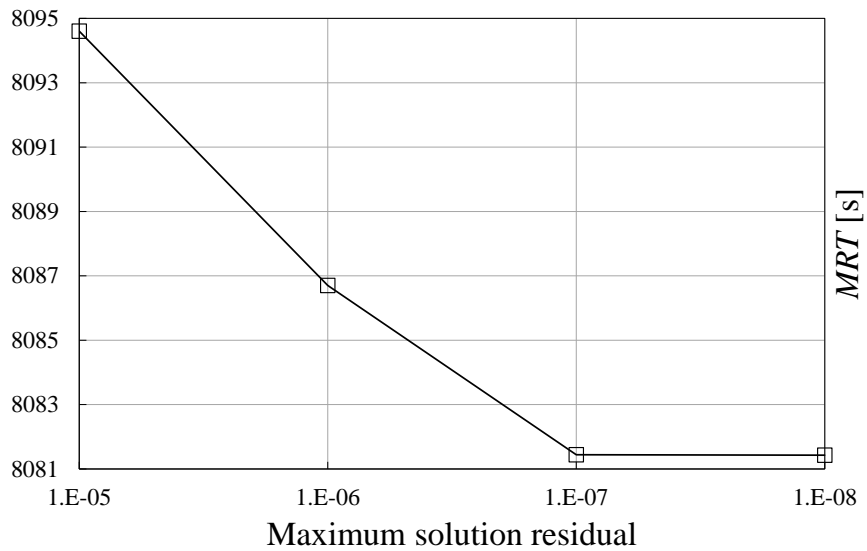


Figure 8.6: Residual evaluation study on the basis of the *MRT* of the glass melt (at Mesh-3). The calculation was performed for the baseline-case of tank operation defined in Section 9.1, i.e. without *EMB*.

9 Implementation and results

This chapter contains the simulations of the real continuous glass-melting tank, undertaken as an investigation of the dynamic system behavior under two sets of conditions, i.e. with and without *EMB*. The boundary conditions are defined and the circuit arrangement for operating the *EMB* system is adapted. Suitable parameter studies are carried out to obtain the optimum process conditions. The simulation results are discussed and comparisons are made. Finally, the structural steel of the tank construction is taken into account for the case of installation of additional magnet coils.

9.1 The baseline-case

As a starting point, or baseline-case, for comparisons, the continuous glass-melting tank is taken in its normal operating state. In this normal state, electric boosting (*EB*) is applied, without *EMB*. The tank model is given in Chapter 6.

9.1.1 Boundary conditions

The boundary conditions for the tank simulation with FLUENT are defined as follows. On the tank-inlet, the “mass-flow-inlet” boundary condition is given for defining a glass mass flow rate $\dot{m} = 1.157407 \text{ kg/s}$ ($= 100 \text{ T/D}$) at a prescribed temperature. On the tank-outlet, the “out-flow” boundary condition is given. This boundary condition is usually used where the details of flow parameters are not known prior to solving the problem. The “No-slip” boundary condition, which means velocity is zero, is given on the glass melt boundaries immediately adjacent

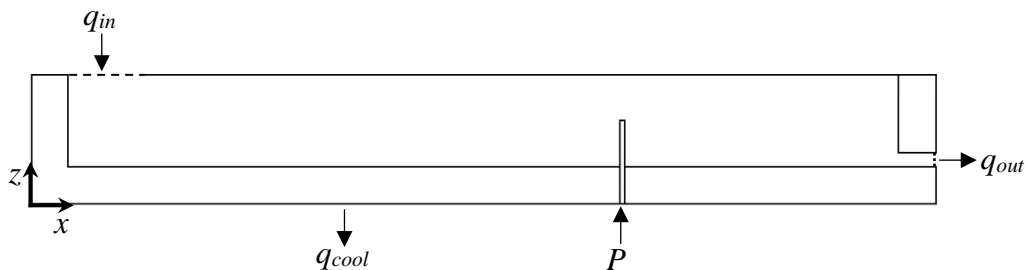


Figure 9.1: Power balance of the glass-melting tank, where q_{in} is the input heat transfer rate introduced by combustion for heating the batch mass, q_{out} is the output heat transfer rate through the molten glass mass that is leaving the tank, q_{cool} is the heat transfer rate from the tank walls to the surroundings (wall losses), and P is the electric power introduced by *EB* system: $q_{in} + P = q_{out} + q_{cool}$.

Property	Soda-lime glass	Molybdenum electrodes	Tank walls
Mass density ρ in kg/m ³	$\rho(T) = -0.1524T + 2550$	10220	6070
Specific heat capacity c_p in J/kgK	1235	250	450
Effective thermal conductivity λ_{eff} in W/mK	100	138	2.5
Dynamic viscosity η in Pa·s	$\log \eta(T) = -5.5235 + \frac{10968}{T}$	-	-
Electrical conductivity κ in S/m	$\log \kappa(T) = 4.044 - \frac{3932.5}{T}$	2.5×10^6	-

Table 9.1: Table of the material properties used in the simulation of the glass-melting tank.

to the electrodes and to the inner boundaries of the tank walls. Shear stress is fixed at zero on the glass melt surface. In the baseline-case, the glass melt throughput flow from the tank-inlet to the tank-outlet is influenced by thermal convection, especially near the electrodes where Joule heat is introduced. Furthermore, natural Lorentz forces have a lifting influence on the glass melt flow in the tiny area surrounding the electrodes.

The glass melt temperature at the tank-inlet is fixed at the prescribed temperature $T_{in} = 1609.15$ K. This inlet-temperature is determined by the power balance (see Figure 9.1), taking into account the typical temperature $T_{out} = 1623.15$ K at which the glass melt leaves the tank in reality. As combustion is not included in the model, heat flux across the glass melt surface is fixed at zero. The temperature distribution resulting from this boundary condition is approximately that of simulations taken from the glass industry. Temperature exchange by convection and radiation is assumed at the outer boundaries of the tank walls. The ambient temperature is assumed to be 323.15 K. The temperature-dependent material properties are defined using UDF. The material properties used are given in Table 9.1.

As the tank walls are assumed to have no electrical conductivity, electric potential is not calculated in the walls domain. For the *EB* system, *effective* electric voltage is given on the bottom-surface of the electrodes.

Electrode	Electrical phase	Magnitude of effective electric potential $ \underline{\varphi} $	Real component of effective electric potential φ_{Re}	Imaginary component of effective electric potential φ_{Im}
E ₁	– R	57 V	57 cos(180°) V	57 sin(180°) V
E ₂	+ T	57 V	57 cos(120°) V	57 sin(120°) V
E ₃	– S	57 V	57 cos(60°) V	57 sin(60°) V
E ₄	+ R	57 V	57 cos(0°) V	57 sin(0°) V
E ₅	– T	57 V	57 cos(– 60°) V	57 sin(– 60°) V
E ₆	+ S	57 V	57 cos(– 120°) V	57 sin(– 120°) V

Table 9.2: Boundary conditions for the boosting electrodes to simulate the distributed three-phase energizing scheme used for operating the *EB* system in the glass-melting tank.

The voltage value is so determined as to result in the typical amount of electric power $P = 700$ kW introduced in the real industrial tank. The electric power P is calculated in FLUENT by the integration of Joule heat density over the glass melt and electrodes volume:

$$P = \int_V \frac{1}{\kappa} |\underline{\mathbf{J}}|^2 dV \quad (9.1)$$

The real and imaginary components of the effective electric voltage are fixed on the bottom-surface of the electrodes as defined in Table 9.2. φ_{Re} and φ_{Im} are set using the “Value” boundary condition in FLUENT. The distributed three-phase energizing scheme of *EB* in the real industrial glass-melting tank is thus simulated (cf. Figure 3.3). The normal component of electric current density is fixed at zero on the tank-inlet, the tank-outlet, the glass melt surface, the interface between the glass melt and tank walls, and the interface between the electrodes and tank walls. The normal component of electric current density is set to be continuous across the interface between the electrodes and glass melt using natural boundary condition. For magnetic field, natural boundary condition is assumed on all interfaces between objects, which means that the normal component of the magnetic field is continuous across the interface boundaries. Thus, the tank walls domain constitutes an extension region for magnetic field calculation. Furthermore, the tangential component of magnetic vector potential is fixed at zero on all outer boundaries. This corresponds to symmetry boundary conditions whereby the magnetic field has no normal component at the outer boundaries and, thus, does not cross them.

RTD in the glass-melting tank is calculated by performing particle tracing of different massless particles released from the tank-inlet and leaving at the tank-outlet. A maximum number of 20 000 particles is sufficient for the highest accuracy of *RTD* determination [109]. In FLUENT, *RTD* is calculated using the “Discrete Phase Model”. For the boundary conditions within the Discrete Phase Model, an injection of 20 000 massless particles distributed evenly at the tank-inlet is defined. The particle residence time depends on the particle starting position within the tank-inlet as well as the flow conditions within the tank. On the glass melt boundaries immediately adjacent to the electrodes and to the inner boundaries of the tank walls, the “reflect” boundary condition is applied to assure the conservation of all injected particles. On the tank-outlet boundary, the “escape” boundary condition is used. Thus, all injected particles are considered to leave the tank when they reach the tank-outlet boundary.

9.1.2 Selected results of the baseline-case simulation

The distribution of electric current density within the glass melt is first considered. The gradients caused by the spatial distribution of electric potential φ within the electrically conducting glass melt generate electric current density \underline{J} . The resultant electric current density distribution depends on the temperature distribution and the flow within the glass melt. This is due to the

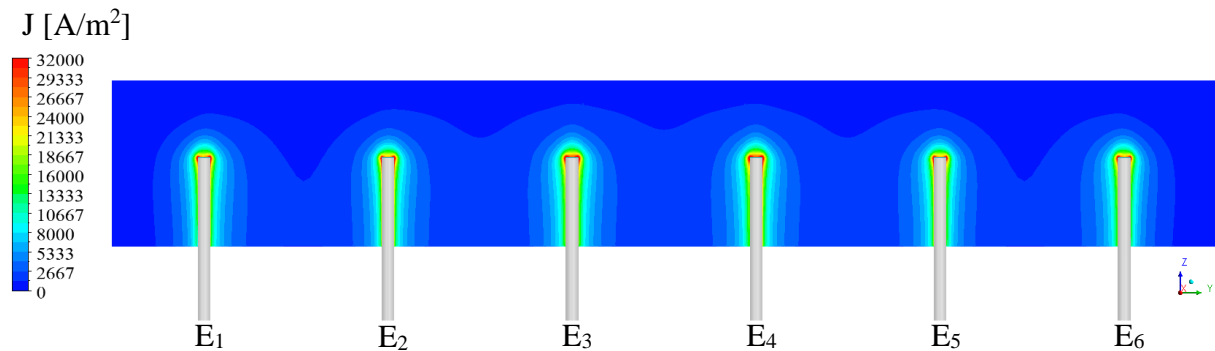


Figure 9.2: The distribution of electric current density magnitudes (effective) within the glass melt in a sectional plane across the electrodes, in the baseline-case.

Electrode	E1	E2	E3	E4	E5	E6
$ \underline{I}_E $	2044.92 A	2013.92 A	2304.15 A	2304.60 A	2013.92 A	2044.88 A

Table 9.3: Magnitude of the effective electric currents flowing through the bottom-surface of the electrodes.

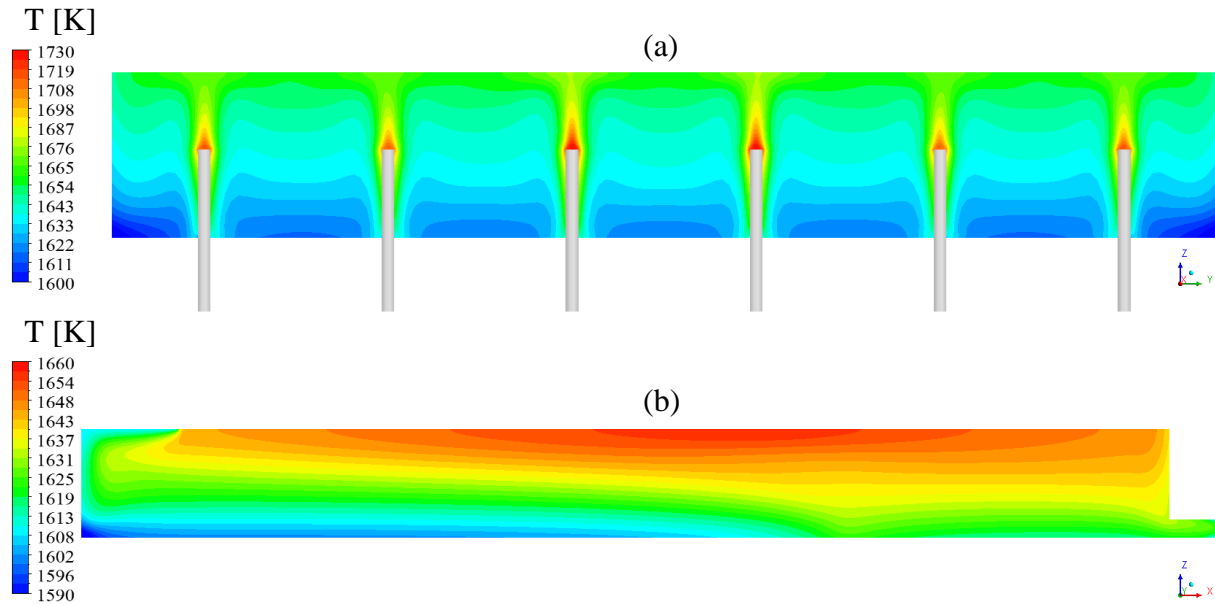


Figure 9.3: The temperature distribution within the glass melt in the baseline-case (a) in a sectional plane across the electrodes and (b) in a sectional plane along the tank centerline between the middle electrodes (E₃ and E₄).

temperature-dependent electrical conductivity of the glass melt as previously explained. Figure 9.2 demonstrates the resultant electric current density distribution within the glass melt in a sectional plane across the electrodes. The largest intensities of electric current density exist around the electrodes. The effective values of electric currents flowing through the bottom-surface of the electrodes are shown in Table 9.3.

The typical gradual decrease of temperature from the surface to the bottom in industrial glass-melting tanks is simulated. This is evident in Figure 9.3 (b), in which the temperature field within the glass melt is demonstrated in a sectional plane along the tank centerline between the middle electrodes (E₃ and E₄). In Figure 9.3 (a), the temperature distribution within the glass melt is presented in a sectional plane across the electrodes. From the figure, it is obvious that the effect of Joule heat generated by *EB* system is localized near the electrodes. The glass melt is thus locally heated to generate a thermal convection current, forcing the bottom glass melt towards the surface. In Figure 9.4, the *z*-velocity of the glass melt is presented in a sectional plane across the electrodes. Since the *z*-axis is set in the simulation against gravitational acceleration, the higher positive *z*-velocity means that the glass melt is being lifted to the surface. In the figure, the *EB* effect of lifting the bottom glass melt is obvious near the electrodes. However, in the spaces between the electrodes, *EB* is less effective for a region of about 60% of the spacing. In this region, the colder bottom glass melt flows directly towards the tank-outlet without being adequately recirculated within the tank. The result is very low residence times. This part

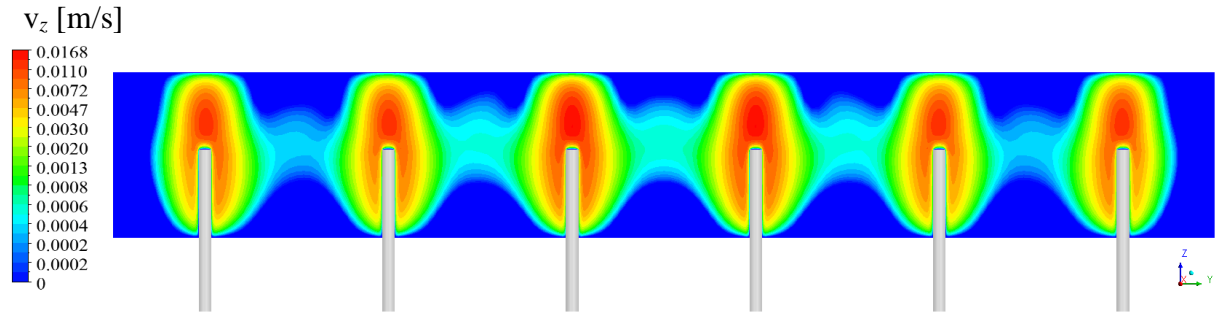


Figure 9.4: z -velocity of the glass melt in a sectional plane across the electrodes, in the baseline-case.

of the glass melt will not be sufficiently processed, impairing the quality of the final glass product.

For the present work, the most important results concern *RTD*. Figure 9.5 depicts the **F** curve (cumulative *RTD*) of the baseline-case, which is also compared with the hypothetical ideal **F** curve. The *RTD* calculation in the baseline-case shows that $MRT = 8081.44 \text{ s} \approx 2.24 \text{ h}$. This *MRT* is necessary to attain the glass quality required to satisfy the quality standards. This characteristic *MRT* is only attainable at the predetermined glass mass flow rate through the tank $\dot{m} = 100 \text{ T/D}$. Furthermore, in the baseline-case, it is not possible to increase the tank productivity (the glass mass flow rate) because this would result a shorter *MRT* and the required glass quality would not be attained. The mean residence time of the baseline-case is $\tau = 105730.64 \text{ s} \approx 29.37 \text{ h}$, which is derived from Equation (2.2). $MRT/\tau = 0.07643$ means that *MRT* is about 7.6% of τ . The *RTD* comparison shows that about 65% of the glass melt particles leave the tank after residence times shorter than τ , as is clear in Figure 9.5 for the time domain where $t < \tau$. These glass melt particles have a lower quality than the ideal. Furthermore, the particles with the *MRT* are considered to have the lowest quality. However, the closer the particle residence time is to τ , the better the quality of the particle. The particles that leave the tank after residence times longer than τ (in the time domain where $t > \tau$) have reached the ideal quality. However, they waste energy because they stay within the tank for times longer than required. A very important descriptive parameter of *RTD* is the spread σ which measures the deviation from the mean residence time τ :

$$\sigma = \sqrt{\frac{1}{N} \sum_1^N (t_i - \tau)^2}, \quad (9.2)$$

where N is the total number of the tracked particles and t_i is the residence time of every tracked particle. A lower spread indicates that the *RTD* tends to be closer to the ideal case. The spread of the ideal case is zero, since $t_i = \tau$. The characteristic spread of the baseline-case is $\sigma = 114250.8816 \text{ s} \approx 31.74 \text{ h}$.

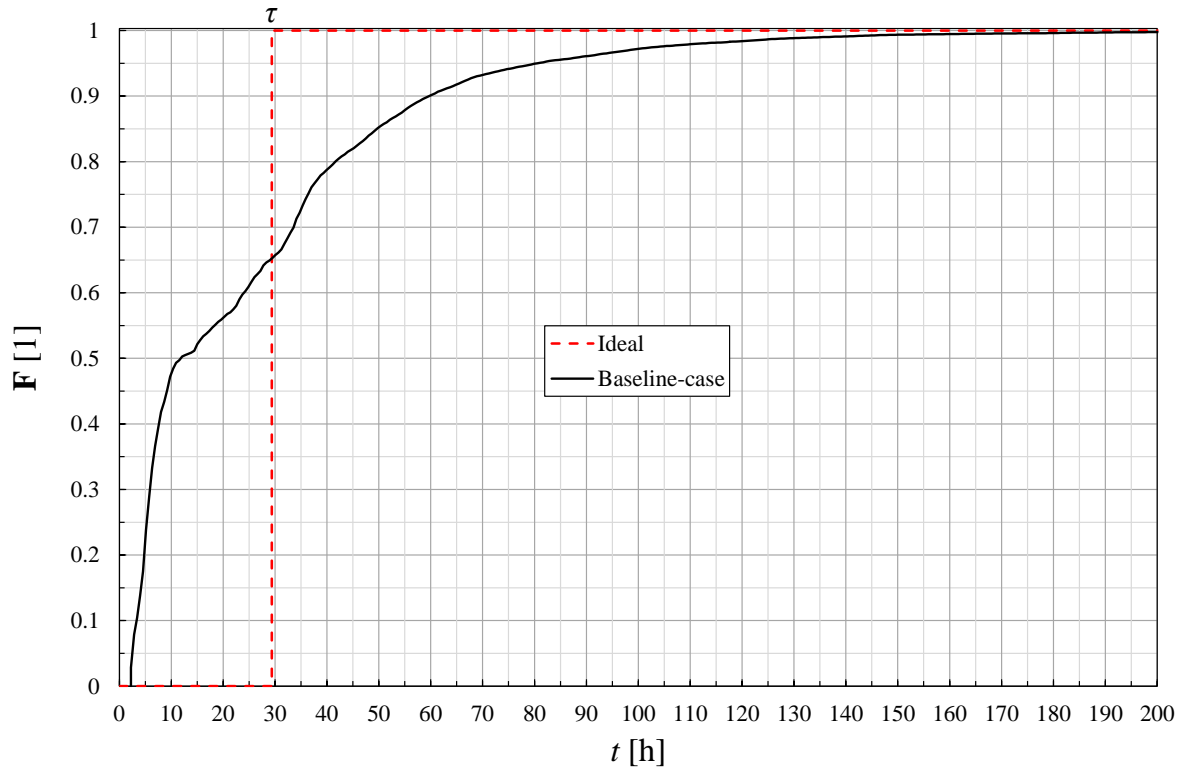


Figure 9.5: The F curve (cumulative RTD) of the baseline-case compared with the hypothetical ideal F curve.

Summary of simulation of the baseline-case

The simulations performed with the commercial software FLUENT use the method presented in Section 7.5 for coupling the calculations. The ordinary operation case of the continuous glass-melting tank is the starting (baseline) case for comparisons to study the dynamic system behavior. The distributed three-phase scheme applied to energize the boosting electrodes in the real industrial tank is simulated. The effective values of electromagnetic field parameters are used for the simulation. The boundary conditions of the baseline-case are chosen to simulate the realistic conditions in the real industrial continuous glass-melting tank. For an accurate RTD calculation, 20 000 massless particles distributed evenly at the tank-inlet are tracked. The simulation results are found to agree qualitatively with the expected characteristics of industrial continuous glass-melting tanks.

It should be noted that the parameters of the baseline-case will be denoted by the index “0”, e.g. MRT_0 , in what follows, as it is the starting point for comparisons.

9.2 Adapting the *EMB* system

To realize *EMB* in continuous glass-melting tanks, it is necessary firstly to incorporate a circuit arrangement for operating the magnet coils. In effect, the electrical phase applied to each magnet coil must be determined so that their alternating magnetic field together with the alternating electric currents flowing through the glass melt result in Lorentz forces that always run against the main flow direction within the tank. The electrical phase distribution of the magnet coils system is thus determined on the basis of the existing electric current densities that flow through the glass melt between the electrodes. These electric currents are generated according to the circuit arrangement given in Figure 3.3 and Table 9.2. Both Figure 9.6 and Table 9.4 describe how the electrical phase distribution of the magnet coils system is adapted to generate artificial Lorentz forces that run against the main flow direction in the tank. The electrical phase is distributed in a 60° sequence from the coil C_1 to the coil C_5 on the basis of vector difference

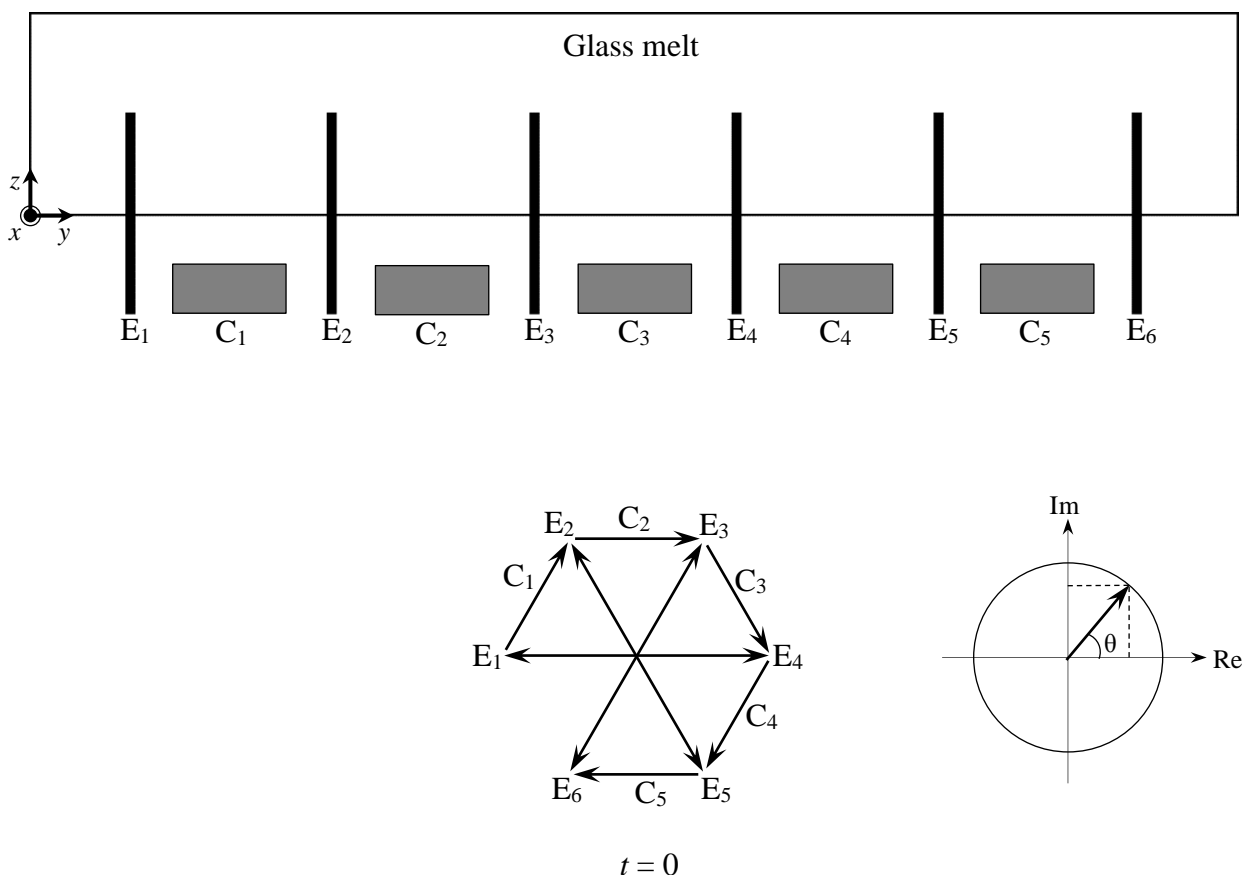


Figure 9.6: Determination of the electrical phase distribution for operating the magnet coils ($C_{1,\dots,5}$) so that *EMB* can be realized in the continuous glass-melting tank. The electrical phase for each coil is determined on the basis of vector difference between the electrode voltages in the complex plane.

Coil	Angle	Electrical phase	Real component of the effective coil current $\underline{I}_C \text{ Re}$	Imaginary component of the effective coil current $\underline{I}_C \text{ Im}$
C_1	60°	- S	$ \underline{I}_C \cos(60^\circ)$	$ \underline{I}_C \sin(60^\circ)$
C_2	0°	+ R	$ \underline{I}_C \cos(0^\circ)$	$ \underline{I}_C \sin(0^\circ)$
C_3	-60°	- T	$ \underline{I}_C \cos(-60^\circ)$	$ \underline{I}_C \sin(-60^\circ)$
C_4	-120°	+ S	$ \underline{I}_C \cos(-120^\circ)$	$ \underline{I}_C \sin(-120^\circ)$
C_5	180°	- R	$ \underline{I}_C \cos(180^\circ)$	$ \underline{I}_C \sin(180^\circ)$

Table 9.4: The coil currents of the magnet system.

between the electrode voltages in the complex plane, as shown in Figure 9.6. This corresponds to the electrical phase operating within the glass melt between each electrode and its neighbor. That way the electrical phase of the coil magnetic field is matched with that of the electric current within the glass melt. Furthermore, it is essential to apply the same frequency to the magnet coils system as that used for the *EB* system, i.e. 50 Hz, in order to synchronize the phase alterations and prevent the additionally generated Lorentz forces from changing their direction. Table 9.4 also shows how the coil currents are defined (at $t = 0$) to calculate the complex magnetic flux density of the coils \underline{B}_C using the Biot-Savart law (Equation (6.14)). To examine the correctness of the adapted circuit arrangement, a test simulation is performed on a simplified example. The test simulation confirms that the Lorentz forces act in the desired direction.

9.3 Optimizing the *EMB* system

9.3.1 The optimum *MRT*

The simulations are now performed for the baseline-case with *EMB* applied, so as to investigate the *EMB* effects on the ordinary tank operation. For the *EMB* system, the assumption is that each coil has 20 turns with an outer diameter of 600 mm, as defined in Section 6.1. Since the coil current passed through the coils I_C is the external control parameter for *EMB*, it is varied in the simulation to obtain the optimum *EMB* effect. In the following, the effective value of the electric current passed through each coil $|I_C|$ will be simply denoted as I_C .

As the desired effect of *EMB* is an increase in *MRT*, a systematic study is carried out to attain the highest *MRT*. During the study, I_C is systematically increased from 0 A (the baseline-case) up to 1400 A, with a maximum interval of 200 A and a minimum interval of 25 A. Accordingly, the intensity of the additionally generated Lorentz forces is raised systematically, meaning that the intensity of the electromagnetic wall created between the electrodes is systematically increased. Figure 9.7 depicts the resulting *MRT* as I_C changes. The *maximal* increase obtained for *MRT* is about 82.4%. This is attained at $I_C = 425$ A. The study reveals that increasing I_C more than 425 A leads to a decrease in *MRT* from the attained value, as is evident in Figure 9.7. The main reason for that is thought to be the increase of the glass melt velocity towards the tank-

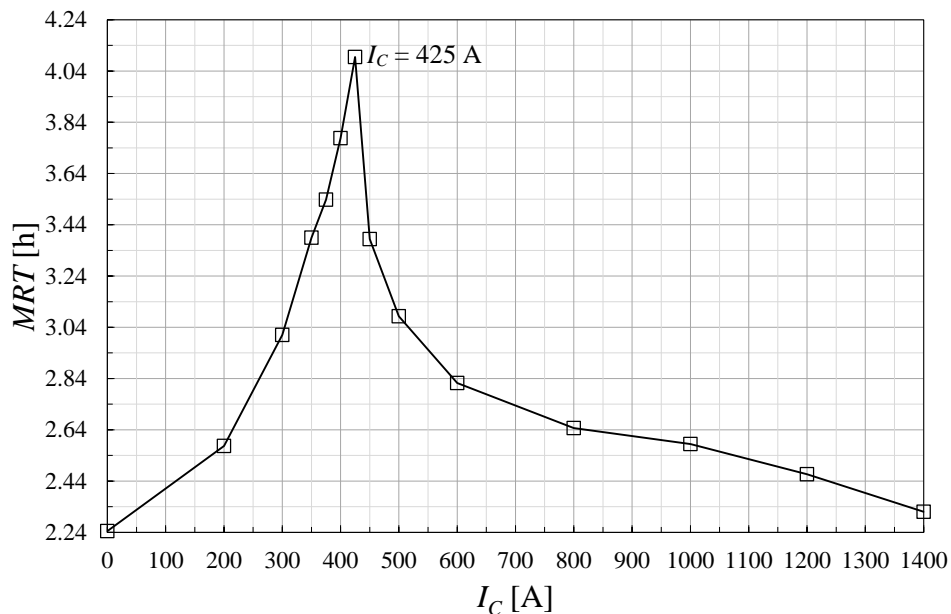


Figure 9.7: *MRT* as a function of the coil current I_C , the highest *MRT* is attained at $I_C = 425$ A.

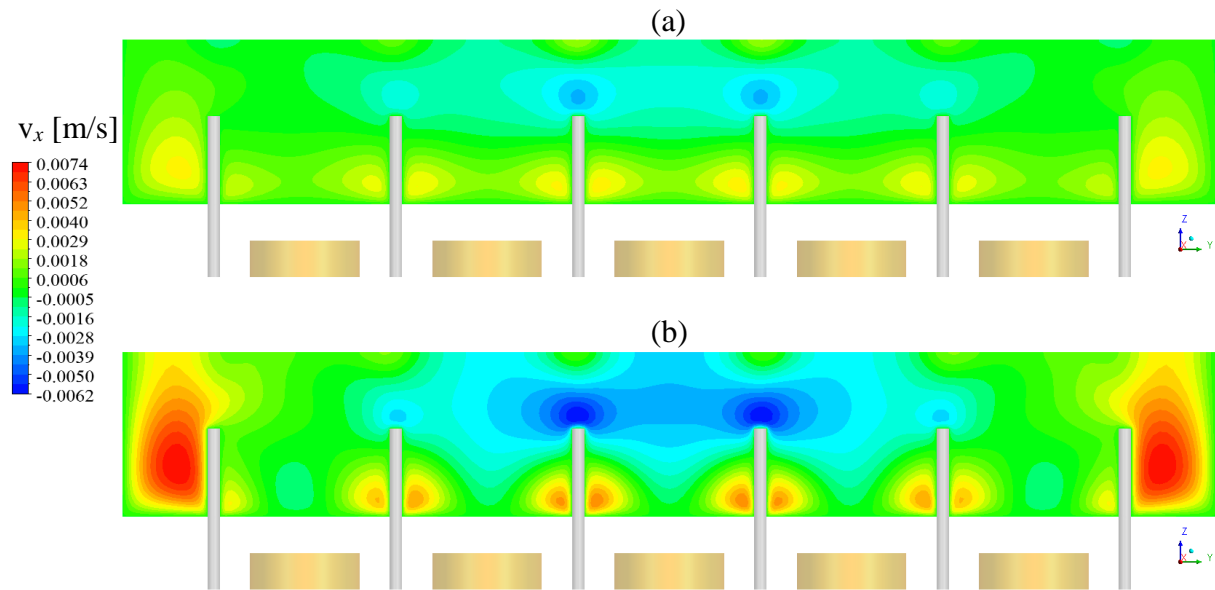


Figure 9.8: x -velocity of the glass melt in a sectional plane across the electrodes, in the case with *EMB* (a) at $I_C = 425$ A and (b) at $I_C = 1400$ A.

outlet in the two small areas where no artificial Lorentz forces are generated. These two areas are located between each tank side-wall and its neighboring electrode (E_1 and E_6). Increasing I_C results in higher intensities of Lorentz force density between the electrodes, and thus an intensification of the flow impediment between the electrodes. This gives rise to stronger flows through the two barrier-free areas. This dynamic behavior is also indicated in Figure 9.8, in which a comparison of the glass melt x -velocity is demonstrated in a sectional plane across the electrodes. The comparison is between the cases of $I_C = 425$ A and $I_C = 1400$ A. The higher positive x -velocity means that the glass melt is flowing towards the tank-outlet at a higher velocity.

It thus becomes obvious that the optimum *EMB* performance, assuming predetermined glass composition and electrode currents, requires a *specific* coil current value, given the predetermined diameter and number of turns of the coil. In fact, the coil current shown as necessary in the model ($I_C = 425$ A) is low in comparison with the current in the electrodes (Table 9.3).

9.3.2 Coil diameter study

For the magnet coils, an outer diameter $\varnothing = 600$ mm is assumed with the intention of covering the area in which *EB* is less effective. However, it is necessary to precisely determine the optimum coil diameter by systematic study. The present subsection reports systematic study in which the coil diameter is varied to attain the highest *MRT*. For each coil, constant coil current

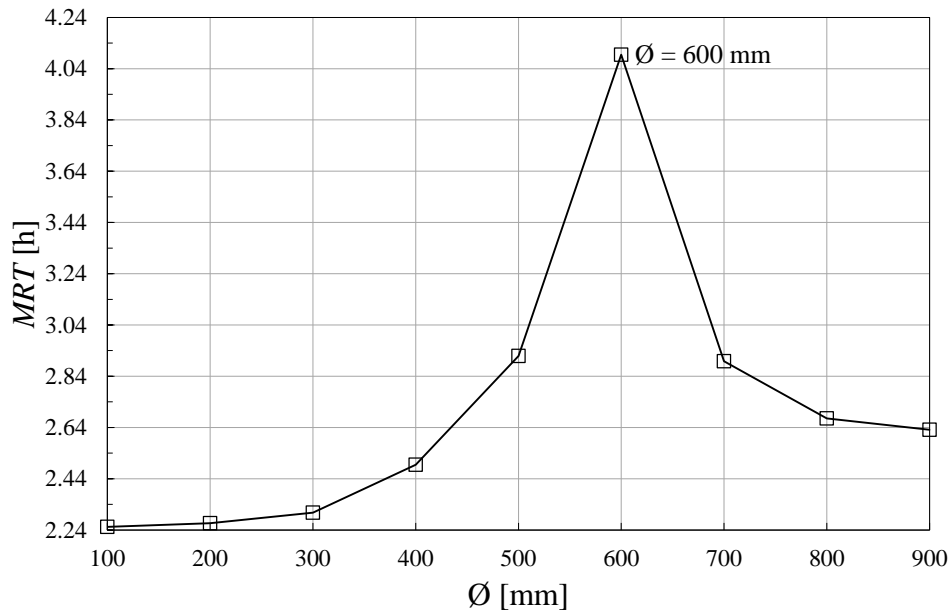


Figure 9.9: MRT as a function of the outer coil diameter \varnothing (at $I_C = 425$ A), the highest MRT is attained at $\varnothing = 600$ mm.

$I_C = 425$ A and 20 turns are considered. During the study, the coil outer diameter \varnothing is systematically increased from 100 mm up to 900 mm with an interval of 100 mm. Figure 9.9 depicts the resulting MRT as \varnothing changes. It is evident that the maximal MRT is attained at $\varnothing = 600$ mm, as expected. The study reveals that increasing \varnothing more than 600 mm leads to a fall in MRT from the attained value.

Conclusions drawn from the parameter analyses

It is possible to increase the MRT in the continuous glass-melting tank by EMB . The optimum EMB performance, assuming predetermined glass composition and electrode currents, is attained in the case of $\varnothing = 600$ mm and $I_C = 425$ A, assuming 20 turns for each coil. These conditions result in the optimum EMB effect and will be called the “ EMB -case”. So, in the following, the EMB -case refers to the tank operation case with EMB at $\varnothing = 600$ mm and $I_C = 425$ A, assuming 20 turns for each coil. It is interesting to note that ohmic loss within the coils in the EMB -case is about 10 kW, assuming the conductor profile defined in Section 6.1. This power amount is very low in comparison with the electric power used by the EB system (700 kW).

9.4 Comparison between the baseline-case and EMB-case

In Sections 9.2 and 9.3, the *EMB* system was adapted and optimized. Now follows an analysis of the dynamic system behavior with and without *EMB* by comparing the baseline-case and the *EMB*-case. The most important parameter for evaluating the tank performance is *RTD*. Figure 9.10 depicts the \mathbf{F} curves (cumulative *RTD*) of the baseline-case and *EMB*-case. Furthermore, both curves are compared with the hypothetical ideal \mathbf{F} curve (the broken lines). The

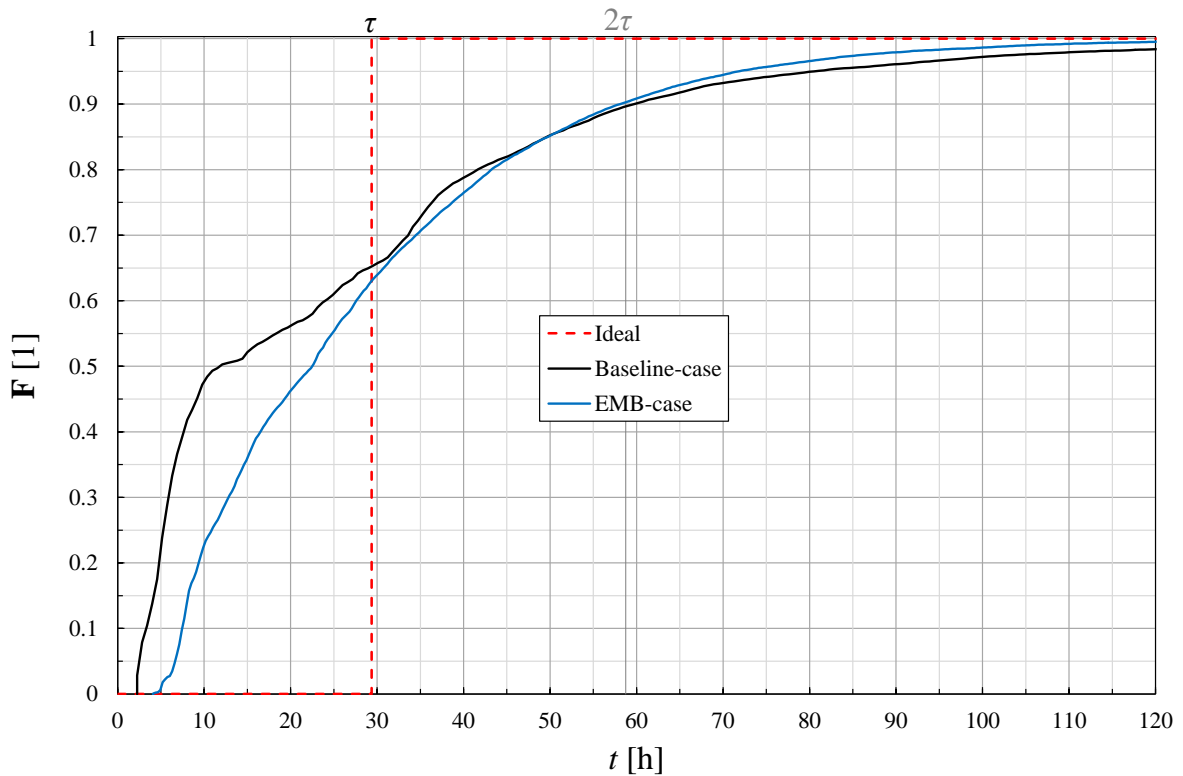


Figure 9.10: Comparison between the \mathbf{F} curves (cumulative *RTD*) of the baseline-case and the *EMB*-case. Both are also compared with the hypothetical ideal \mathbf{F} curve.

Case	MRT	MRT/MRT_0	MRT/τ	σ	σ/σ_0
baseline-case	8081.44 s	1	0.076	114250.88 s	1
<i>EMB</i> -case	14740.00 s	1.824	0.139	81394.83 s	0.712

Table 9.5: Evaluation of the tank performance in the baseline-case and *EMB*-case.

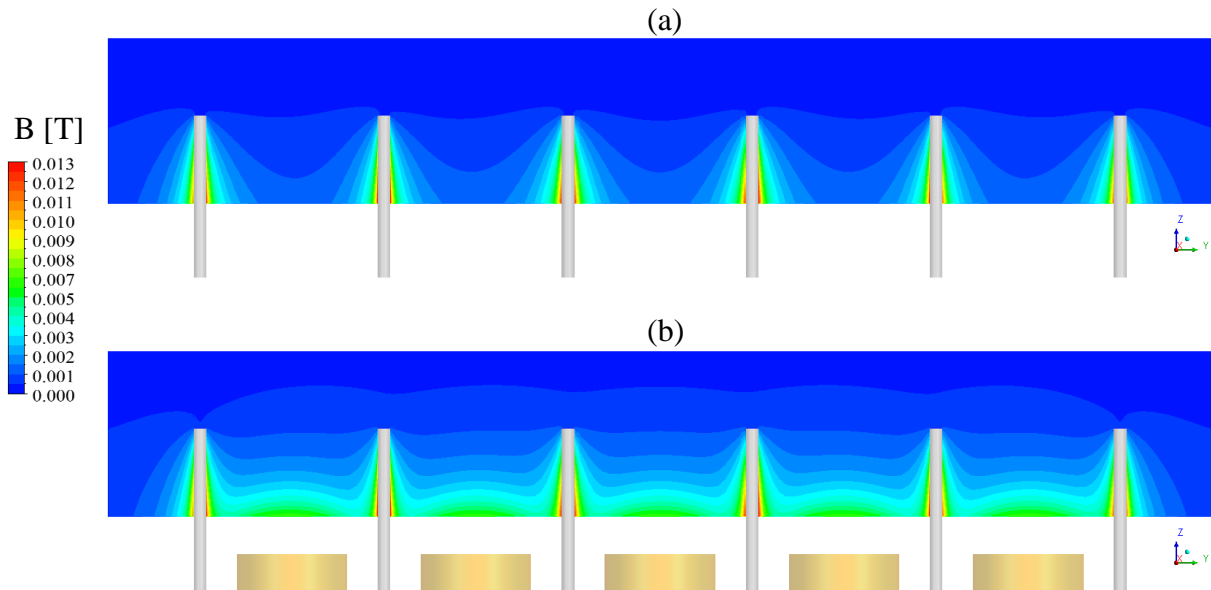


Figure 9.11: The distribution of magnetic flux density magnitudes (effective) within the glass melt in a sectional plane across the electrodes (a) in the baseline-case and (b) in the EMB-case.

mean residence time τ is the same for both cases, being defined by Equation (2.2). *MRT* of the baseline-case is about 7.6% of τ , while that of the EMB-case is about 13.9% of τ . The *RTD* comparative analysis shows that in the EMB-case, *MRT* is increased by about 82.4%. Moreover, the *RTD* comparison in Figure 9.10 shows that about 15% of the glass melt particles in the baseline-case have residence times that are lower than the *MRT* of the EMB-case. These glass melt particles have quality lower than the minimum quality in the EMB-case. In the time domain where $t < \tau$, the EMB-case allows fewer particles to leave the tank, so that the glass melt will have a longer processing time and consequently a better quality. Moreover, if the time domain exceeds twice the mean residence time $t > 2\tau$, the EMB-case allows more particles to leave the tank, shortening the unnecessary processing. The EMB-case has thus a spread σ that is reduced by about 28.8%. In Figure 9.10, it is obvious how the **F** curve (cumulative *RTD*) is brought closer to the ideal case by *EMB*. As a result, the timed distribution of the energy consumed will be more homogeneous and, consequently, the glass quality will be enhanced. The tank performance evaluation in the baseline-case and EMB-case is summarized in Table 9.5.

Figure 9.11 presents a magnitude comparison of the magnetic flux density distribution within the glass melt in a vertical plane across the electrodes. The comparison is between the baseline-case and EMB-case. In both cases, the eigenfield induced by the electrode currents has similar intensities surrounding the electrodes. In the EMB-case, the additional magnetic flux density generated by the coils (at $I_C = 425$ A) between the electrodes can be distinguished. This magnetic flux density has a maximum intensity of about 6 mT at the bottom of the glass bath. The

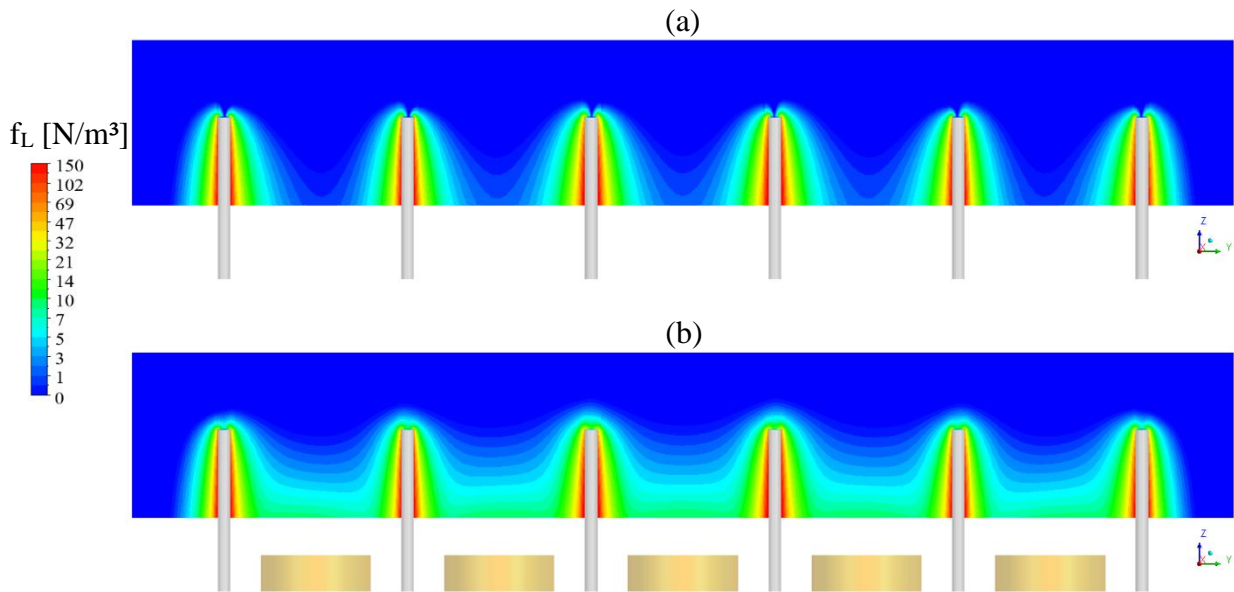


Figure 9.12: The distribution of Lorentz force (time averaged) density magnitudes within the glass melt in a sectional plane across the electrodes (a) in the baseline-case and (b) in the EMB-case.

Lorentz force (time averaged) density distributions within the glass melt of both cases are also compared in a vertical plane across the electrodes, see Figure 9.12. In both cases, the natural Lorentz force density exists in the vicinity of the electrodes. It is obvious in the figure that the natural Lorentz force density has a considerable intensity (maximally about 150 N/m^3) in the direct vicinity of the electrodes in both cases. However, away from the electrodes, this high intensity decreases rapidly. The reason for the relatively high natural Lorentz force intensity near the electrodes, although the eigenfield intensity is relatively small, is the very high electric current densities flowing in the vicinity of the electrodes. In the EMB-case (Figure 9.12 (b)), artificial Lorentz force density is additionally generated in the gaps between the electrodes with a maximum intensity of about 10 N/m^3 at the bottom of the glass bath. Figure 9.13 illustrates the vectors of the additionally generated Lorentz force density. These vectors are unidirectional against the main flow direction within the tank, which confirms that the electrical phases of the coils are determined correctly. In Figure 9.14, the x -velocity profiles of the glass melt are also compared in a vertical plane across the electrodes between both cases. In the figure, it is obvious how the flow of the bottom glass melt in the gaps between the electrodes is retarded in the EMB-case. The lower positive x -velocity near the bottom between the electrodes in the EMB-case (Figure 9.14 (b)) means that the flow of glass melt towards the tank-outlet is slowed down. In the two small barrier-free areas which are located between each tank side-wall and its neighboring electrode (E_1 and E_6), some increase in x -velocity is observed. Furthermore, in the EMB-

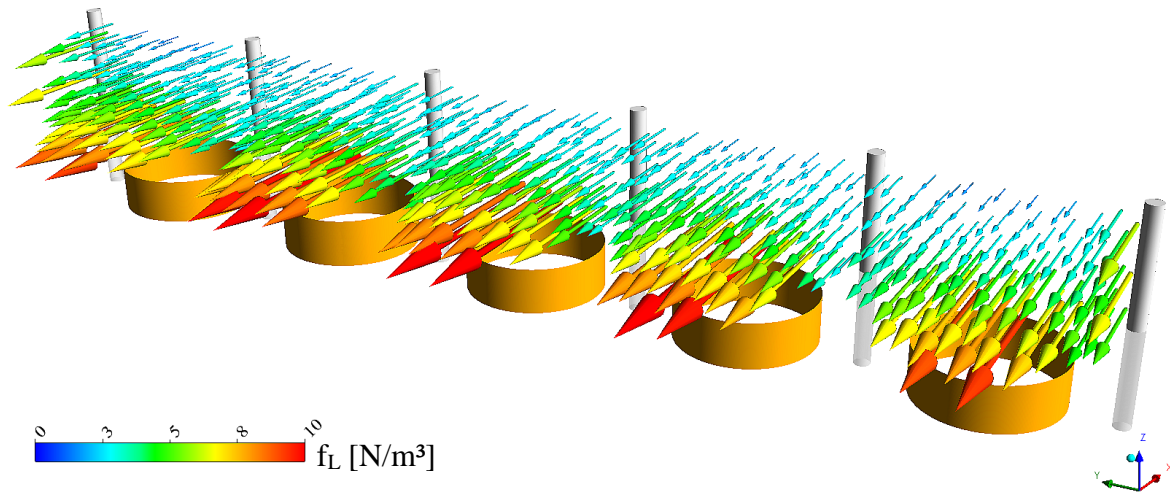


Figure 9.13: The distribution of the additionally generated Lorentz force (time averaged) density vectors within the glass melt in a sectional plane across the electrodes, in the EMB-case.

case, the higher negative x -velocity above the electrodes, especially the middle ones (E_3 and E_4), means that the recirculating flow of the glass melt towards the melting zone is intensified. As a result, the glass melt will be processed for longer, improving the melting performance. The effect of the additionally generated Lorentz forces on the glass melt flow is visualized in Figure 9.15, which shows the streamlines of three glass melt particles which are released from the tank-inlet and have the MRT . In the baseline-case (Figure 9.15 (a)), the particles in the flow of glass melt near the bottom pass through the gaps between the electrodes directly to the tank-outlet, without adequate recirculation within the tank. This causes very short residence time and impairs the glass quality. In the EMB-case (Figure 9.15 (b)), these particles are prevented from passing through the gaps between the electrodes. The glass melt particles continue to recirculate within the tank, following longer streamlines to the tank-outlet, with higher residence time. Thus, the glass melt particles that have very low residence time in the baseline-case will be processed for longer in the EMB-case, which has a positive effect on the glass quality. It is remarkable that the streamlines in the EMB-case have an asymmetric tendency although the additional Lorentz forces have symmetric distribution. The reasons for that are presumably the nonlinearity of the momentum equation and the integrated numerical error due to the longer streamlines.

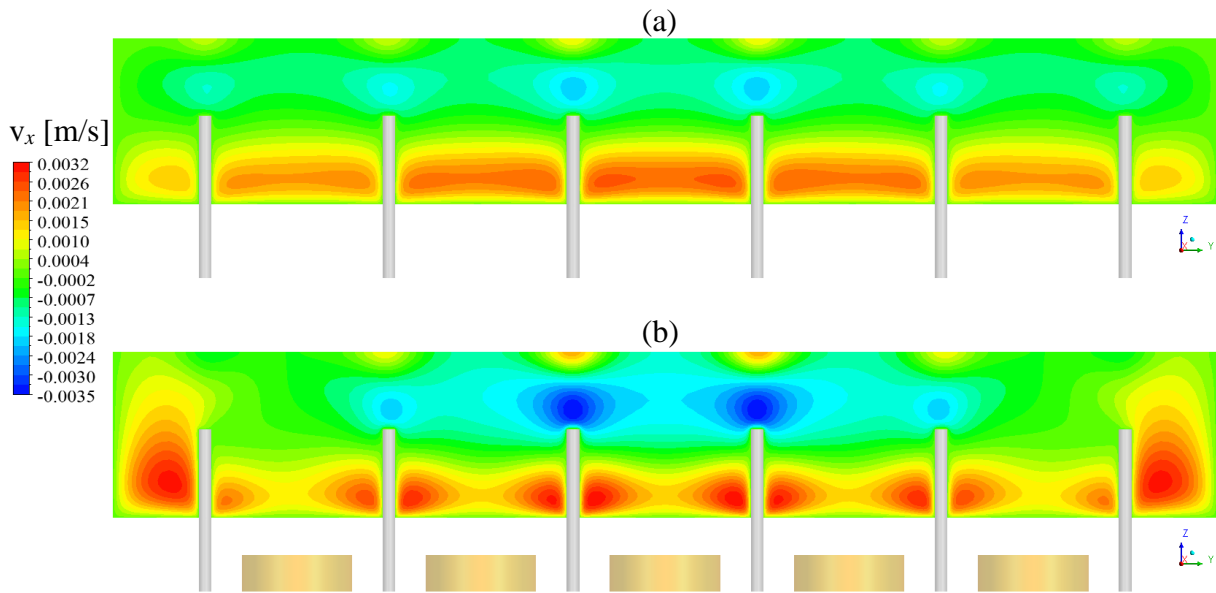


Figure 9.14: x -velocity of the glass melt in a sectional plane across the electrodes (a) in the baseline-case and (b) in the EMB-case.

Summary of the two compared cases

The dynamic system behavior within the continuous glass-melting tank is studied with and without the additionally generated Lorentz forces. The study compares the tank operation under the pre-calculated optimum *EMB* conditions (the EMB-case) with the ordinary tank operation (the baseline-case). The boundary conditions are chosen to simulate the realistic conditions in the industrial continuous glass-melting tank. In the simulations performed, the effective values of electromagnetic field parameters are applied. The simulations prove that the circuit arrangement proposed in Section 9.2 is appropriate for realizing *EMB* in the continuous glass-melting tank. Basically, it is possible to prevent the bottom glass melt from flowing directly to the tank-outlet through the gaps between the electrodes by using additionally generated Lorentz forces. For an accurate *RTD* presentation, 20 000 massless particles distributed evenly at the tank-inlet are tracked. The simulation results show that the desired *EMB* effect of *increasing* the *MRT* and consequently *improving* the *RTD* is achieved, ultimately resulting in enhanced glass quality. The EMB-case has an *MRT* that is increased by about 82.4%, and a spread σ that is reduced by about 28.8%.

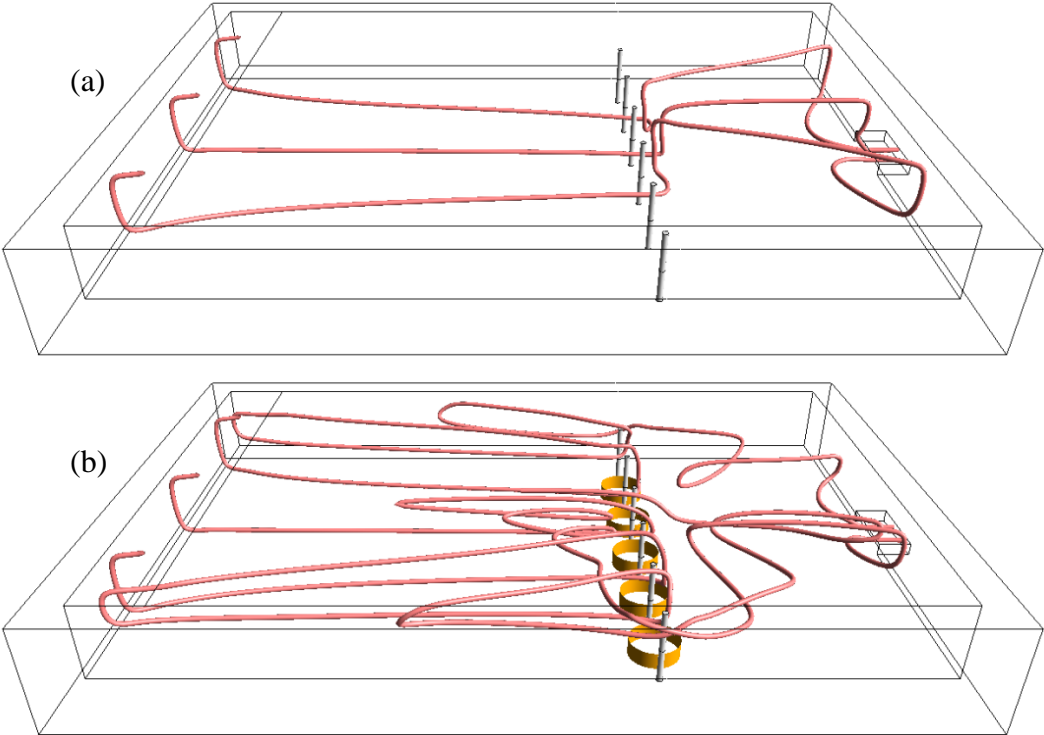


Figure 9.15: The streamlines of three glass melt particles released from the tank-inlet (a) in the baseline-case and (b) in the EMB-case, in both cases all three particles with *MRT*.

9.5 Increasing the tank productivity

Increasing the tank productivity means increasing the rate of flow of the glass mass through the tank. In other words, the aim is to produce more glass mass per time unit. However, this would result in MRT shorter than the required MRT_0 and the required glass quality would not be attained. In the last section, the EMB capability of increasing MRT has been shown. It is now possible to go further than this and investigate the EMB capability of retaining MRT as required while increasing the mass flow rate through the tank. To investigate the potential of increasing the tank productivity under EMB , the mass flow rate at the tank-inlet is systematically increased for the EMB -case from the ordinary value $\dot{m}_0 = 100$ T/D up to $4.5\dot{m}_0$ with an interval of $0.5\dot{m}_0$. Figure 9.16 shows the resulting MRT as the normalized mass flow rate \dot{m}/\dot{m}_0 increases. The already increased MRT reverses to MRT_0 at a mass flow rate $\dot{m} = 4\dot{m}_0$, and a higher mass flow rate results in MRT lower than the required MRT_0 . It should be noted that in reality, increasing the ordinary glass mass flow rate requires a corresponding increase in the input heat transfer rate q_{in} introduced by combustion. Now, to compare the RTD spread for the considered cases, the normalized spreads (ratio σ/τ) of each case are compared, because the cases have different mean residence times (cf. Equation (2.2)). The comparison is summarized in Table 9.6. The EMB -case at all mass flow rates considered is seen to be always characterized by a σ/τ value that is lower than that of the baseline-case. Clearly, the timed distribution of the energy consumed will be more homogeneous as the spread is reduced. Moreover, the comparison highlights the EMB capability of providing a glass quality higher than the ordinary while $\dot{m} > \dot{m}_0$.

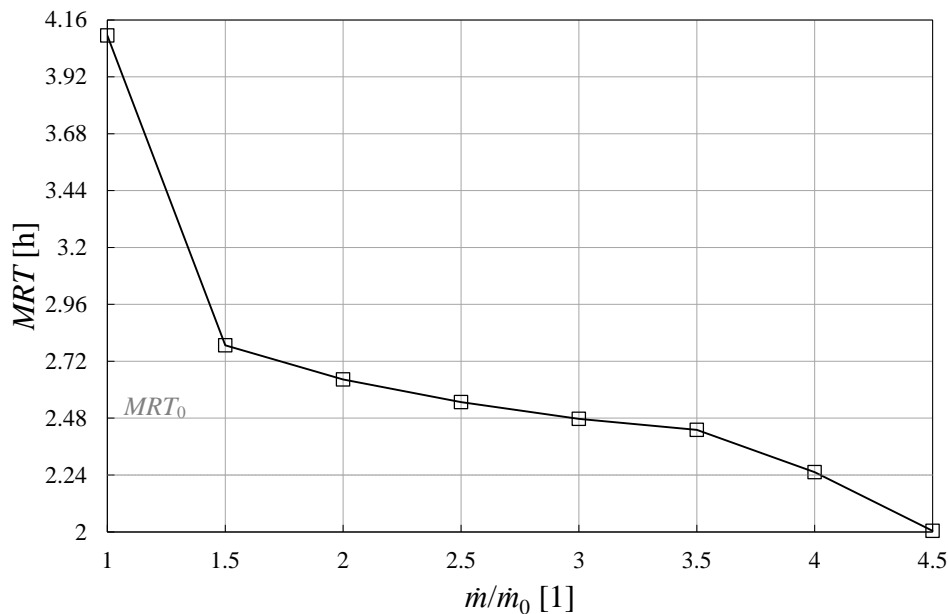


Figure 9.16: MRT as a function of the normalized mass flow rate \dot{m}/\dot{m}_0 in the EMB -case.

No.	Case	τ	\dot{m}/\dot{m}_0	MRT/MRT_0	MRT/τ	σ/τ
0	baseline-case	≈ 29.37 h	1	1	0.076	1.081
1	EMB-case	≈ 29.37 h	1	1.824	0.139	0.770
2		≈ 20.18 h	1.5	1.242	0.138	0.620
3		≈ 15.20 h	2	1.178	0.174	0.566
4		≈ 12.17 h	2.5	1.135	0.209	0.542
5		≈ 10.14 h	3	1.103	0.244	0.564
6		≈ 8.69 h	3.5	1.083	0.280	0.556
7		≈ 7.60 h	4	1.003	0.296	0.569

Table 9.6: Evaluation of the tank performance at increased productivity in the EMB-case.

This corresponds to the cases in which $MRT > MRT_0$ at $\dot{m} > \dot{m}_0$ (cases No. 2, 3, 4, 5, and 6). However, increasing the glass mass flow rate through the tank to $4\dot{m}_0$ is only a theoretical assumption. It would in reality require considerable pushing of the firing system of the furnace. As it is stated in the literature that, under super conditions, the tank output can be ultimately doubled [14], the case of $\dot{m} = 1.5 \dot{m}_0$ may be considered to be reasonable. Figure 9.17 depicts the \mathbf{F} curve (cumulative RTD) of the EMB-case at $\dot{m} = 1.5 \dot{m}_0$ in comparison with that of the baseline-case.

Conclusions drawn from tank productivity study

EMB in the continuous glass-melting tank offers the possibility of simultaneously increasing the MRT and the rate of flow of the glass mass through the tank. In other words, it will be possible to obtain improved glass quality while increasing the tank productivity using *EMB*. The RTD comparative analysis shows that increasing the mass flow rate through the tank in the EMB-case results in a reduced spread σ , with the effect of a more homogeneous timed distribution of the energy consumed. Without *EMB*, higher productivity requires a larger tank volume to retain the required MRT_0 . Hence, using *EMB* to increase the tank productivity without increasing the tank volume can save the costs required for larger tank construction.

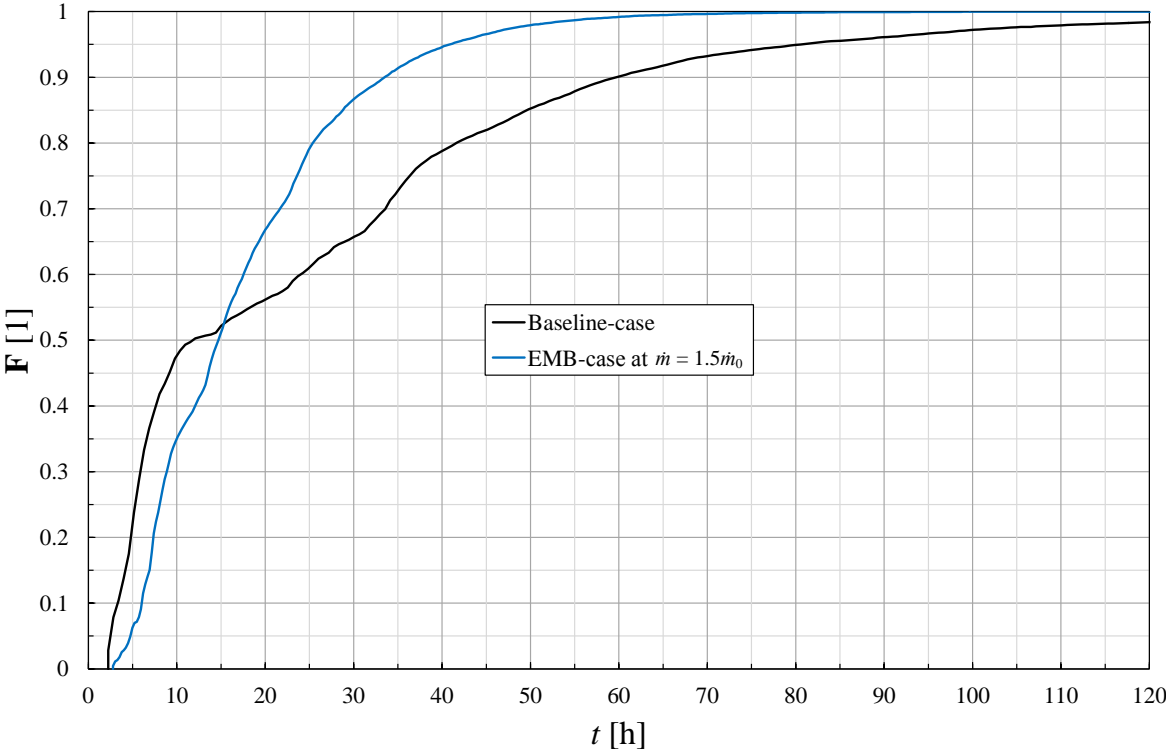


Figure 9.17: F curves (cumulative RTD) comparison between the EMB-case at $\dot{m} = 1.5 \dot{m}_0$ and the baseline-case.

9.6 Increasing the tank thermal efficiency

In the ordinary tank operation case, if higher tank productivity is required, a larger tank volume should be used to attain the required MRT_0 . This gives rise to higher thermal energy exchange with the surroundings through the tank walls, cf. Equations (6.21) and (6.22), so that the wall losses q_{cool} will increase. *EMB* offers the possibility of increasing the tank productivity without increasing its volume, thus keeping the wall losses q_{cool} constant. This is to be interpreted as *energy saving* that is evaluated by the tank thermal efficiency. The present section is concerned with the theoretical investigation of how the tank thermal efficiency is improved by increasing the tank productivity under *EMB*.

The ordinary tank thermal efficiency is calculated by

$$\eta_{th0} = \frac{q_{out0}}{q_{out0} + q_{cool}} , \text{ this also gives } q_{cool} = \frac{q_{out0}}{\eta_{th0}} - q_{out0} . \quad (9.3)$$

Under *EMB*, the ordinary tank output can be increased by the factor \dot{m}/\dot{m}_0 :

$$q_{out} = \frac{\dot{m}}{\dot{m}_0} \cdot q_{out0} , \quad (9.4)$$

where in the theoretical study $1 \leq \dot{m}/\dot{m}_0 \leq 4$.

The tank thermal efficiency resulting from an increased output will be

$$\eta_{th} = \frac{q_{out}}{q_{out} + q_{cool}} . \quad (9.5)$$

If q_{cool} and q_{out} (Equations (9.3) and (9.4) respectively) are substituted in Equation (9.5), the resulting equation is

$$\eta_{th} = \frac{\frac{\dot{m}}{\dot{m}_0}}{\frac{\dot{m}}{\dot{m}_0} + \frac{1}{\eta_{th0}} - 1} . \quad (9.6)$$

Equation (9.6) gives the relation between the tank thermal efficiency and the increased productivity. The ordinary thermal efficiency of the tank under consideration is assumed $\eta_{th0} = 0.75$. Now, the potential improvement in tank thermal efficiency can be investigated by increasing the ratio \dot{m}/\dot{m}_0 systematically. The ratio \dot{m}/\dot{m}_0 is raised from 1 up to 4 at intervals of 0.5, as described in the last section. Figure 9.18 depicts how the tank thermal efficiency η_{th} in the *EMB*-case increases together with the factor \dot{m}/\dot{m}_0 according to Equation (9.6). The details of the studied cases are also presented in Table 9.7. The cases at $1.5\dot{m}_0$ and $2\dot{m}_0$ can be considered to be realistic. The thermal efficiency in these two cases has been increased by 9.3 % and 14.7% respectively, which is advantageous in both economic and environmental terms. It should be

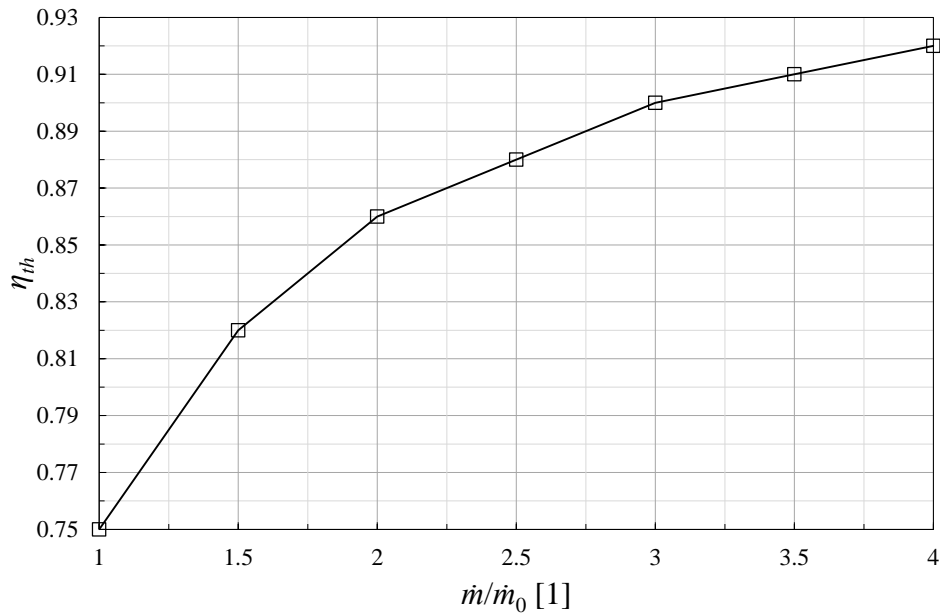


Figure 9.18: The tank thermal efficiency η_{th} as a function of the normalized mass flow rate \dot{m}/\dot{m}_0 in the EMB-case.

noted that this study considers the thermal efficiency of the tank and not of the whole furnace. In the furnace, the heat losses through the walls of the combustion chamber should be additionally taken into account. These losses may increase with the increased heat transfer rate introduced by combustion to melt the increased batch mass.

A final parameter to compare is the power saved by increasing the tank output using a certain amount of power to operate the coils. Taking the EMB-case at $1.5\dot{m}_0$ which is realistic and reasonable, the amount of power saved is about 265 kW, while the ohmic loss spent in the coils is about 10 kW.

These results lead to the conclusion that employing *EMB* in continuous glass-melting tanks can represent an efficient investment.

No.	Case	\dot{m}/\dot{m}_0	η_{th}	η_{th}/η_{th0}
0	EMB-case	1	0.75	1
1		1.5	0.82	1.093
2		2	0.86	1.147
3		2.5	0.88	1.173
4		3	0.90	1.200
5		3.5	0.91	1.213
6		4	0.92	1.227

Table 9.7: Evaluation of the tank thermal efficiency at increased productivity in the EMB-case.

9.7 Considering the structural steel girders

Structural steel girders are used in the construction of the tank to support it at the necessary height. Their position is below the tank. There follows here an investigation of whether these steel girders are affected by an additional magnetic field underneath the tank. The arrangement illustrated in Figures 9.19 and 9.20 is taken as the basis of the analysis. It consists of a glass melt cube with two immersed electrodes and an intermediate coil. Below this cube there are eight steel girders ($G_1, \dots, 8$) connected by two cross-girders (G_9 and G_{10}), at distances corresponding to the real distances. In reality, the girders have an I-shaped profile but only the upper part of the girders is considered in the simulation. A rectangle girder profile of 120×10 mm is thus assumed. It is the goal of this model to explore what may be the effects of the alternating magnetic field on the steel girders. It can be expected that eddy currents will be induced in the girders. The simulation is performed with the commercial software MAXWELL.

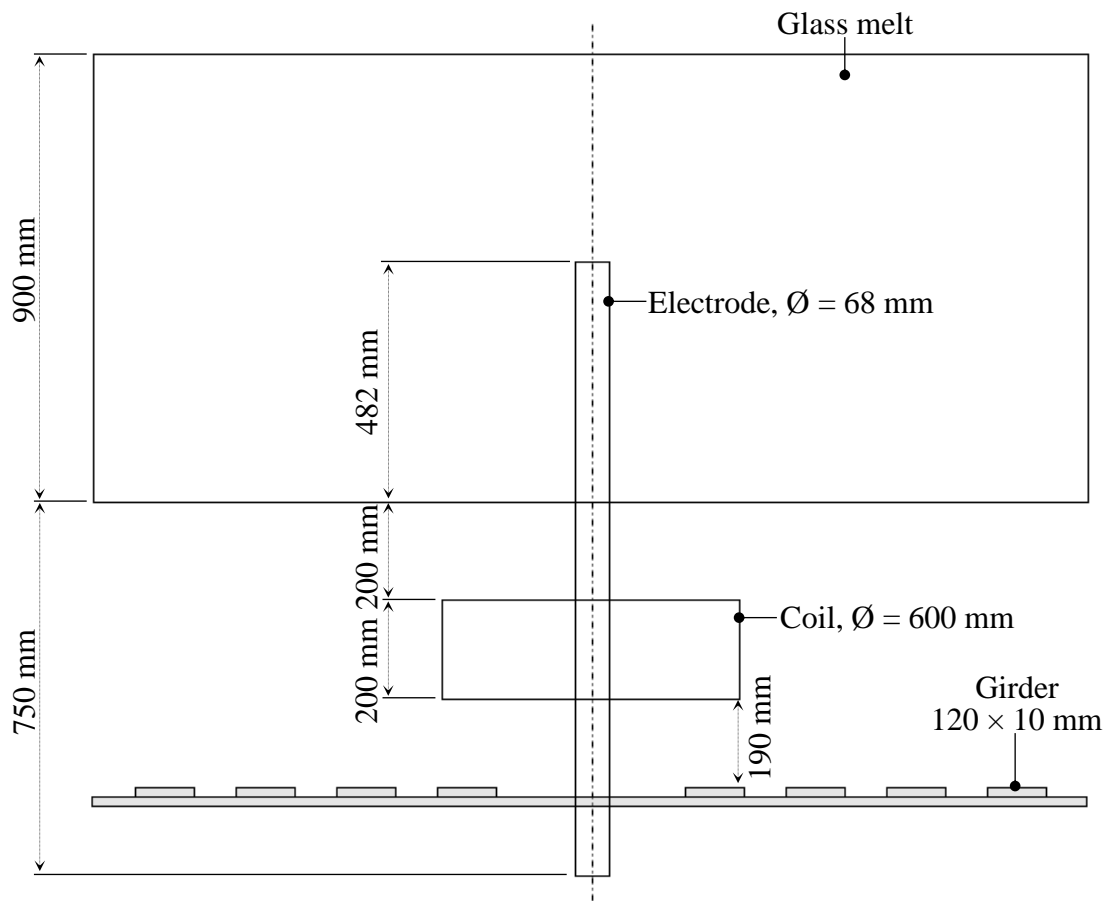


Figure 9.19: Schematic (side view) of the arrangement used as basis for investigating the effects of generating a time varying magnetic field under the tank, taking into account the presence of the steel girders.

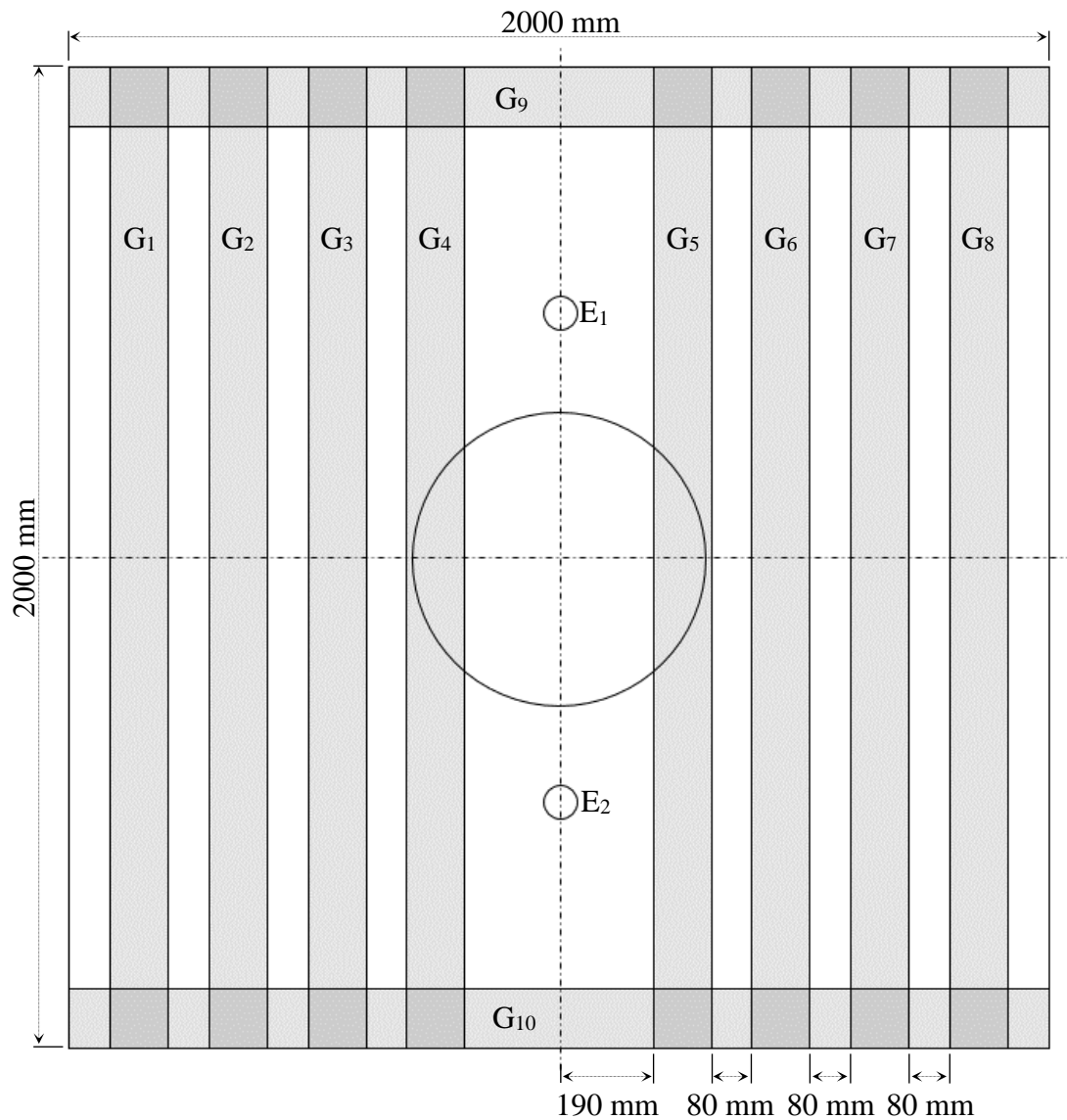


Figure 9.20: Schematic (top view) of the arrangement used as basis for investigating the effects of generating a time varying magnetic field under the tank, taking into account the presence of the steel girders.

9.7.1 Boundary conditions

The calculations are performed using the “Eddy Current” solver in MAXWELL, defining a system frequency as $f = 50$ Hz. Skin effect in the steel girders is considered, where skin depth δ is derived from

$$\delta = \frac{1}{\sqrt{\pi f \kappa \mu}} \quad (9.7)$$

κ and μ are respectively the electrical conductivity and magnetic permeability of the steel girders. The simulation assumes $\kappa = 7142857$ S/m and a simplified relative magnetic permeability $\mu_r = 1000$. With these assumptions $\delta = 0.842169$ mm. These material properties are typical of the S235JR type of structural steel which is usually used in the construction of glass-melting furnaces. To enhance the accuracy of the calculation, the case-characteristic skin depth $\delta = 0.842169$ mm is used to define a “Skin Depth Based” adaptive mesh refinement in MAXWELL, to be applied to the upper surface of the girders.

The coil is modeled as a single object made of copper conductor material, with a terminal in the cross section. On the terminal, the current source applied is a “Stranded” alternating current source with a peak value of $\sqrt{2} \times 425 \times 20$ A (assuming the effective value $I_C = 425$ A of the EMB-case). With the Stranded boundary condition, the electric current density will be uniformly distributed over the coil terminal. A coil with 20 turns and a peak electric current of $\sqrt{2} \times 425$ A through each turn is thus represented. At the bottom surface of the electrodes, a current source with a peak value of $\sqrt{2} \times 2304.5$ A is defined. The electrode current is assumed to be entering through the bottom surface of the electrode E_1 and exiting from that of the electrode E_2 . The magnetic field of the coil and the eigenfield of the electrodes are added together, forming the total magnetic field. Additionally, a region of ambient air is defined with a padding percentage of 200%. For the magnetic field, “Neumann” boundary condition is assumed on all outer boundaries. Under this condition, the magnetic field is tangential to the boundary and cannot cross it. The Neumann boundary condition corresponds to symmetry conditions and is set by default in MAXWELL. On the interfaces between objects, the natural boundary condition is assumed for the magnetic field, which means that the normal component of the magnetic field is continuous across the interface boundaries.

9.7.2 Results and discussion

Figure 9.21 demonstrates the electric current density induced in the girder G_4 , in which the largest eddy current intensity exists. The figure represents the electric current density in a cross sectional plane through the centre of G_4 . Eddy currents have the largest density of about 8×10^5 A/m² in the region of the upper surface of the girder. However, the greater the distance between a girder and the coil, the less intense the eddy current induced. The ohmic loss density is shown in Figure 9.22 for the same cross sectional plane of G_4 . Again, the largest ohmic loss exists in the region of the upper surface of the girder with a density of about 1.5×10^5 W/m³. In addition to the eddy currents, sinusoidal short-circuit currents flow through the connected girders. The maximum currents flow through G_9 and G_{10} . The peak values of the short-circuit currents flowing through the girders are presented in Table 9.8.

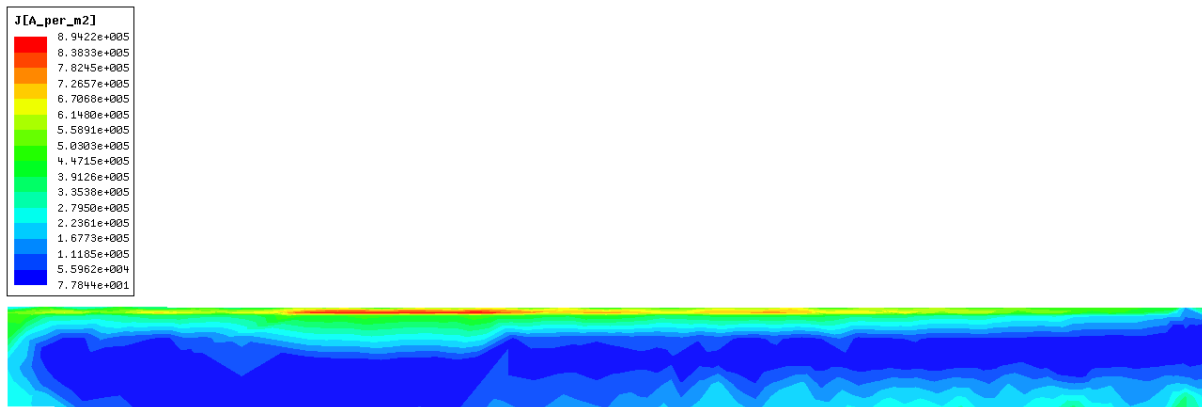


Figure 9.21: Electric current density induced within the steel girder G₄, in a cross sectional plane through the centre of the girder.

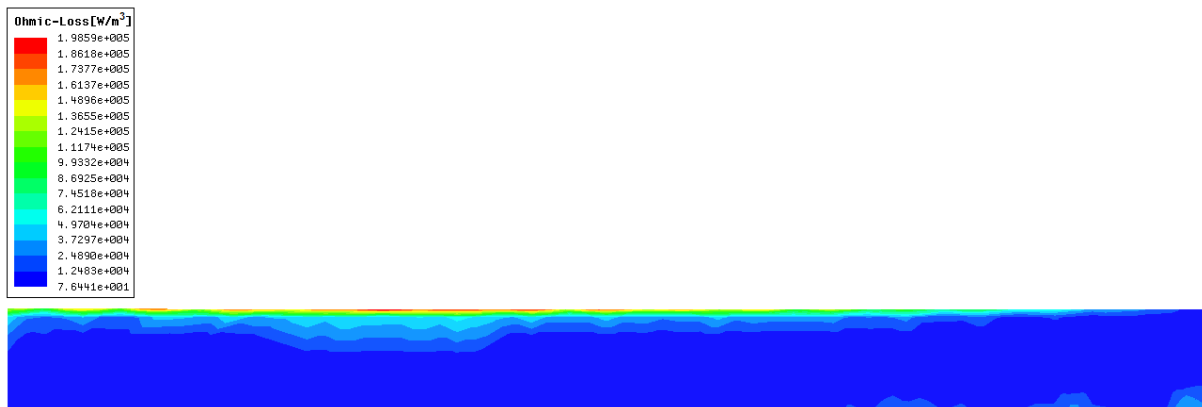


Figure 9.22: Ohmic loss density in W/m³ within the steel girder G₄, in a cross sectional plane through the centre of the girder.

Girder	G ₁	G ₂	G ₃	G ₄	G ₅	G ₆	G ₇	G ₈	G ₉	G ₁₀
I_{peak} in A	10.86	33.11	68.10	80.93	80.74	56.43	22.21	4.44	110.63	110.72

Table 9.8: Peak values of the short-circuit currents flowing through the connected steel girders.

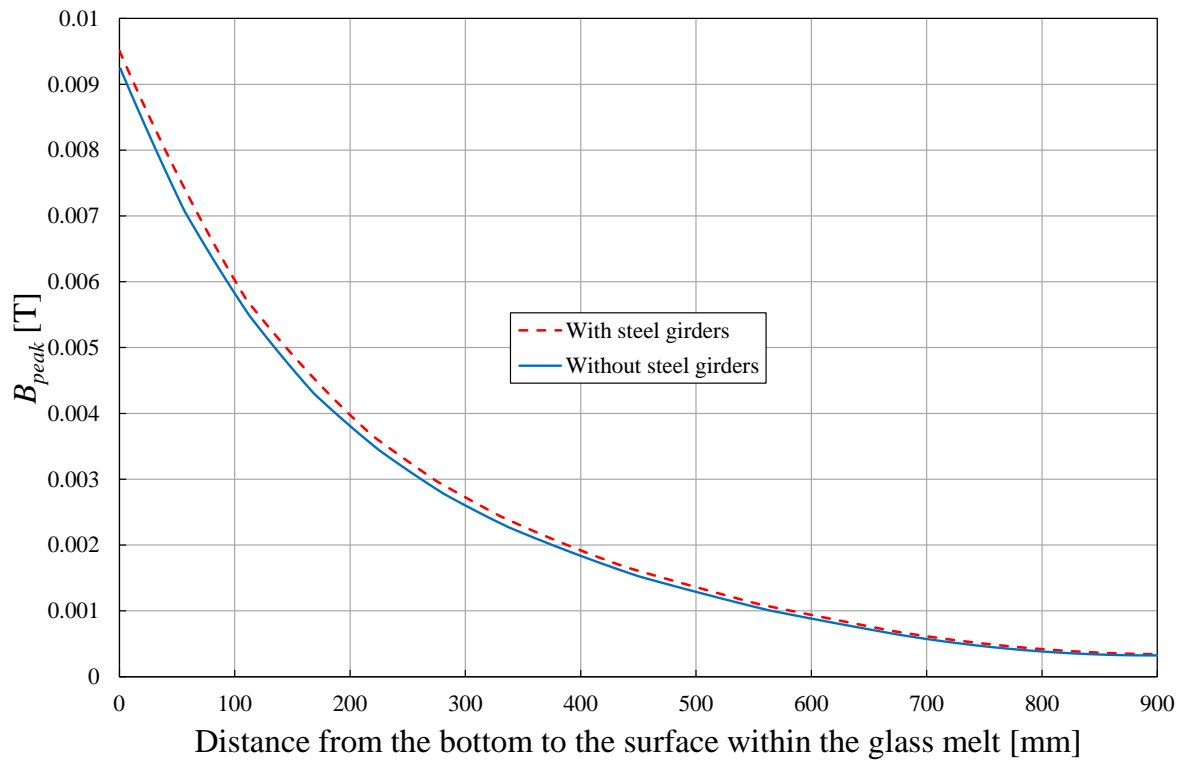


Figure 9.23: Comparison between the magnetic flux density magnitudes (peak value) with and without the steel girders, shown for the vertical center line within the glass melt.

To detect how the steel girders affect the magnetic field within the glass melt, a simulation without the steel girders was performed, to permit comparison of magnetic fields within the glass melt with and without the steel girders. The simulation results reveal that the steel girders contribute to a small increase in the magnetic flux density within the glass melt. The reason is that the high magnetic permeability of the girder material, relative to the surrounding air, causes the magnetic field to follow a shorter path under the coil, effectively concentrating the field. The average increase in the magnetic flux density within the glass melt is about 5.76%. Figure 9.23 presents a comparison of the magnetic flux density magnitudes (peak value) in the vertical center line within the glass melt. No changes in the magnetic field direction within the glass melt are found.

Conclusions drawn from considering the structural steel girders

The existence of steel girders will not be an obstacle to installing magnet coils underneath the tank. Furthermore, the steel girders will support the *EMB* process as they increase the magnetic field intensity within the glass melt. This increase necessitates a corresponding decrease in the coil current $I_C = 425$ A, resulting in lower ohmic losses in the coils. Due to the skin effect, the largest electric current densities are induced in and near the upper surface of the girders. The

ohmic losses in the steel girders are uncritical: the highest ohmic loss is about 121.15 W and the lowest ohmic loss is about 0.20 W (the values are for G₄ and G₈ respectively). Experiments will be necessary to validate the simulation results.

To reduce the electric current densities induced in the steel girders, it would be possible to use a shield of a magnetically conducting material placed directly underneath the coils. This would not only spare the girders from heating effects of eddy currents but also increase the magnetic field intensity within the glass melt and support the *EMB* process.

10 Conclusion and outlook

10.1 Conclusion

This thesis has reported numerical simulations which explore how Lorentz forces generated additionally to the conventional forces in an electrically boosted continuous glass-melting tank can improve the *RTD*. The additional Lorentz forces come in this case from an externally generated magnetic field interacting with the electric currents that are flowing through the glass melt. For this purpose, additional magnet coils are placed underneath the tank bottom and positioned between the boosting electrodes. The additional Lorentz forces are orientated against the main direction of flow within the tank, with the effect of preventing the colder, less well-melted bottom glass from flowing between the electrodes directly to the tank-outlet. This bottom glass thus has a longer residence time within the tank. The new and innovative approach is called electromagnetic boosting, *EMB*. The work represents the *first* investigation of the employment of additionally generated Lorentz forces to improve the performance of an industrial continuous glass-melting tank.

Because of the temperature-dependent physical properties of glass, coupled electrodynamic, thermodynamic, and hydrodynamic effects have to be calculated for the numerical simulation. Coupling of the calculations is achieved by implementing electromagnetic field calculation in the commercial software program FLUENT (developed for calculating coupled hydrodynamic and thermodynamic effects on the basis of FVM). This coupling method has been tested, and the electromagnetic field calculation with FLUENT has been validated by numerical simulation using the commercial software MAXWELL (developed for calculating electromagnetic effects on the basis of FEM). The author has found the method to be reliable and accurate.

The simulations have been performed for an actual industrial-scale continuous glass-melting tank using an academic representation of the tank. The goal was a model permitting investigation of the pure effects of the additionally generated Lorentz forces on the flow pattern within the tank and basic evaluation of the *EMB*. The boundary conditions were so defined as to simulate the realistic conditions in the actual tank. The numerical simulations were thoroughly verified to ensure sufficient numerical accuracy. The simulation results were found to agree qualitatively with the expected characteristics of the industrial continuous glass-melting tank. An external magnet coils system was adapted to realize *EMB* in the tank considered. The simulations showed that it is basically possible to create an electromagnetic wall within the glass melt between the boosting electrodes. Further parameter analyses were carried out to establish the optimum *EMB* effects, which are optimally increased *MRT* and improved *RTD*. With the simulation, it was possible for the first time to predict and analyze the dynamic behavior of

operating *electromagnetically boosted* continuous glass-melting tank. This dynamic operation was analyzed for the case both with and without *EMB*. The comparison revealed that *EMB* is favorably affecting the glass melt flow within the tank, increasing the *MRT* substantially and thus enhancing the glass quality. *RTD* in the tank was also improved, which, in turn, resulted in more homogeneous timed distribution of the energy consumed. Moreover, with *EMB*, the tank simulations showed that it is possible to simultaneously increase the tank productivity and enhance the glass quality. This is not possible in the ordinary tank operation case without *EMB*. The rise in tank productivity leads to higher tank thermal efficiency. As an ultimate result, the tank performance has been substantially enhanced by *EMB*.

10.2 Outlook

In this work, the calculations have been coupled by a numerical method which is an efficient means of addressing Multiphysics problems. The method can be extended to a wide range of coupled problems. It would be possible to include eddy currents and the currents induced by movement of conducting bodies in future simulations.

The new innovative concept of *EMB* to provide a contactless flow control in continuous glass-melting tanks can be further supported by plates of a magnetically conducting material to increase the magnetic field intensity within the glass melt. Such plates would mean that ohmic losses in the coils could be reduced by decreasing the currents in them, but would involve additional costs.

Installing an *EMB* system is viable investment which will improve the operational flexibility of continuous glass-melting tanks. The present work is the foundation necessary to convert the idea into an effective industrial process in the future. The results have already been discussed at specialized conferences of the glass industry and found to be promising. However, no industrial partner is yet ready to embark on a costly and large construction with risky conditions so that the process is performed on an operating tank. The first step, always the most important, has been taken en route to a sophisticated glass-melting tank characterized by high efficiency and high production quality. Using *EMB* to improve the tank efficiency and increase the production quality simultaneously will serve the constant aim of glass manufacturing, which is to produce high quality glass as cheaply as possible. The range of application of the technique could also be extended to different tank types and sizes, enabling a variety of goals to be met, among them a substantial reduction in energy consumed.

Bibliography

- [1] P. McCray (Ed.), The prehistory & history of glassmaking technology: [proceedings of the Prehistory and History of Glassmaking Technology Symposium, held at the 99th Annual Meeting of the American Ceramic Society in Cincinnati, Ohio, May 4 - 7, 1997], American Ceramic Soc, Westerville, Ohio, 1998.
- [2] W.S. Ellis, Glass: From the first mirror to fiber optics, the story of the substance that changed the world, 1st ed., Avon Books, New York, c1998.
- [3] S.C. Rasmussen, How glass changed the world: The history and chemistry of glass from antiquity to the 13th century, Springer, Heidelberg, 2012.
- [4] H.G. Pfaender, Schott guide to glass, 2nd ed., Chapman & Hall, London, 1996.
- [5] S. Spauszus, D. Schnapp, Glas allgemeinverständlich: Eine Einführung in Theorie und Praxis, 1st ed., VEB Fachbuchverlag, Leipzig, 1977.
- [6] I. Fanderlik (Ed.), Silica glass and its application, Elsevier, Amsterdam, 1991.
- [7] H. Rawson, Properties and applications of glass, 1st ed., Elsevier, Amsterdam, 1984.
- [8] C.W. Sinton, Raw materials for glass and ceramics: Sources, processes, and quality control, Wiley, Hoboken, NJ, 2006.
- [9] J. Lange, Rohstoffe der Glasindustrie ; mit 128 Tabellen, 3rd ed., Dt. Verl. für Grundstoffindustrie, Leipzig, 1993.
- [10] T.H. Finger, Glass Batch Plant Control with Small Computers, IEEE Trans. on Ind. Applicat. IA-8 (1972) 168–172.
- [11] J.E. Polcyn, W.C. Susor, Computer Controlled Glass Batching System, IEEE Trans. on Ind. Applicat. IA-8 (1972) 542–548.
- [12] P.J. Doyle, Glass-making today: An introduction to current practice in glass manufacture, Portcullis Press; Available from International Publications Service, Collins, Redhill [England], New York, 1979.
- [13] G. Nölle, Technik der Glasherstellung: 41 Tabellen, 3rd ed., Dt. Verl. für Grundstoffindustrie, Stuttgart, 1997.
- [14] F.V. Tooley, The Handbook of glass manufacture: a book of reference for the plant executive, technologist and engineer, Books for Industry Inc., New York, 1974.
- [15] W. Trier, Glasschmelzöfen: Konstruktion und Betriebsverhalten ; mit 63 Tabellen, Springer, Berlin, 1984.

- [16] O. Verworner, K. Berndt, *Feuerfeste Baustoffe für Glasschmelzanlagen: Feuerfeste Baustoffe ; Glasschmelzanlagen ; Bauelemente der Glasschmelzanlagen, ihre Baustoffe und Beanspruchung ; mit 112 Bildern, 49 Tabellen, 1st ed., Dt. Verl. für Grundstoffindustrie, Leipzig, 1978.*
- [17] G.A. Pecoraro, J.C. Marra, J.T. Wenzel (Eds.), *Corrosion of materials by molten glass*, American Ceramic Society, Westerville, Ohio, 1996.
- [18] O. Levenspiel, *Chemical reaction engineering*, 3rd ed., Wiley, Hoboken, NJ, 1999.
- [19] H. Bach, Baucke, Friedrich G. K., D. Krause, *Electrochemistry of glasses and glass melts, including glass electrodes: With 22 tables*, Springer, Berlin, 2001.
- [20] S.K. Sundaram (Ed.), *Electrochemistry of glass and ceramics: [proceedings of the Electrochemistry of Glass and Ceramics Symposium, held at the 100th annual meeting of the American Ceramic Society in Cincinnati, Ohio, May 3 - 6, 1998]*, American Ceramic Society, Westerville, Ohio, 1999.
- [21] R.H. Doremus, *Glass science*, 2nd ed., Wiley, New York, NY, 1994.
- [22] Nikolaus Sorg GmbH & Co KG, *Glass Melting Technology. GlasE/10.08/V2.2.*
- [23] R. Kessel, R. Sims, *Die elektrische Zusatzbeheizung für Schmelzwannen - Technologie-stand 2005*, in: *Proceedings 79. Glasstechnische Tagung, Würzburg, 2005.*
- [24] R.D. Argent, *Modern trends in electrode utilization*, *IEEE Trans. on Ind. Applicat.* 26 (1990) 175–182.
- [25] J.S. Stroud, *Molybdenum Electrodes in Glass Tanks*, *IEEE Trans. on Ind. Applicat.* IA-13 (1977) 618–625.
- [26] IEEE Institute of Electrical and Electronics Engineers, Inc, *IEEE Recommended Practice for Electrical Heating Applications to Melting Furnaces and Forehearth in the Glass Industry*, IEEE, New York, 1986.
- [27] U. Lüdtke, S. Soubeih, B. Halbedel, U. Krieger, A. Kelm, *Numerische Simulation der Strömung einer Glasschmelze unter dem Einfluss von extern generierten Lorentzkraften*, in: *Tagungsband Workshop Elektroprozessstechnik, Heyda, Germany, 2011.*
- [28] U. Lüdtke, S. Soubeih, B. Halbedel, *Numerische Simulation der Strömung in einer Glaswanne mit Barriere-Boostelektroden unter dem Einfluss von extern generierten Lorentzkraften*, in: *Tagungsband Workshop Elektroprozessstechnik, Heyda, Germany, 2012.*
- [29] U. Luedtke, S. Soubeih, B. Halbedel, *Numerical simulation of induced alterations of flow patterns within glass melts using external Lorentz forces*, *Journal of iron and steel research international* 19 (2012) 471–474.

- [30] U. Luedtke, S. Soubeih, B. Halbedel, Numerical simulation of electromagnetically controlled flow in glass melting tanks, in: Proceedings of the International Conference on Heating by Electromagnetic Sources HES-13, Padua, Italy, 2013, pp. 45–52.
- [31] U. Lüdtkke, S. Soubeih, B. Halbedel, Numerische Simulation von Glaswannen mit Barrierebooster unter dem Einfluss von extern generierten Lorentzkräften - Vergleich verschiedener Spulensysteme, in: Tagungsband Workshop Elektroprozessertechnik, Heyda, Germany, 2013.
- [32] B. Halbedel, J.O. Torres, U. Lüdtkke, S. Soubeih, Nutzung von Lorentzkräften in der Glasschmelztechnik, in: Thüringer Werkstofftag 2013, Ilmenau, Germany, 2013, pp. 25–32.
- [33] S. Soubeih, U. Lüdtkke, B. Halbedel, Numerical simulation and optimization of a glass melting tank with magnet coil system to improve the residence time distribution, in: Tagungsband Workshop Elektroprozessertechnik, Heyda, Germany, 2014.
- [34] U. Lüdtkke, S. Soubeih, B. Halbedel, Using Numerical Simulation to Optimize the External Magnet System Needed to Improve the Residence Time Distribution of Glass Melting Tanks, in: Proceedings of the International Scientific Colloquium Modelling for Electromagnetic Processing, Hannover, Germany, 2014, pp. 177–182.
- [35] S. Soubeih, U. Luedtke, B. Halbedel, Improving Residence Time Distribution in Glass Melting Tanks Using Additionally Generated Lorentz Forces, *J. Chem. Chem. Eng.* 9 (2015) 203–210.
- [36] S. Soubeih, U. Luedtke, B. Halbedel, Numerical simulation of electromagnetically controlled flow in glass melting process, in: Proceedings of the 23rd International Congress on Glass, Prague, Czech Republic, 2013.
- [37] S. Soubeih, U. Luedtke, B. Halbedel, Using numerical simulation to study the effects of how an external magnet system improves the residence time distribution on glass melting tanks, in: Proceedings of the 1st Joint Meeting of DGG – ACerS GOMD, Aachen, Germany, 2014.
- [38] S. Soubeih, U. Luedtke, B. Halbedel, Numerical simulation of a glass melting tank with a magnet system to improve the residence time distribution, in: Proceedings of the 12th ESG Conference, Parma, Italy, 2014.
- [39] S. Soubeih, U. Lüdtkke, B. Halbedel, Using Numerical Simulation to Investigate How Additional Lorentz Forces Improve the Residence Time Distribution in Industrial Glass Melting Tanks, in: Proceedings of the ANSYS Conference & 33. CADFEM Users' Meeting, Bremen, Germany, 2015, pp. 2.7.6.

- [40] R.A. Murnane, D.A. Nolet, Evolution of simulation techniques to model electric glass furnaces, in: Conference Record of the IEEE Industry Applications Society Annual Meeting, San Diego, CA, USA, 1-5 Oct. 1989, pp. 1384–1394.
- [41] H. De Waal, Mathematical modeling of the glass melting process, *Glastech. Ber.* 63K (1990) 1–18.
- [42] S.R. Venkateswaran, J.L. Conrad, G.A. Walzer, Modeling of the glass melting process, in: Conference Record of the 1990 IEEE Industry Applications Society Annual Meeting, Seattle, WA, USA, 7-12 Oct. 1990, pp. 1343–1348.
- [43] M.K. Choudhary, N.T. Huff, Mathematical modeling in the glass industry: An overview of status and needs, *Glastech. Ber. Glass Sci. Technol.* 70 (1997) 363–370.
- [44] H. Loch, D. Krause (Eds.), *Mathematical simulation in glass technology: With 17 tables and 27 videos on CD*, Springer, Berlin, 2002.
- [45] R.L. Curran, Use of Mathematical Modeling in Determining the Effects of Electrode Configuration on Convection Currents in an Electric Glass Melter, *IEEE Trans. on Ind. Gen. Applicat.* IGA-7 (1971) 116–129.
- [46] R.L. Curran, Mathematical Model of an Electric Glass Furnace: Effects of Glass Color and Resistivity, *IEEE Trans. on Ind. Applicat.* IA-9 (1973) 348–357.
- [47] M.J. Austin, D.E. Bourne, A mathematical model of an electric glass furnace, *Glass Technology* 14 (1973) 78–84.
- [48] G. Leyens, Beitrag zur Berechnung zweidimensionaler Konvektionsströmungen in kontinuierlich betriebenen Glasschmelzwannen: Teil 1. Mathematisches Modell. Teil 2. Ergebnisse der Berechnungen, *Glastech. Ber.* 47 (1974) 251-259 & 261-270.
- [49] H. Mase, K. Oda, Mathematical model of glass tank furnace with batch melting process, *Journal of Non-Crystalline Solids* 38 & 39 (1980) 807–812.
- [50] L. Mardorf, G. Woelk, Berechnung des Verhaltens einer elektrisch beheizten Glasschmelzwanne mit einem mathematischen Modell, *Glastech. Ber.* 56 (1983) 73–84.
- [51] G. Leyens, J. Smrček, Einfluß der Badtiefe und des Durchsatzes auf die Strömungen in der Glasschmelzwanne, *Glastech. Ber.* 55 (1982) 81–87.
- [52] G. Leyens, J. Smrček, J. Thyn, Anwendung der Isotopen-Meßtechnik und eines mathematischen Modells zur Bestimmung der Strömungsverteilung in einer Schmelzwanne, *Glastech. Ber.* 53 (1980) 124–129.
- [53] D.A. Nolet, Applications of modeling and process analysis to furnace operations and re-design, in: Proceedings of the 46th Conference on Glass Problems, Urbana, USA, 1985, pp. 329–339.

- [54] T.-S. Chen, R.E. Goodson, Computation of three-dimensional temperature and convective flow profiles for an electric glass furnace, *Glass Technology* 13 (1972).
- [55] A. Moulton, Two and three dimensional mathematical models of glass tank furnaces, *Glass Technology* 23 (1982) 106–112.
- [56] F. Simonis, H. De Waal, R.C.G. Beerkens, Influence of furnace design and operation parameters on the residence time distribution of glass tanks, predicted by 3-D computer simulation, in: *Collected papers, XIV International Congress on Glass, Calcutta, 1986*, pp. 118–127.
- [57] A. Ungan, R. Viskanta, Three-Dimensional Numerical Simulation of Circulation and Heat Transfer in an Electrically Boosted Glass Melting Tank, *IEEE Trans. on Ind. Applicat.* IA-22 (1986) 922–933.
- [58] A. Ungan, R. Viskanta, Three-dimensional numerical modeling of circulation and heat transfer in a glass melting tank: Part 1. Mathematical formulation. Part 2. Sample simulations, *Glastech. Ber.* 60 (1987).
- [59] M.K. Choudhary, A Three-Dimensional Mathematical Model for Flow and Heat Transfer in Electrical Glass Furnaces, *IEEE Trans. on Ind. Applicat.* IA-22 (1986) 912–921.
- [60] M.K. Choudhary, A modeling study of flow and heat transfer in an electric melter, *Journal of Non-Crystalline Solids* 101 (1988) 41–53.
- [61] A.A. Ghandakly, R.L. Curran, Accurate modeling of interelectrode resistance and power dissipation in electric glass melters, *IEEE Trans. on Ind. Applicat.* 24 (1988) 1057–1061.
- [62] R.A. Murnane, W.W. Johnson, N.J. Moreland, The analysis of glass melting processes using three-dimensional finite elements, *International Journal for Numerical Methods in Fluids* 8 (1988) 1491–1511.
- [63] M.G. Carvalho, M. Nogueira, Modelling of glass melting industrial process, *JOURNAL DE PHYSIQUE IV* 3/C7 (1993) 1357–1366.
- [64] R.G.C. Beerkens, T. van der Heijden, E. Muijsenberg, Possibilities of glass tank modeling for the prediction of the quality of melting processes, *Ceram. Eng. Sci. Proc.* 14(3-4) (1993) 139–160.
- [65] R. Beerkens, Heutige Möglichkeiten zur Modellierung von Glasschmelzöfen voraussetzen zur Qualität des Glasschmelzprozesses, *Glastech. Ber. Glass Sci. Technol.* 71 (1998).
- [66] K.O. Lim, T.H. Song, K.S. Lee, Patterns of natural convection driven by the free surface temperature distribution in a glass melting furnace, *Glass Technology* 39 (1998) 27–31.

- [67] L. Pilon, G. Zhao, R. Viskanta, Three-dimensional flow and thermal structures in glass melting furnaces: Part I. effects of the heat flux distribution. Part II. effects of batch blanket and bubbles, *Glass Sci. Technol.* 75 (2002) 55–68 & 115–124.
- [68] T. Hiejima, H. Azuma, M. Sawasaki, Numerical analysis and measurement of glass flow in a small melting furnace, *Glass Sci. Technol.* 76 (2003) 155–165.
- [69] V. Sardeshpande, U.N. Gaitonde, R. Banerjee, Model based energy benchmarking for glass furnace, *Energy Conversion and Management* 48 (2007) 2718–2738.
- [70] S. Gopalakrishnan, A. Thess, G. Weidmann, U. Lange, Chaotic mixing in a Joule-heated glass melt, *Phys. Fluids* 22 (2010) 013101.
- [71] W. Muschick, E. Muysenberg, Round robin for glass tank models: Report of the International Commission on Glass (ICG) Technical Committee 21 "Modeling of Glass Melts", *Glastech. Ber. Glass Sci. Technol.* 71 (1998) 153–156.
- [72] C. Moukarzel, W.S. Kuhn, D. Clodic, Numerical precision of minimum residence time calculations for glass tanks: Recalculation of Round Robin Test 1 of Technical Committee 21 "Modelling of Glass Melts" of the International Commission on Glass (ICG), *Glass Sci. Technol.* 76 (2003).
- [73] R. Beerkens, Analysis of elementary process steps in industrial glass melting tanks - Some ideas on innovations in industrial glass melting, *Ceramics – Silikáty* 52 (2008) 206–217.
- [74] H.P.H. Muysenberg, F. Simonis, Verification of 3D mathematical simulation with measured temperature profiles during furnace operation, *Glastech. Ber. Glass Sci. Technol.* 68C2 (1995) 55–62.
- [75] J. Bauer, U. Roger, P. Simons, Validation of a mathematical glass tank model, *Glastech. Ber. Glass Sci. Technol.* 72 (1999) 171–181.
- [76] E. Muysenberg, M. Nováčková, M. Trochta, P. Viktorin, Advanced melter operation and training tool, *Glass Sci. Technol.* 75 (2002) 209–215.
- [77] O.R. Hofmann, H. Kaliski, Die elektromagnetische Kraftwirkung auf die Glasschmelze in Elektrodennähe, *Silikattechnik* 42 (1991) 19–21.
- [78] O.R. Hofmann, G. Philipp, Importance of the Lorentz force in electrically heated glass melts, *Glastech. Ber.* 65 (1992) 142–149.
- [79] G. Philipp, O.R. Hofmann, Modelling of electrically heated glass melting furnaces needs inclusion of Lorentz force, in: *Fundamentals of glass science and technology 1993: Proceedings of the Second Conference of the European Society of Glass Science and Technology*, Venice, Italy, 1993, pp. 235–240.

- [80] M.K. Choudhary, Mathematical modeling of MHD and buoyancy driven flow in electric furnaces, in: Proceedings II International Seminar on Mathematical Simulation in the Glass Melting, Vsetin, Czech Republic, 1993, pp. 87–98.
- [81] M.K. Choudhary, A modeling study of flow and heat transfer in the vicinity of an electrode, in: Proceedings of the XVII International Congress on Glass, Beijing, China, 1995, pp. 100–107.
- [82] O.R. Hofmann, A. Thess, Elektromagnetische Beeinflussung der Glasbadströmung - ein neues Anwendungsgebiet der Magnetohydrodynamik, *Glas-Ingenieur* 1 (2002) 39–45.
- [83] O.R. Hofmann, Electromagnetic force in electric glass melting, *Glass Sci. Technol.* 76 (2003).
- [84] L.G. Bates, F.E. Haskell US1853843, 1932.
- [85] A.J. Walkden GB1289317, 1972.
- [86] A.E. Mikelson, V.N. Moshnyaga, A.D. Osmanis, V.T. Slavyanskij, V.S. Shashkin SU814904, 1981.
- [87] A.D. Osmanis, A.E. Mikelson, L.Y. Pochs, I. Barbans, O.M. Mezhdrejs, V.V. Troshin, V.I. Butaeva, N.M. Vygorka, A.I. Grigorev, V.M. Zalevskij SU1024423A.
- [88] V.N. Fekolin, F.A. Stupak, The application of the magnetohydrodynamic effect to the agitation of glass, *Glass Ceram* 41 (1984) 531–535.
- [89] C. Kunert, A. Langsdorf, F.T. Lentjes, K.D. Duch, A. Thess, Y. Kolesnikow DE102004015055A1, 2005.
- [90] C. Giessler, U. Lange, A. Thess, Nonlinear laminar pipe flow of fluids with strongly temperature-dependent material properties, *Phys. Fluids* 19 (2007) 043601.
- [91] C. Giessler, R. Schlegel, A. Thess, Numerical investigation of the flow of a glass melt through a long circular pipe, *International Journal of Heat and Fluid Flow* 29 (2008) 1462–1468.
- [92] C. Gießler, Theoretical investigations of electromagnetic control of glass melt flow. Dissertation, Technische Universität Ilmenau, 2008.
- [93] D. Hülsenberg, B. Halbedel, G. Conrad, A. Thess, Y. Kolesnikov, U. Lüdtke, Electromagnetic stirring of glass melts using Lorentz forces - Experimental results, *Glass Sci. Technol.* 77 (2004) 186–193.
- [94] U. Krieger, Einfluss elektromagnetisch generierter Kraftwirkungen auf die Strömung in Glasschmelzen. Dissertation, Technische Universität Ilmenau, 2007.
- [95] U. Krieger, B. Halbedel, D. Hülsenberg, A. Thess, Electromagnetic effects on glass melt flow in crucibles, *Glass Technol.: Eur. J. Glass Sci. Technol. A* 49 (2008) 33–40.

- [96] D. Cepite, A. Jakovičs, B. Halbedel, U. Krieger, Modelling of electromagnetic glass convection with temperature-dependent properties of the melt, *Magnetohydrodynamics* 43 (2007) 195–204.
- [97] C. Giessler, C. Sievert, U. Krieger, B. Halbedel, D. Huelsenberg, U. Luedtke, A. Thess, A model for electromagnetic control of buoyancy driven convection in glass melts, *FDMP* 1 (2005) 247–266.
- [98] C. Giessler, A. Thess, Electromagnetic control of thermal convection of a fluid with strongly temperature-dependent material properties, *J. Fluid Mech.* 618 (2009) 135–154.
- [99] C. Giessler, A. Thess, Numerical simulation of electromagnetically controlled thermal convection of glass melt in a crucible, *International Journal of Heat and Mass Transfer* 52 (2009) 3373–3389.
- [100] B. Halbedel, D. Hülsenberg, U. Krieger, U. Lüdtkke, G. Carl, H.-J. Linz DE102005058729A1, 2007.
- [101] O.R. Hofmann DE102008011008A1, 2009.
- [102] S. Gopalakrishnan, A. Thess, Electromagnetically induced chaotic mixing in a pipe mixer, *Chemical Engineering Science* 65 (2010) 6282–6291.
- [103] J.O. Torres, B. Halbedel, A novel electromagnetic mixer for the glass melt homogenization - evaluation with a numerical and physical model, in: *Tagungsband Workshop Elektroprozessstechnik*, Heyda, Germany, 2012.
- [104] A.P. Kelm, Numerische Simulation der Strömungsbeeinflussung einer Glasschmelze mit Hilfe von Lorentzkräften. Diplomarbeit, Technische Universität Ilmenau, 2010.
- [105] J.O. Torres, B. Halbedel, C. Weber, R. Reche, High-performance forehearth coloring using Lorentz forces, in: *Tagungsband Workshop Elektroprozessstechnik*, Heyda, Germany, 2014.
- [106] HVG and DGG, Standardglas I der DGG (Kalk-Natron-Glas), available at http://www.hvg-dgg.de/fileadmin/dateien/verein/Standardglas_Ia.pdf (2012).
- [107] H. Loch, Overview, in: H. Loch, D. Krause (Eds.), *Mathematical simulation in glass technology: With 17 tables and 27 videos on CD*, Springer, Berlin, 2002, pp. 1–15.
- [108] B. Halbedel, *Messberichte (unpublished document)*. Technische Universität Ilmenau, Fachgebiet Anorganisch-nichtmetallische Werkstoffe, Ilmenau, 2012.
- [109] R.G. Beerkens, Modeling of the melting process in industrial glass furnaces, in: H. Loch, D. Krause (Eds.), *Mathematical simulation in glass technology: With 17 tables and 27 videos on CD*, Springer, Berlin, 2002, pp. 17–73.
- [110] J.D. Jackson, *Classical electrodynamics*, 3rd ed., Wiley, New York, NY, c 1999.

- [111] R.J. Moreau, *Magnetohydrodynamics*, Kluwer, Dordrecht, 1990.
- [112] F.-T. Lentjes, High-frequency melting of glass in crucibles, in: H. Loch, D. Krause (Eds.), *Mathematical simulation in glass technology: With 17 tables and 27 videos on CD*, Springer, Berlin, 2002, pp. 126–155.
- [113] W.M. Rohsenow (Ed.), *Handbook of heat transfer*, 3rd ed., McGraw-Hill, New York, NY, 1998.
- [114] G. Nellis, S. Klein, *Heat transfer*, Cambridge Univ. Press, Cambridge, 2009.
- [115] U. Lüdtke, *Numerische Simulation gekoppelter Felder in der Elektroprozess-technik*. Habilitationsschrift, Technische Universität Ilmenau, 2014.
- [116] ANSYS FLUENT: Help, ANSYS Inc., 2014.
- [117] N. Ida, *Engineering electromagnetics*, Springer, New York, 2000.
- [118] P.J. Roache, *Verification and validation in computational science and engineering*, Hermosa Publishers, Albuquerque, N.M., 1998.
- [119] W.L. Oberkampf, C.J. Roy, *Verification and validation in scientific computing*, Cambridge Univ. Press, Cambridge, 2010.
- [120] R. Schwarze, *CFD-Modellierung: Grundlagen und Anwendungen bei Strömungsprozessen*, Springer Vieweg, Berlin, 2013.
- [121] ANSYS MAXWELL: Help, ANSYS Inc., 2014.
- [122] K.J. Binns, P.J. Lawrenson, C.W. Trowbridge, *The analytical and numerical solution of electric and magnetic fields*, Wiley, Chichester, 1994.
- [123] A. Kost, *Numerische Methoden in der Berechnung elektromagnetischer Felder*, Springer, Berlin, 1994.
- [124] J.F. Thompson, Warsi, Z. U. A, C.W. Mastin, *Numerical grid generation: Foundations and applications*, North-Holland; Elsevier Science Pub. Co. [distributor], New York, 1985.
- [125] ANSYS, Inc., 8. Thür. ANSYS Hochschultag, Ilmenau, 2013.
- [126] J. Blazek, *Computational fluid dynamics: Principles and applications*, 2nd ed., Elsevier, Amsterdam, 2007.
- [127] P.J. Roache, Quantification of uncertainty in computational fluid dynamics, *Annu. Rev. Fluid. Mech.* 29 (1997) 123–160.
- [128] Technische Universität Ilmenau, available at <http://www.tu-ilmenau.de/it-service/struktureinheiten/advanced-computing/hardware/> (2014).

List of abbreviations

AC	alternating current
AZS	alumina-zirconia-silica
baseline-case	the ordinary tank operation case (with <i>EB</i> but no <i>EMB</i>)
$C_{1,\dots,5}$	coil number 1, ..., 5
CFD	computational fluid dynamics
CPU	central processing unit
DC	direct current
$E_{1,\dots,6}$	electrode number 1, ..., 6
<i>EB</i>	electric boosting
<i>EMB</i>	electromagnetic boosting
EMB-case	tank operation case with <i>EMB</i> under the optimum process conditions
FEM	Finite Element Method
FVM	Finite Volume Method
ICG	International Commission on Glass
<i>MRT</i>	minimum residence time
RRT1	first Round Robin Test
<i>RTD</i>	residence time distribution
TC 21	Technical Committee 21
UDF	user-defined function
UDM	user-defined memory
UDS	user-defined scalar

List of symbols

- A**.....magnetic vector potential (vector field) [Wb/m]
- A**.....complex magnetic vector potential (vector field) [Wb/m]
- A_x**.....*x*-component of magnetic vector potential in Cartesian coordinate system [Wb/m]
- A_{xRe}**.....real part of *x*-component of complex magnetic vector potential in Cartesian coordinate system [Wb/m]
- A_{xIm}**.....imaginary part of *x*-component of complex magnetic vector potential in Cartesian coordinate system [Wb/m]
- A_y**.....*y*-component of magnetic vector potential in Cartesian coordinate system [Wb/m]
- A_{yRe}**.....real part of *y*-component of complex magnetic vector potential in Cartesian coordinate system [Wb/m]
- A_{yIm}**.....imaginary part of *y*-component of complex magnetic vector potential in Cartesian coordinate system [Wb/m]
- A_z**.....*z*-component of magnetic vector potential in Cartesian coordinate system [Wb/m]
- A_{zRe}**.....real part of *z*-component of complex magnetic vector potential in Cartesian coordinate system [Wb/m]
- A_{zIm}**.....imaginary part of *z*-component of complex magnetic vector potential in Cartesian coordinate system [Wb/m]
- A_s**.....surface area of the tank walls
- B**.....magnetic flux density (vector field) [T]
- B**.....complex magnetic flux density (vector field) [T]
- B_c**.....magnetic flux density of the coils (vector field) [T]
- B_c**.....complex magnetic flux density of the coils (vector field) [T]
- B_E**.....magnetic flux density of the electrodes “eigenfield” (vector field) [T]
- B_E**.....complex magnetic flux density of the electrodes “eigenfield” (vector field) [T]
- B_{Total}**.....total magnetic flux density (vector field) [T]

- $\mathbf{B}_{\text{Total}}$ complex total magnetic flux density (vector field) [T]
- \mathbf{B}_{\perp} normal component of magnetic flux density (vector field) [T]
- B_{FLUENT} magnetic flux density magnitude calculated with FLUENT [T]
- B_{MAXWELL} magnetic flux density magnitude calculated with MAXWELL [T]
- B_{peak} peak value of alternating magnetic flux density [T]
- CaO..... calcium oxide
- c_p specific heat capacity [J/kg.K]
- \mathbf{D} electric flux density (vector field) [C/m²]
- $\underline{\mathbf{D}}$ complex electric flux density (vector field) [C/m²]
- d_B percentage total divergence between the magnetic flux densities within the glass melt calculated with MAXWELL and FLUENT [%]
- d_f percentage total divergence between the Lorentz force densities within the glass melt calculated with MAXWELL and FLUENT [%]
- d_J percentage total divergence between the electric current densities within the glass melt calculated with MAXWELL and FLUENT [%]
- dl' infinitesimal length [m]
- dt infinitesimal time [s]
- $\partial/\partial t$ partial derivative with respect to time [1/s]
- $\partial/\partial x_i$ partial derivative with respect to space [1/m]
- $\partial/\partial x$ partial derivative with respect to x -coordinate in Cartesian system [1/m]
- $\partial/\partial y$ partial derivative with respect to y -coordinate in Cartesian system [1/m]
- $\partial/\partial z$ partial derivative with respect to z -coordinate in Cartesian system [1/m]
- dV infinitesimal volume [m³]
- \mathbf{E} electric field intensity (vector field) [V/m]
- $\underline{\mathbf{E}}$ complex electric field intensity (vector field) [V/m]
- E_k kinetic energy [J]
- \mathbf{F} mass fraction [1]
- f frequency [Hz]
- \mathbf{f}_L Lorentz force density (vector field) [N/m³]

$\mathbf{f}_L(t)$	time-dependent Lorentz force density (vector field) [N/m ³]
$\mathbf{f}_L(x,y,z)$	Lorentz force density (vector field) spatial distribution in Cartesian system [N/m ³]
\mathbf{f}_{La}	artificial Lorentz force density [N/m ³]
\mathbf{f}_{Ln}	natural Lorentz force density [N/m ³]
f_{FLUENT}	Lorentz force density magnitude calculated with FLUENT [N/m ³]
$f_{MAXWELL}$	Lorentz force density magnitude calculated with MAXWELL [N/m ³]
\mathbf{g}	gravitational acceleration vector [m/s ²]
h	heat transfer coefficient [W/m ² K]
\mathbf{I}_C	coil current (vector field) [A]
$\underline{\mathbf{I}}_C$	complex coil current (vector field) [A]
$\mathbf{I}_{C\text{ Re}}$	real part of complex coil current (vector field) [A]
$\mathbf{I}_{C\text{ Im}}$	imaginary part of complex coil current (vector field) [A]
I_C	magnitude of effective complex coil current [A]
\mathbf{I}_E	electrode current (vector field) [A]
$\underline{\mathbf{I}}_E$	complex electrode current (vector field) [A]
I_{peak}	peak value of alternating electric current [A]
\mathbf{J}	electric current density (vector field) [A/m ²]
$\underline{\mathbf{J}}$	complex electric current density (vector field) [A/m ²]
J_{FLUENT}	electric current density magnitude calculated with FLUENT [A/m ²]
$J_{MAXWELL}$	electric current density magnitude calculated with MAXWELL [A/m ²]
L	characteristic travelled length [m]
\dot{m}	mass flow rate [kg/s]
\dot{m}_0	ordinary mass flow rate [kg/s]
Max. Δx	maximum length of mesh cell edge [m]
Min. Δx	minimum length of mesh cell edge [m]
MRT	minimum residence time [s]
MRT_0	ordinary minimum residence time [s]
N	a total number

Na_2O	sodium oxide
P	electric power [W]
p_v	Joule heat density [W/m ³]
q_{conv}	convective heat transfer rate [W]
q_{cool}	wall losses [W]
q_{cool}'''	volumetric wall losses [W/m ³]
q_{in}	input heat transfer rate [W]
q_{out}	output heat transfer rate [W]
q_{out0}	ordinary output heat transfer rate [W]
q_{rad}	radiative heat transfer rate [W]
\mathbf{q}_w''	heat flux vector [W/m]
\mathbf{r}, \mathbf{r}'	position vectors [m]
Re	Reynolds number
S_{ϕ_k}	source term of an arbitrary scalar ϕ_k
SiO_2	silicon dioxide
T	temperature [K]
$T(x,y,z)$	temperature spatial distribution in Cartesian system [T]
T_{in}	input temperature [t]
T_{out}	output temperature [T]
T_s	surface temperature [T]
T_∞	ambient temperature [T]
t	time [s]
t_i	residence time of the particle i [s]
t_{max}	maximum residence time [s]
\mathbf{u}	velocity (vector field) [m/s]
\bar{u}	mean flow velocity [m/s]
u_i	velocity component with respect to coordinate [m/s]
V	volume [m ³]
\dot{V}	volumetric flow rate [m ³ /s]

δ	skin depth [m]
ε	surface emissivity
\emptyset	diameter [m]
ϕ_k	arbitrary scalar
φ	electric potential [V]
$\underline{\varphi}$	complex electric potential [V]
φ_{Re}	real part of complex electric potential [V]
φ_{Re}	real part of complex electric potential [V]
η	dynamic viscosity [Pa·s]
$\eta(T)$	temperature-dependent dynamic viscosity [Pa·s]
η_{th}	thermal efficiency
η_{th0}	ordinary thermal efficiency
\int_l	integration over the path l
$\int_{V_{\text{Glass}}}$	integration over the glass melt volume
κ	electrical conductivity [S/m]
$\kappa(T)$	temperature-dependent electrical conductivity [S/m]
λ_{eff}	effective thermal conductivity [W/mK]
λ_w	equivalent effective thermal conductivity of the tank walls [W/mK]
μ	magnetic permeability [H/m]
μ_0	magnetic permeability of a vacuum $\mu_0 = 4\pi \times 10^{-7}$ [H/m]
μ_r	relative magnetic permeability $\mu_r = \mu/\mu_0$
$-\nabla p$	pressure force density [N/m ³]
∇	gradient operator
$\nabla \cdot$	divergence operator
$\nabla \times$	curl operator
∇^2	Laplace operator
ω	angular frequency [rad/s]

ρmass density [kg/m³]

$\rho(T)$temperature-dependent mass density [kg/m³]

$\sum_{i=1}^N$ summation from $i = 1$ to $i = N$

σspread of residence time distribution [s]

σ_0ordinary spread of residence time distribution [s]

σ_BStefan-Boltzmann constant [W/m² K⁴]

τmean residence time distribution [s]

Erklärung

Ich versichere, dass ich die vorliegende Arbeit ohne unzulässige Hilfe Dritter und ohne Benutzung anderer als der angegebenen Hilfsmittel angefertigt habe. Die aus anderen Quellen direkt oder indirekt übernommenen Daten und Konzepte sind unter Angabe der Quelle gekennzeichnet.

Bei der Auswahl und Auswertung folgenden Materials haben mir die nachstehend aufgeführten Personen in der jeweils beschriebenen Weise unentgeltlich geholfen:

Die fachliche Betreuung der Arbeit erfolgte durch PD Dr.-Ing. habil. Ulrich Lüdtke und Dr.-Ing. Bernd Halbedel.

Weitere Personen waren an der inhaltlich-materiellen Erstellung der vorliegenden Arbeit nicht beteiligt. Insbesondere habe ich hierfür nicht die entgeltliche Hilfe von Vermittlungs- bzw. Beratungsdiensten (Promotionsberater oder anderer Personen) in Anspruch genommen. Niemand hat von mir unmittelbar oder mittelbar geldwerte Leistungen für Arbeiten erhalten, die im Zusammenhang mit dem Inhalt der vorgelegten Dissertation stehen.

Die Arbeit wurde bisher weder im In- noch im Ausland in gleicher oder ähnlicher Form einer Prüfungsbehörde vorgelegt.

Ich bin darauf hingewiesen worden, dass die Unrichtigkeit der vorstehenden Erklärung als Täuschungsversuch bewertet wird und gemäß § 7 Abs. 10 der Promotionsordnung den Abbruch des Promotionsverfahrens zur Folge hat.

Ilmenau, den 25.02.2016

Senan Soubeih